

AD-A163 106

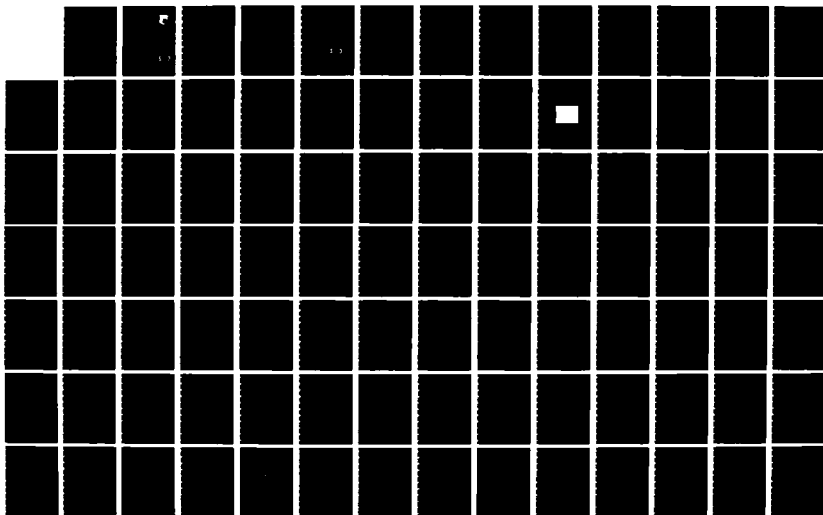
DIODE PUMPED FIBER LASER(U) STANFORD UNIV CA EDWARD L  
GINZTON LAB OF PHYSICS C GAETA ET AL DEC 84 GL-3756  
AFWAL-TR-84-1159 F33615-82-C-1749

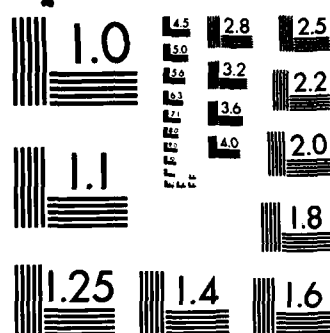
1/8

UNCLASSIFIED

F/G 20/5

NL





MICROCOPY RESOLUTION TEST CHART  
NATIONAL BUREAU OF STANDARDS-1963-A

AD-A163 106

2

AFWAL-TR-84-1159

DIODE PUMPED FIBER LASER



CEL GAETA and MICHEL DIGONNET  
Edward L. Ginzton Laboratory  
Stanford University  
Stanford, California 94305

December 1984

Interim Report for Period September 1983 - July 1984

Approved for public release; distribution unlimited.

DTIC FILE COPY

DTIC  
ELECTE  
JAN 13 1986  
S B D

AVIONICS LABORATORY  
AIR FORCE WRIGHT AERONAUTICAL LABORATORIES  
AIR FORCE SYSTEMS COMMAND  
WRIGHT-PATTERSON AIR FORCE BASE, OHIO 45433

86 1 13 035

# NOTICE

When Government drawings, specifications, or other data are used for any purpose other than in connection with a definitely related Government procurement operation, the United States Government thereby incurs no responsibility nor any obligation whatsoever; and the fact that the government may have formulated, furnished, or in any way supplied the said drawings, specifications, or other data, is not to be regarded by implication or otherwise as in any manner licensing the holder or any other person or corporation, or conveying any rights or permission to manufacture use, or sell any patented invention that may in any way be related thereto.

This report has been reviewed by the Office of Public Affairs (ASD/PA) and is releasable to the National Technical Information Service (NTIS). At NTIS, it will be available to the general public, including foreign nations.

This technical report has been reviewed and is approved for publication.

K L Schepler

DR K.L. SCHEPLER, Project Scientist  
Electro-Optics Sources Group  
Electro-Optics Technology Branch

FOR THE COMMANDER

Ronald F. Paulson

DR RONALD F. PAULSON, Chief  
Electro-Optics Technology Branch  
Electronic Technology Division

"If your address has changed, if you wish to be removed from our mailing list, or if the addressee is no longer employed by your organization please notify AFWAL/AADO, W-PAFB, OH 45433 to help us maintain a current mailing list".

Copies of this report should not be returned unless return is required by security considerations, contractual obligations, or notice on a specific document.

UNCLASSIFIED

SECURITY CLASSIFICATION OF THIS PAGE (When Data Entered)

REPORT DOCUMENTATION PAGE		READ INSTRUCTIONS BEFORE COMPLETING FORM
1. REPORT NUMBER AFWAL-TR-84-1159	2. GOVT ACCESSION NO. ADA 163106	3. RECIPIENT'S CATALOG NUMBER
4. TITLE (and Subtitle) DIODE PUMPED FIBER LASER		5. TYPE OF REPORT & PERIOD COVERED Interim Report 9-1-83 to 7-2-84
		6. PERFORMING ORG. REPORT NUMBER G. L. Report 3756
7. AUTHOR(s) Cel Gaeta and Michel Digonnet		8. CONTRACT OR GRANT NUMBER(s) F33615-82-C-1749
9. PERFORMING ORGANIZATION NAME AND ADDRESS Edward L. Ginzton Laboratory Stanford University Stanford, CA 94305		10. PROGRAM ELEMENT, PROJECT, TASK AREA & WORK UNIT NUMBERS P.E. 62204F 2001 01 99
11. CONTROLLING OFFICE NAME AND ADDRESS Avionics Laboratory (AFWAL/AADO) Air Force Wright Aeronautical Laboratories Wright-Patterson Air Force Base, OH 45433		12. REPORT DATE December 1984
		13. NUMBER OF PAGES 101
14. MONITORING AGENCY NAME & ADDRESS (if different from Controlling Office)		15. SECURITY CLASS. (of this report) Unclassified
		15a. DECLASSIFICATION/DOWNGRADING SCHEDULE
16. DISTRIBUTION STATEMENT (of this Report)  Approved for public release; distribution unlimited.		
17. DISTRIBUTION STATEMENT (of the abstract entered in Block 20, if different from Report)		
18. SUPPLEMENTARY NOTES		
19. KEY WORDS (Continue on reverse side if necessary and identify by block number) Laser source      Optical fiber laser      Single mode fiber system Nd:YAG single crystal      Q-switched optical fiber optical fiber      laser LiNbO <sub>3</sub> single crystal      Optical waveguides optical fiber      Single crystal fiber growth		
20. ABSTRACT (Continue on reverse side if necessary and identify by block number)  This report describes work conducted in the area of single crystal fiber optical devices. Miniature Nd:YAG 1.32 $\mu$ m lasers were fabricated using both free space (unguided) and single crystal fiber configurations. Bulk lasers with thresholds as low as 19 mw and near optimum slope efficiencies of 36% were demonstrated. Several guided fiber lasers were also successfully brought to oscillation. The best device has a threshold of 12 mw, a slope efficiency of 22%, and a maximum recorded output power at 1.32 $\mu$ m of 22 mw.		

DD FORM 1 JAN 73 1473

EDITION OF 1 NOV 65 IS OBSOLETE

S N 0102-LF-014-6601

UNCLASSIFIED

SECURITY CLASSIFICATION OF THIS PAGE (When Data Entered)

UNCLASSIFIED

SECURITY CLASSIFICATION OF THIS PAGE (When Data Entered)

## 20. Abstract (continued)

Fiber scattering properties inferred from these measurements indicate that the crystal fibers used in this work exhibit a much higher quality than the fibers used in earlier phases of this work as a result of improved growth conditions. A theoretical investigation of 1.32  $\mu\text{m}$  optically-pumped lasers was also developed for interpretation of experimental data. *micrometers*

A feasibility study of Q-switched fiber lasers operating near  $\lambda = 1.06 \mu\text{m}$  was also conducted. Theoretical expressions for the laser output peak power, pulse width and energy were cast in a simple form by implementing the formalism of normalized mode overlap coefficient introduced earlier in this work. Peak powers on the order of 100-500 watts and pulse widths of a few nanoseconds are anticipated for fiber lasers with a V-number in the optimum range of 4-16. Potential Q-switched fiber lasers were also reviewed and compared to provide a recommended guideline for future pulsed fiber laser work. An electro-optically Q-switched Nd:LiNbO<sub>3</sub> fiber laser is currently the most appealing candidate, although other passive schemes are considered.



Accession For	
NTIS	<input checked="" type="checkbox"/>
DTIC	<input type="checkbox"/>
Unannounced	<input type="checkbox"/>
Justification	
By	
Distribution/	
Availability Codes	
Dist	Avail and/or Special
A-1	

DTIC  
ELECTE  
JAN 13 1986  
B

S/N 0102-LF-014-6601

UNCLASSIFIED

SECURITY CLASSIFICATION OF THIS PAGE (When Data Entered)

The authors would like to acknowledge Dr. Wolf Schuebel, for his insight into the possibilities afforded by single crystal fiber lasers, his key roll in arranging support for this area, and his essential contributions to its successful development. We dedicate this manuscript to him.

## TABLE OF CONTENTS

### PART A - GENERAL INTRODUCTION

I. BACKGROUND . . . . .	1
II. OBJECTIVES . . . . .	2
III. SUMMARY OF RESULTS . . . . .	2
IV. GENERAL PLAN . . . . .	4

### PART B - 1.32 $\mu\text{m}$ FIBER LASERS

I. Nd:YAG FIBER LASER FABRICATION . . . . .	5
A. FIBER GROWTH . . . . .	5
B. FIBER PROCESSING . . . . .	7
1. Arrays with Capillary Tubes . . . . .	7
2. High Temperature Epoxy . . . . .	11
3. Individual Fiber Lasers . . . . .	11
II. MODAL OVERLAP THEORY IN 1.32 $\mu\text{m}$ LASERS . . . . .	12
A. INTRODUCTION . . . . .	12
B. REVIEW OF GENERAL THEORY OF MODAL OVERLAPS IN LASERS . . . . .	13
C. FREE SPACE LASERS . . . . .	15
1. Introduction . . . . .	15
2. Threshold Pump Power . . . . .	17
3. Slope Efficiency . . . . .	19
4. Summary . . . . .	19
D. FIBER LASERS . . . . .	19



1. Introduction . . . . .	19
2. Threshold Pump Power . . . . .	22
3. Slope Efficiency . . . . .	22
4. Summary . . . . .	27
<b>IV. ARGON LASER PUMPED Nd:YAG LASERS . . . . .</b>	<b>27</b>
<b>A. MINIATURE BULK LASERS . . . . .</b>	<b>27</b>
1. Laser Cavity . . . . .	27
2. Experimental Arrangement . . . . .	29
3. Laser Measurements . . . . .	29
a. Laser Crystals . . . . .	29
b. Laser Characterization . . . . .	31
c. Interpretation . . . . .	33
<b>B. FIBER LASERS . . . . .</b>	<b>33</b>
1. CW Argon Pumping . . . . .	33
a. Experimental Procedure . . . . .	35
b. Laser Measurements . . . . .	36
c. Interpretation . . . . .	38
2. Pulsed Argon Pumping . . . . .	40
a. Experimental Procedure . . . . .	40
b. Laser Measurements . . . . .	41
c. Transverse Mode Profiles . . . . .	47
d. Loss Calculations . . . . .	50
e. Comparison with 1.064 $\mu\text{m}$ Fiber Lasers . . . . .	50
<b>V. DYE LASER PUMPING . . . . .</b>	<b>51</b>
<b>A. COHERENT DYE LASER SYSTEM . . . . .</b>	<b>51</b>
<b>B. EXPERIMENTAL ARRANGEMENT . . . . .</b>	<b>52</b>
<b>C. DISCUSSION . . . . .</b>	<b>53</b>

## PART C - THEORETICAL ANALYSIS AND DESIGN OF Q-SWITCHED FIBER LASERS

I.	MODAL OVERLAP THEORY OF Q-SWITCHED LASERS . . .	53
A.	GENERAL THEORY . . . . .	53
B.	SINGLE MODE CASE . . . . .	56
1.	Output Power . . . . .	56
2.	Maximum Output Power . . . . .	57
3.	Pulse Energy . . . . .	59
4.	Pulse Width . . . . .	59
5.	Initial Population Inversion . . . . .	60
C.	Q-SWITCHED FIBER LASERS . . . . .	61
1.	Fiber Laser Configuration . . . . .	61
2.	Behavior of Population Inversions . . . . .	62
3.	Maximum Output Power . . . . .	62
4.	Output Pulse Energy . . . . .	66
5.	Pulse Width . . . . .	69
6.	Summary . . . . .	69
II.	EVALUATION OF FIBER LASER Q-SWITCHING SCHEMES .	72
A.	SWITCHING METHODS . . . . .	72
1.	Introduction . . . . .	72
2.	Mechanical Q-Switching . . . . .	72
3.	Electro-optic Q-Switching . . . . .	74
4.	Electro-optic Active Material: Nd:LiNbO <sub>3</sub> . . . . .	77
5.	Passive Q-Switching . . . . .	80
B.	COMPARISON OF SWITCHING METHODS . . . . .	82
C.	RECOMMENDATIONS . . . . .	86

III. CONCLUSIONS . . . . .	86
REFERENCES . . . . .	88

## LIST OF ILLUSTRATIONS

1	Schematic Representation of Polishing Jig with Nd:YAG Fibers in Glass Capillary Cubes . . . . .	8
2	Polished End-Face of Nd:YAG Fiber #17-4 mounted in Glass Capillary Tube with Epoxy . . . . .	10
3	Plot of Absorbed Pump Power at Threshold versus the Waist of the Pump Beam . . . . .	18
4	Slope Efficiency versus Round-Trip Loss . . . . .	20
5	Incident Threshold Pump Power versus Core Radius . . . . .	23
6	Incident Threshold Pump Power versus Core Radius ( $\lambda_p = 808$ nm) . . . . .	24
7	Slope Efficiency (with respect to Incident Power) versus Core Radius . . . . .	25
8	Slope Efficiency versus Core Radius ( $\lambda_p = 808$ nm) . . . . .	26
9	Schematic of the Laser Cavity . . . . .	28
10	Diagram of the Experimental Arrangement for Miniature Nd:YAG Laser . . . . .	30
11	Laser Output Power versus Absorbed Pump Power for Crystal#1.	32
12	Laser Output Power versus Absorbed Pump Power for Crystal No. 2 . . . . .	34
13	Output Power versus Pump Power using a 1 Minute Rest Interval between Data Points . . . . .	37
14	Output Power versus Pump Power with no Rest Interval be- tween Data Points . . . . .	39
15	Output Power versus Pump Power for Fiber #17-3 . . . . .	42
16	Output Power versus Pump Power for Fiber #17-4 . . . . .	43

17	Output Power versus Pump Power for Fiber #17-1 . . . . .	45
18	Output Power versus Pump Power for Fiber #18-4 . . . . .	46
19	Horizontal Mode Profile of 1.32 $\mu\text{m}$ Output from Fiber #17-1 . .	48
20	Vertical Mode Profile of 1.32 $\mu\text{m}$ Output from Fiber 17-1 . . . .	49
21	Fraction of the Initial Inversion remaining after the Q-switch Pulse versus the Ratio of the Initial Inversion at the Beginning of the Pulse to the Threshold Inversion . . . . .	58
22	Behavior of Population Inversions as a Function of the Fiber Core Radius . . . . .	63
23	Population Inversion versus Fiber Core Radius . . . . .	64
24	Peak Output Power as a Function of the Fiber Core Radius . . .	65
25	Plot of Peak Output Power versus Fiber Core Radius . . . . .	67
26	A Plot of Pulse Energy versus Core Radius . . . . .	68
27	Pulse Energy as a Function of the Fiber Core Radius . . . . .	70
28	Pulse Width versus Core Radius . . . . .	71
29	Typical Arrangement for an Electro-optic Switch in a Fiber Laser . . . . .	75
30	Required Switching Voltage for LiNbO <sub>3</sub> Fiber as a Function of the Ratio of Length to Diameter . . . . .	78
31	Initial and Threshold Population Inversions as a Function of Pump Power . . . . .	83
32	Dye Loss versus Pump Power . . . . .	84
33	Peak Output Power versus Pump Power . . . . .	85

## LIST OF TABLES

1	Summary of Results for Bulk Lasers . . . . .	33
2	Summary of Results for Fiber #17-4 . . . . .	40
3	Measured Absorption Coefficients and Growth Rates . . . . .	44
4	Summary of Results for Arrays #17 and #18 . . . . .	47
5	Fiber Laser Mode Waist Sizes . . . . .	50
6	Scattering Loss Coefficients . . . . .	51
7	Scattering Loss for 1.064 $\mu\text{m}$ Fiber Lasers . . . . .	52
8	Measured Optical Parameters of Nd:LiNbO <sub>3</sub> (c $\perp$ F) . . . . .	79
9	Properties of Some 1.064 $\mu\text{m}$ Saturable Absorbers . . . . .	81

## PART A - GENERAL INTRODUCTION

### I. BACKGROUND

Development of fiber optic systems is progressing at a rapid rate. These include all fiber gyroscopes,<sup>1</sup> sensors,<sup>2</sup> and signal processing systems.<sup>3,4</sup> Some advantages of an all fiber approach over existing techniques<sup>5</sup> are increased sensitivity, flexibility in that arbitrary geometric configurations are possible, insensitivity to high voltage and electrically noisy environments due to the dielectric construction of optical fibers, and inherent compatibility with fiber optic data transmission. Such systems are also compact and lightweight.

Earlier hybrid versions of such systems combined optical fibers with bulk optic components such as beamsplitters, polarizers, and phase retardation plates ( $\lambda/4$ ,  $\lambda/2$ , ...etc.). A problem with systems of this type is that the light must, at various points, leave the fiber, interact with a bulk optic component, and then couple back into the fiber. This not only leads to added loss but introduces the additional complexity of alignment of bulk optic components with each other and with the optical fiber. In order to overcome these difficulties a variety of fiber optic devices have been developed in parallel with fiber systems. These new components perform the same functions as their bulk optic counterparts while allowing the light to remain within the fiber. Of particular interest are: a polarization controller which makes it possible to achieve an arbitrary polarization state of the light within the fiber, an evanescent field coupler with a variable coupling coefficient, a polarizer, and a wavelength multiplexer.

In recent years attention has also been directed toward active fiber components.<sup>6-9</sup> This emphasis led to the birth of the field of single crystal fiber optics. Single crystal fibers are grown using the laser - heated pedestal growth method described later in this report. Laser, electro-optic, and other optical intensity dependent processes may be implemented in a fiber format using single crystal fibers. Because the optical field is guided a high optical intensity may be maintained over the entire length of the active material resulting in higher efficiencies and lower thresholds than would be obtained using unguided versions of such devices. Another attractive feature of single crystal fiber optic devices is their inherent geometrical compatibility with standard silica fibers.

Also of interest to the field of fiber optics are high pulse rate optical sources operating in the near infrared, especially miniature sources whose geometries are compatible with those of optical fibers. Pulsed fiber lasers are excellent candidates for this purpose. They may also prove to be very useful devices in the field of optical communication. One method

which can be used to obtain short duration (nanosecond) high peak power (10-100 watts) pulses from lasers is the technique of  $Q$ -switching. This widely used technique involves pumping the gain medium in a laser resonator under a high loss (low cavity  $Q$ ) condition, then to quickly switch the cavity  $Q$  to a high value to release the stored energy in the form of a short, intense pulse. This operation can be accomplished very efficiently in fiber lasers, which can have very low loss cavities and are generally very efficient.

The work reported here is a continuation of the development of single crystal fiber devices, begun in 1979-1980 with the demonstration of Nd:YAG fiber pulse amplifiers,<sup>8</sup> and continued in 1982-1983 with the study of cw Nd:YAG fiber oscillators.<sup>9</sup> During the last year (1983-1984) two new types of fiber devices have been studied. The first task involved the experimental demonstration and characterization of cw Nd:YAG fiber lasers operated at  $1.32 \mu\text{m}$ . The second task comprised a theoretical feasibility study and practical design of  $Q$ -switched crystal fiber lasers operating near  $1.06 \mu\text{m}$ .

## II. OBJECTIVES

The objective of this contract was to develop and evaluate breadboard single crystal fiber optic devices. Two specific types of devices were to be studied. One involved the demonstration and development of a fiber oscillator operating at  $\lambda = 1.32 \mu\text{m}$ . The fibers would be pumped with the  $0.5145 \mu\text{m}$  line of an argon ion laser although a dye laser or laser diode at  $808 \text{ nm}$  could also serve as a pump source if oscillation thresholds in the fiber lasers proved to be sufficiently low. New methods of fiber processing would also be explored to produce better quality devices.

The second type of device would be a  $Q$ -switched fiber laser emitting high peak power (100 W) pulses with pulse widths in the nanosecond range. In this phase of the contract, this study would exclusively take the form of a theoretical study of  $Q$ -switching in fiber lasers including the effects of modal interactions between the laser signal and the pump field as well as a feasibility study of various schemes to  $Q$ -switch a fiber laser.

## III. SUMMARY OF RESULTS

Laser oscillation at  $\lambda = 1.32 \mu\text{m}$  was demonstrated in miniature Nd:YAG bulk lasers under cw pumping conditions with an argon ion laser operating at  $\lambda_p = 0.5145 \mu\text{m}$ . In the best case a slope efficiency of approximately 36% was obtained corresponding to a total round-trip loss of about 1.1%. Since the transmission of the output coupler used was 1% the internal round-trip loss was actually on the order of 0.1%. The slope efficiency



mentioned here is close to the maximum theoretical value of 39%, given by the ratio of the signal and pump photon energies.

New fiber arrays were fabricated using a modified version of a technique employed to construct  $1.064\text{ }\mu\text{m}$  fiber lasers under the previous phase of this contract. In this new scheme individual fibers were inserted in glass capillary tubes and stacked for polishing purposes. Improved angular tolerances between the fiber end-faces were achieved with these arrays, typically better than  $14\text{ mrad}$  ( $0.8^\circ$ ).

Individual fiber lasers were also constructed using glass capillary tubes with large outer diameters (about  $5\text{ mm}$ ) and a new epoxy that could be used in vacuum stations for high temperature ( $200^\circ\text{C}$ ) thin film deposition resulting in good quality AR and mirror coatings on the fiber ends. Work in this area led to the development of suitable polishing techniques that produced a very good quality end-face polish on fibers with diameters as small as  $40\text{ }\mu\text{m}$ . This is the smallest diameter fiber successfully processed in this manner. Angular tolerances between the polished end-faces of these fibers are about  $1\text{ mrad}$ , or  $0.06^\circ$ . This is much better than the result obtained with the arrays because of a better control of the orientation of the fiber within the polishing jig. It is believed that this method can be implemented in a straightforward manner to even smaller diameter fibers.

Both *cw* and pulsed pumping with an argon laser were used to demonstrate  $1.32\text{ }\mu\text{m}$  laser oscillation in both  $170\text{ }\mu\text{m}$  and  $80\text{ }\mu\text{m}$  diameter Nd:YAG single crystal fibers. The output obtained using *cw* pumping was unstable, probably due to thermal effects in the fiber laser cavity caused by the high power pump beam. Pulsed, lower duty cycle pumping resulted in a very stable output power from the fiber lasers. This allowed accurate measurements of the output mode profiles from the fibers to be made. The measured values agreed well with the theoretical predictions for a step index fiber. This indicated that the laser signal was most probably guided by the step index profile of the fiber. Estimates were made of the effective pump area in these fibers as well as the gain cross-section at  $1.32\text{ }\mu\text{m}$ . The average value of the gain cross-section for the  $170\text{ }\mu\text{m}$  fibers is  $0.67 \times 10^{-19}\text{ cm}^2$  which is close to the average value measured for miniature bulk lasers ( $0.68 \times 10^{-19}\text{ cm}^2$ ). Gain cross-sections in the  $80\text{ }\mu\text{m}$  diameter fibers are also in good agreement with this value.

The best result obtained for the fiber lasers is a slope efficiency of about 22%. This indicates that the total round-trip loss in this laser (including the 1% output coupler transmittance) is about 1.8%. The absorbed pump power at threshold in this case is about  $12.0\text{ mW}$ . This particular  $170\text{ }\mu\text{m}$  diameter fiber was selected for use in experiments involving a dye laser system to pump the fiber at  $\lambda_p = 808\text{ nm}$ . Unfortunately, laser oscillation was not obtained here, probably because the output power from the dye laser

was not sufficiently above threshold to compensate for a possibly improper initial fiber laser cavity alignment.

A study of the feasibility of *Q*-switched fiber lasers operating at  $\lambda = 1.064 \mu m$  was completed. This involved the development of a general theory of the effects of modal overlap between the pump and signal fields in an optically pumped laser. The normalized overlap coefficient concept used in the *cw* laser theory was implemented to cast results in a simple form. When applied to the case of a fiber laser it showed that a broad range of fiber core radii (for a given index difference between the core and cladding regions of the fiber) exists for optimum operation of the device. Peak power predicted for 60 *mW* of a  $0.5145 \mu m$  pump coupled into a Nd:YAG fiber is about 240 *W* with a pulse energy of 0.5  $\mu J$  and a pulse width around 4 *nsec*. For the case of a pump wavelength of 808 *nm* the peak power would be about 1 *kW* and the pulse energy around 2  $\mu J$ .

#### IV. GENERAL PLAN

Work conducted under this program was essentially divided into two parts. The first parts deals with the experimental and theoretical analysis of Nd:YAG single crystal fiber lasers emitting radiation at  $\lambda = 1.32 \mu m$  in a single (lowest order) transverse mode. The second part of this project involved a feasibility study of *Q*-switched fiber lasers operating at a wavelength of  $1.064 \mu m$ .

This report is organized in much the same way as the project. After a general introduction concerning all aspects of this contract, attention is focussed on the  $1.32 \mu m$  fiber laser work. Growth of Nd:YAG single crystal fibers and device fabrication are described first. A discussion of  $1.32 \mu m$  Nd:YAG miniature bulk lasers is then presented followed by a description of fiber lasers operating at  $\lambda = 1.32 \mu m$  employing both *cw* and pulsed pumping with the  $0.5145 \mu m$  line of an argon ion pump laser. Attempts at pumping with a dye laser at  $\lambda_p = 808 \text{ nm}$  are also discussed.

A theoretical analysis of both free space and fiber lasers operating at  $\lambda = 1.32 \mu m$  is included to assess the performance of the laser devices studied here as well as to study the effects of device and pump beam parameters upon laser characteristics such as slope efficiency and oscillation threshold.

The next part of the report describes the findings of a feasibility study of *Q*-switched laser action in fiber lasers at  $\lambda = 1.064 \mu m$ . A development of a general theoretical model of modal interactions in optically-pumped *Q*-switched lasers is presented first. This theory is then applied to a fiber laser format so that the effects of fiber, pump, and signal parameters upon *Q*-switched laser performance could be ascertained and an optimum

design selected.

An evaluation of various potential methods to *Q*-switch a fiber laser is presented. The relative merits and disadvantages of each method are discussed and recommendations are made concerning suitable switching schemes.

Finally, a general conclusion summarizes the work performed on both 1.32  $\mu\text{m}$  fiber lasers and *Q*-switched 1.064  $\mu\text{m}$  fiber lasers.

## PART B - 1.32 $\mu\text{m}$ FIBER LASERS

### I. Nd:YAG FIBER LASER FABRICATION

#### A. FIBER GROWTH

The single crystal fibers used in this work were grown at Stanford University using the laser - heated pedestal growth technique.<sup>10,11</sup> In the first generation system that produced Nd:YAG single crystal fibers for 1.064  $\mu\text{m}$  fiber laser work a beam from a  $\text{CO}_2$  laser is split into two parts and then recombined at a common focus.<sup>10</sup> A source rod or fiber is then driven upward at speed  $V_s$  into this spot and a molten zone formed at the tip. A platinum wire or oriented seed crystal is then dipped into the molten bead and also pulled upward at a rate  $V_f$  different than that of the parent rod. The diameter  $d_f$  of the new fiber is determined by mass conservation and obeys the relation

$$d_f = \left( \frac{V_s}{V_f} \right)^{\frac{1}{2}} d_s \quad (1)$$

where  $d_s$  is the diameter of the source rod. Diameter variations in the best fibers grown on this station were typically on the order of 5%, for fiber diameters of 80-250  $\mu\text{m}$ . It is believed that part of these variations is due to (1) nonuniformity in the motor speeds, (2) a nonuniform heating of the molten zone due to the manner in which the laser beams are incident upon the source rod, and (3) mechanical vibrations in the motor driven stages. The second generation growth station, developed under other auspices by Prof. R. B. Byer and co-workers,<sup>11</sup> sought to overcome these difficulties with a number of improvements. This system uses a 15 W  $\text{CO}_2$  waveguide laser as the heat source for the growth process because of its high power stability. In addition, an external CdTe electro-optic modulator (EOM) is used to compensate for power fluctuations in the laser. The beam from the laser impinges onto a refraxicon which transforms it into a ring of light with a half Gaussian

cross-section. This ring is then focussed onto the parent rod by gold coated parabolic reflectors. In this way the tip of the source rod is illuminated from all directions by the incident radiation resulting in a uniform heating of the molten zone. Frequency-locked motors and belt drives are used to translate the source rod and fiber upward at their respective velocities to obtain the desired diameter reduction. A visible ( $0.6328\ \mu\text{m}$ ) HeNe laser is aligned coaxially with the invisible  $10.6\ \mu\text{m}$  output from the  $\text{CO}_2$  laser to facilitate the alignment of the optics used in the station. The growth system also features a large controlled atmosphere chamber and motor speed controllers.

Initial growth now typically involves using a  $350\text{-}500\ \mu\text{m}$  diameter parent circular rod. Typical diameter reductions are in the range of 2-4:1 as it was shown that it provides the greatest growth stability.<sup>12</sup> A few iterations of the growth process are thus required to obtain fibers with diameters below  $100\ \mu\text{m}$  of interest for optical device applications. Since fiber growth rates are on the order of millimeters per minute, small diameter fibers ( $< 100\ \mu\text{m}$ ) can be grown several centimeters in length within a few hours. Materials that have been grown in the past  $2\frac{1}{2}$  years include neodymium yttrium aluminum garnet (Nd:YAG), yttrium iron garnet (YIG), sapphire ( $\text{Al}_2\text{O}_3$ ), lithium niobate ( $\text{LiNbO}_3$ ), and gadolinium molybdenum oxide (GMO).

The best diameter variations obtained so far are on the order of 1%. It is expected that these fibers should exhibit lower guided propagation loss than the fibers used in earlier phases of this work. Loss measurements in a  $15\ \text{cm}$  long,  $170\ \mu\text{m}$  diameter ruby fiber, conducted under another program, indicated a propagation loss of about  $0.05\ \text{dB/cm}$ , even though the spectrum of excited guided modes was quite broad. An even lower propagation loss coefficient may be expected for the fundamental fiber mode. This figure demonstrates the possibility of low loss propagation in crystal fibers with good diameter control.

Until a year ago, the smallest fiber diameter obtained was approximately  $50\ \mu\text{m}$  with excellent diameter control (better than 1% in the best cases). Fibers of Nd:YAG were also grown with diameters on the order of  $30\ \mu\text{m}$ , but they showed significant diameter fluctuations. More recently, Nd:YAG and ruby fibers were grown at the Center for Materials Research (CMR) at Stanford University with diameters on the order of  $5\ \mu\text{m}$ . These fibers were grown from  $100\text{-}200\ \mu\text{m}$  diameter fibers in a single step, i.e., under high diameter reduction conditions. Because the fiber grown is then much smaller than the transverse size of the molten zone, this technique is more closely related to a Czochralski growth than to an edge-defined growth. Fiber growth is therefore somewhat less stable, and a more frequent manual control of the growth parameters is required to limit fiber diameter fluctuations. The  $5\ \mu\text{m}$  fibers, in lengths of up to  $10\text{-}15\ \text{mm}$ , currently exhibit 5-20% diameter variations. Lower diameter fluctuations are expected with active feedback,

although the present samples are definitely adequate for initial optical characterization measurements. Such fibers will allow (a) higher optical intensities over the length of the fiber, leading to more efficient devices; (b) a reduction of the maximum number of guided fiber modes. By cladding these fibers with an adequate material using techniques now available, devices may soon be developed which are inherently single transverse mode.

Fibers with diameters of approximately 170, 80, 70, and 40  $\mu\text{m}$  were grown on the second generation fiber growth station for use in the present contract.

## B. FIBER PROCESSING

### 1. Arrays With Capillary Tubes

A total of 6 new fiber arrays were fabricated for the purpose of 1.32  $\mu\text{m}$  laser evaluation, labeled #17 thru #22. The steps involved in their fabrication are detailed in this section.

Fiber array #17 was fabricated using fibers with diameters of approximately 170  $\mu\text{m}$ . The construction of this array employed a slightly modified version of the procedure which had been used under the previous phase of this contract for the development of 1.064  $\mu\text{m}$  fiber lasers. In the past, several Nd:YAG single crystal fibers were placed in a slot which had been cut into the side of a cylinder of Nd:YAG, then fixed into place using epoxy or wax. The cylindrical mounting jig was made of the same material as the fibers so that a flatter polish could be obtained over the entire end-face of a fiber. This approach appeared to work well and yielded fairly good fiber ends. However, because of their small size compared to the width of the slot, the fibers generally aligned themselves in a staggered fashion in the slot, and not all were aligned parallel to the axis of the polishing jig. Such an alignment, however, is crucial for the purpose of polishing the fiber end-faces perpendicular to the fiber axis, and producing low loss lasers.

An additional step in the fabrication process has been implemented for fiber array #17 which provides for better alignment of the fibers within the slot. In this scheme each individual fiber is fastened into a glass capillary tube with epoxy. Several such capillary tubes are then placed into the slot in the mounting jig and held with either epoxy or wax. The procedure is illustrated in Figure 1. The slot is cut in a direction parallel to the outside walls of the mounting jig (which are used as references during polishing) to a good accuracy. By choosing a good fit between the outer diameter of the fiber and the inner diameter of the capillary tube on one hand, and between the outer diameter of the capillary tube and the width of the slot on the other hand (which can be adjusted with

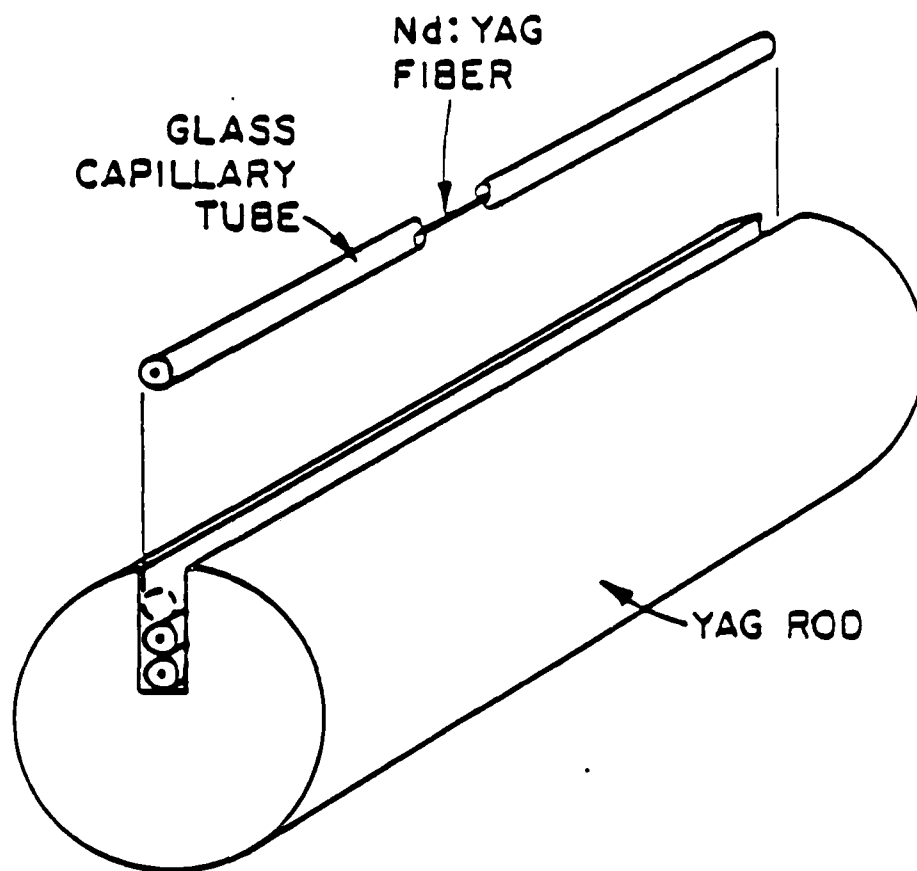


Figure 1 - Schematic Representation of Polishing Jig with Nd:YAG Fibers held in Glass Capillary Tubes.

aluminum foil shims), and carefully layering the capillary tubes inside the slot, all of the fibers are expected to lie nearly parallel to the side walls of the jig after mounting. Using the jig walls as references to polish the fiber ends should then yield fiber ends which are close to being perpendicular to the fiber axis.

This method also facilitates the construction of individual fiber lasers because the fibers may be removed from the mounting jig upon completion of the polishing of their end-faces and still be protected by the glass capillary tubes. These tubes also make it much easier to handle individual fiber samples. In order to remove the fibers from the jig it is necessary to either use wax to hold the glass tubes in place within the slot or an epoxy which is dissolved by chemicals or processes which do not affect the epoxy used to hold the fibers within the capillary tubes themselves. Once the fibers have been removed from the jig they may be used as lasers by coating their end-faces with anti-reflection coatings (for use with external mirrors) or with high reflection dielectric coatings to form a laser with internal mirrors.

Fiber array #17 consists of five 170  $\mu\text{m}$  diameter, 9 mm long fibers held in glass capillary tubes with epoxy as described above. The inner and outer diameters of the capillary tubes are 210  $\mu\text{m}$  and 700  $\mu\text{m}$ , respectively, while the width of the slot is approximately 790  $\mu\text{m}$ . These tolerances indicate that the angle between the reference sides of the jig and each individual fiber does not exceed  $\frac{(90+40)\mu\text{m}}{9\text{mm}} = 14\text{ mrad}$ , or  $0.8^\circ$ .

The mounting jig used for this array has a rectangular cross-section instead of the usual cylindrical geometry. This is not as convenient for the purpose of providing reference surfaces for polishing but was selected since cylindrical jigs were not immediately available. The end-faces were polished to within 4 minutes of each other and then AR-coated for 1.319  $\mu\text{m}$  with about 2390 Å of  $\text{MgF}_2$ .

Upon completion of the polishing and coating steps the end-faces of the array were inspected using an optical microscope. The quality of polish appeared to be quite good for one side of the array with no surface scratches observed but not quite as good for the other side of the array where some chipping remained on the perimeters of some of the fibers. The fibers were fairly well centered within the capillary tubes with the tubes themselves aligned one directly above another within the slot instead of the staggered pattern observed in previous fiber arrays. Under reflected light the Nd:YAG jig and the end-faces of the fibers were observed to have a uniform blue tint due to the AR-coating while the glass capillary tube appeared beige and the epoxy brown. A photograph of an end-face of fiber #17-4 (the fourth fiber from the bottom of the slot in array #17) is presented in Figure 2. We observed a uniform color over the fiber end-faces, which indicates that (1) the AR-coating is adhering well to the surface in a uniform fashion and

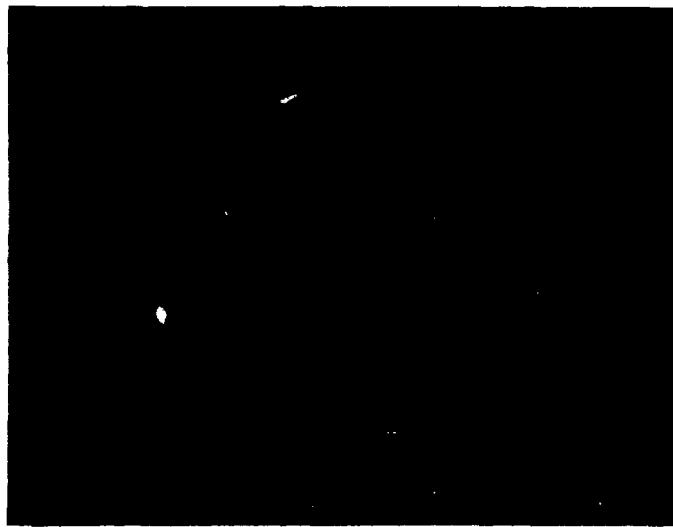


Figure 2 - Polished End-Face of Nd:YAG Fiber #17-4 mounted  
in Glass Capillary Tube with Epoxy.



all the way to the very edge of the fiber, and (2) the optical behavior of the coating is identical for the fiber and the bulk Nd:YAG crystal. This means that it may be possible to deposit multilayer mirror dielectric coatings directly onto the fiber end-faces yielding a self-contained device. In order to obtain the best coating adherence it is usually necessary to heat the substrate during the vacuum deposition. This is not possible with most epoxies because they normally out-gas but may be accomplished using a new epoxy described in Part 2 below.

A second array of Nd:YAG single crystal fibers (array #18) was constructed in the same manner as the previous array with the exception that a cylindrical Nd:YAG jig was used. Four fibers with diameters of approximately  $80\text{ }\mu\text{m}$  were inserted (with epoxy) into glass capillary tubes with inner diameters of about  $140\text{ }\mu\text{m}$ . Some residual chipping was observed around the perimeters of the polished end-faces of the fibers in array #18 although the central portion of a given end-face appeared to be free of pits or scratches. This is where most of the energy of the optical (signal) field is expected to reside for a large index difference between the fiber core and the surrounding epoxy. The length of this array is  $9.5\text{ mm}$ , roughly the same as that of array #17.

## 2. High Temperature Epoxy

Another new feature used in more recent fiber processing work is an epoxy which does not out-gas at elevated temperatures because it does not contain thinners or solvents. Thus it may be used in vacuum stations for high temperature film deposition, a process which yields much better film-to-substrate adhesion than the cold deposition technique employed so far. This makes it possible to deposit good quality AR coatings, and even possibly HR coatings directly onto the fiber end-faces for monolithic fiber laser applications. The epoxy is EPO-TEK H77.<sup>14</sup> It is temperature cured using a schedule of 30 minutes at  $150^{\circ}\text{C}$  or 1 hour at  $120^{\circ}\text{C}$ . Tests conducted at NASA's Goddard Space Flight Center<sup>13</sup> showed that there was less than 1% total mass loss for this epoxy when subjected to a temperature of  $125^{\circ}\text{C}$  in a vacuum chamber at  $10^{-8}$  torr for a period of 24 hours. The manufacturer has also stated that this epoxy was placed in a vacuum chamber at  $500^{\circ}\text{C}$  for 10 hours with no problems.

## 3. Individual Fiber Lasers

Thick walled capillary tubes were used to construct four individual devices (labeled fibers #19 - #22). These low cost glass capillary tubes have outer diameters on the order

of 5-6 *mm* and inner diameters available in increments of 0.001 inch starting from 0.001 inch. Smaller diameter capillary tubes, as well as other non-standard sizes, may also be obtained as custom orders at a higher price. Several tubes were ordered and received with inner diameters of 0.001, 0.002, 0.003, and 0.004 inches. They were obtained in lengths of about 1 foot from which four sections, each approximately 1 *cm* in length, were cut and used in the fabrication of the new devices. These latest devices employed the recently obtained EPO-TEK H77 epoxy for the first time.

Fiber #19 consists of a 70  $\mu\text{m}$  diameter fiber epoxied into a 0.003 inch (76  $\mu\text{m}$ ) diameter capillary tube. Introduction of the epoxy into the space between the inner wall of the capillary tube and the fiber by capillary action appeared to be a difficult proposition because of the viscosity of the epoxy. However, two methods turned out to be successful. Using the first method, epoxy was inserted at both ends of the tube by placing a bead of epoxy on the end and then momentarily heating it with a torch. The sample was then left on a hot plate at the required temperature for curing. This method allowed enough epoxy to enter from the ends to permit grinding and polishing of the end-faces of the fiber to proceed. Polishing the end-faces with 6  $\mu\text{m}$  lap produced chipped end-faces, a difficulty previously encountered in polishing smaller diameter Nd:YAG fibers. After repeated trials with different size laps it was decided to try to use pitch in the final stages of polishing. Good quality end-faces were obtained in this manner.

Fibers #20-22 were constructed using a second method in which a hole was drilled into the side of the capillary tube midway along the length and the epoxy forced through this hole with a syringe until it arrived at the ends of the tube. This proved to be much easier and faster than the first method. The fibers used in these three devices were approximately 40  $\mu\text{m}$  in diameter while the capillary tubes had an inner diameter of about 0.002 in (51  $\mu\text{m}$ ). Angular tolerances (between the polished faces) of about 1 *mrad* can be obtained in this way over a 1 *cm* length. Better tolerances can be obtained by simply using capillary tubes whose inner diameters are better matched to those of the fibers or, alternatively, by growing fibers with diameters that will just fit inside available capillary tubes.

The 40  $\mu\text{m}$  diameter fibers are the smallest Nd:YAG fibers to be successfully processed as described above although the method may be extended to allow even smaller diameter fibers to be processed in the same way. There was no time left on the current contract to place coatings on the end-faces of these new devices but no major problems are expected.

## II. MODAL OVERLAP THEORY IN 1.32 $\mu\text{m}$ LASERS

### A. INTRODUCTION

Once the cavity and pump beam parameters of a fiber laser have been specified, experimental values of the slope efficiency and laser threshold may be used in conjunction with theoretical expressions for these quantities to estimate both the loss in the laser cavity and the gain cross-section. These quantities are useful for rating the overall performance of both unguided and fiber laser devices. In order to do so, a modal overlap theory in fiber lasers was previously developed,<sup>9,15</sup> which is briefly reviewed in this section. We refer the reader to References 9 and 15 for further details on the derivation of the following expressions. Numerical applications study the case of Nd:YAG, for which it is assumed that  $\sigma = 0.67 \times 10^{-19} \text{ cm}^2$  and the fluorescence lifetime  $\tau_f = 236 \text{ } \mu\text{sec}$ . The material refractive index is taken to be 1.813 at  $\lambda = 1.319 \text{ } \mu\text{m}$ , 1.845 at  $\lambda = 0.5145 \text{ } \mu\text{m}$ , and 1.8243 at  $\lambda = 0.808 \text{ } \mu\text{m}$ .

## B. REVIEW OF GENERAL THEORY OF MODAL OVERLAPS IN LASERS

An efficient four level laser system such as Nd:YAG may be modeled as a two level system where the population inversion density  $n(x, y, z)$ , the pumping rate per unit volume  $r(x, y, z)$ , and the photon density of the  $i^{\text{th}}$  transverse mode  $s_i(x, y, z)$  are related by

$$\frac{dn(x, y, z)}{dt} = 0 = r(x, y, z) - \frac{n(x, y, z)}{\tau_f} - \frac{c\sigma n(x, y, z)}{n_l} \sum_{i=1}^m s_i(x, y, z) \quad (2)$$

$$\frac{dS_i}{dt} = 0 = \frac{c\sigma}{n_l} \int \int \int_{\text{cavity}} n(x, y, z) s_i(x, y, z) dv - \frac{c\delta_i}{2ln_l} S_i \quad (3)$$

where a steady state is assumed. Here  $\tau_f$  is the fluorescence lifetime,  $\sigma$  is the gain cross-section,  $c$  is the velocity of light in free space, and  $n_l$  is the index of refraction of the laser material. Total round-trip cavity loss for the  $i^{\text{th}}$  transverse signal mode is represented by  $\delta_i$  and  $l$  is the length of the optical cavity. The total number of photons in the  $i^{\text{th}}$  mode,  $S_i$ , is found by integrating the photon density of the mode over the entire cavity.

Equations (2) and (3) can be combined to eliminate  $n(x, y, z)$  and yield an expression relating the total number of signal photons  $S_i$  in the  $i^{\text{th}}$  mode and the pumping rate  $R$ , obtained by integrating the pumping rate distribution over the volume of the laser medium:

$$J_i(S_1, S_2, \dots, S_m) = \frac{\delta_i}{2l\sigma\tau_f} \frac{1}{R} \quad (4)$$

In Equation (4)  $J_i(S_1, S_2, \dots, S_m)$  is an overlap integral between the  $i^{\text{th}}$  cavity mode and the pump distribution which also includes the effects of saturation due to the presence of all signal modes which may be oscillating. It is given by

$$J_i(S_1, S_2, \dots, S_m) = \int \int \int_{\text{cavity}} \frac{s_{0,i}(x, y, z) r_0(x, y, z)}{1 + \frac{c\sigma\tau_f}{n_i} \sum_{i=1}^m S_i s_{0,i}(x, y, z)} dv \quad (5)$$

where  $s_{0,i}(x, y, z)$  and  $r_0(x, y, z)$  are the normalized distribution functions for the  $i^{\text{th}}$  signal mode and the pump, respectively, defined by

$$s_i(x, y, z) = S_i s_{0,i}(x, y, z) \quad (6)$$

$$r(x, y, z) = R r_0(x, y, z) \quad (7)$$

$$\int \int \int_{\text{cavity}} r_0(x, y, z) dv = \int \int \int_{\text{cavity}} s_{0,i}(x, y, z) dv = 1 \quad (8)$$

Equation (5) actually represents a system of  $m$  equations (for  $m$  cavity modes) which must be solved simultaneously for a given pumping rate to obtain the pump threshold power and conversion efficiency of each signal mode. For the case of a single mode it can be shown that the absorbed pump power at threshold is given by

$$P_{th} = \frac{h\nu_p \delta_i}{\sigma\tau_f} \frac{1}{2l J_1(0)} \quad (9)$$

where

$$J_1(0) = J_1(0, 0, \dots, 0) = \int \int \int_{\text{cavity}} s_{0,1}(x, y, z) r_0(x, y, z) dv \quad (10)$$

Here  $h$  is Planck's constant and  $\nu_p$  is the optical frequency of the pump so that  $h\nu_p$  represents the pump photon energy. Equation (9) can also be written in terms of an effective pump area  $A_p^*$  as

$$P_{th} = \frac{h\nu_p \delta_i}{\sigma\tau_f} \frac{1}{2} A_p^* \quad (11)$$

where

$$A_p^* = \frac{1}{l J_1(0)} \quad (12)$$

It is convenient to introduce the filling factor  $F_{\nu_s, \mu_s, \nu_p, \mu_p}$  here. It is defined as

$$A_p^* = \frac{A_f}{F_{\nu_s, \mu_s, \nu_p, \mu_p}} \quad (\text{fiber case}) \quad (13)$$

$$A_p^* = \frac{\bar{A}_p}{F_{\nu_s, \mu_s, \nu_p, \mu_p}} \quad (\text{unguided case}) \quad (14)$$

where  $(\nu_s, \mu_s)$  and  $(\nu_p, \mu_p)$  characterize the signal and pump modes, respectively. Here  $\bar{A}_p$  is the average pump mode area in the unguided case and  $A_f$  is the area of the fiber in the fiber case. These filling factors entirely characterize the degree of overlap of two given modes within a laser cavity. As it is primarily a function of the fiber V-number only, it can be conveniently tabulated. For example, for a single-mode fundamental pump and signal fiber laser with a V-number larger than about 15,  $F_{0101} \simeq 2 - 2.1$ . The threshold is approximately half of what it would be in a plane wave situation.

When the overlap between the pump and signal modes is good and the laser is operating far above threshold the slope efficiency of the laser is independent of the modal overlap. It is given by<sup>9,15</sup>

$$\eta_{inc} = \frac{P_{out}}{(P_{abs} - P_{th})} = \eta_a \eta_p \frac{T_1}{\delta_1} \frac{h\nu_s}{h\nu_p} \quad (15)$$

where  $T_1$  is the transmission of the output coupler,  $\eta_p$  is the fraction of the pump energy contained within the active region of the laser medium, which is equal to unity for a free space laser, and  $\eta_a$  is given by<sup>9,15</sup>

$$\eta_a = 1 - \exp(-\alpha'_p l) \quad (16)$$

where  $\alpha'_p$  is the effective pump absorption coefficient obtained by multiplying the plane wave absorption coefficient by the fraction of the pump power contained within the active region of the waveguide. For the case of a free space laser it is convenient to reference the slope efficiency to the absorbed pump power so that Equation (15) applies with  $\eta_a = 1$ . The slope efficiency in a fiber laser is referenced to the incident pump power because fiber parameters such as the V - number also affect the amount of pump power that is absorbed by the device. This effect should be taken into account for a proper fiber laser design.

## C. FREE SPACE LASERS

### 1. Introduction

The case of an unguided laser is considered here. Both the pump and the laser signal are assumed to propagate as lowest order (fundamental) circular Gaussian beams with

spot sizes given by  $w_p(z)$  and  $w_s(z)$ , respectively. The radius of a Gaussian beam varies on either side of its waist as

$$w^2(z) = w_0^2 \left\{ 1 + \left[ \frac{\lambda_0(z - z_0)}{\pi w_0^2 n_0} \right]^2 \right\} \quad (17)$$

where  $w_0$  is the waist,  $z_0$  is the waist location,  $\lambda_0$  is the wavelength in vacuum, and  $n_0$  is the index of refraction of the laser crystal at  $\lambda_0$ . The pump and signal beams are assumed to be coaxial and propagating along the  $z$ -axis of the resonator (longitudinal direction). The average of the square of the radius of such a Gaussian beam in a laser crystal of length  $l$  is given by

$$\bar{w}^2 = \frac{1}{l} \int_0^l w^2(z) dz \quad (18)$$

The effective pump area (Equations (10) and (12)) can be approximated by replacing  $w^2(z)$  by its average value  $\bar{w}^2$  for both the pump and signal modes, respectively. The result obtained for lowest order pump and signal modes is then<sup>9,15</sup>

$$A_p^* = \frac{\pi}{2} (\bar{w}_p^2 + \bar{w}_s^2) \quad (19)$$

where  $\bar{w}_p^2$  and  $\bar{w}_s^2$  are the average radii squared for the pump and signal beam, respectively. The pump waist is assumed to be located at  $z_0 = l/2$ . The effective pump area  $A_p^*$  is lowest when  $\bar{w}_p^2$  and  $\bar{w}_s^2$  are minimum. The choice of cavity parameters imposes  $\bar{w}_s^2$  while  $\bar{w}_p^2$  depends upon the way the pump beam is focussed.

For a symmetric laser resonator ( $R_1 = R_2 = R$ ) the waist radius of the signal beam is found from<sup>16,17</sup>

$$w_0^4 = \left( \frac{\lambda_0}{2\pi} \right)^2 d'(2R - d') \quad (20)$$

where  $\lambda_0$  is the lasing wavelength in free space,  $R$  is the radius of curvature of the laser mirrors, and  $d'$  is the effective cavity length given by

$$d' = d - \left( 1 - \frac{1}{n_0} \right) l \quad (21)$$

Here  $d$  is the mirror separation and  $l$  is the length of the laser crystal. A laser resonator formed by placing an 8 mm long crystal of Nd:YAG between mirrors that are separated by 9 mm (with  $n_{YAG} = 1.813$  at  $\lambda = 1.319 \mu m$ ) has an effective length of 5.4 mm which yields a waist radius  $w_0 = 82.5 \mu m$  located at the center of the resonator for a symmetric cavity employing 10 cm radius of curvature mirrors.

The mean square pump beam waist radius  $\bar{w}_p^2$ , computed from Equations (17) and (18), is

$$\bar{w}_p^2 = u_{0,p}^2 \left[ 1 + \frac{1}{12} \left( \frac{\lambda_p l}{\pi n_0 w_{0,p}^2} \right)^2 \right] \quad (22)$$

and can be shown to be minimized when the waist radius takes the optimum value of

$$w_{0,p,opt} = \left( \frac{\lambda_p l}{\sqrt{12} \pi n_0} \right)^{1/2} \quad (23)$$

In the following computer simulations,  $A_p^*$  was calculated from its exact expression (Equations 10 and 12) rather than its approximate form (Equation 19). The spatial distributions for the pump and the signal that were used for these computations are given by:

$$s_{00}(x, y, z) = \frac{2}{\pi d} \frac{1}{w_s^2(z)} \exp \left[ \frac{-2(x^2 + y^2)}{w_s^2(z)} \right] \quad (24)$$

$$r_{00}(x, y, z) = \frac{2}{\pi} \frac{\alpha_p}{1 - \exp(-\alpha_p l)} \frac{1}{w_p^2(z)} \exp \left[ -\alpha_p \left( z + \frac{l}{2} \right) \right] \exp \left[ \frac{-2(x^2 + y^2)}{w_p^2(z)} \right] \quad (25)$$

where  $\alpha_p$  is the absorption coefficient for the laser material at the pump wavelength,  $l$  is the length of the laser material, and  $d$  is the distance between the laser cavity mirrors.

## 2. Threshold Pump Power

A plot of threshold pump power versus the waist of the pump beam (assumed to be located at the center of the resonator) is presented in Figure 3. This curve assumes a total round-trip loss of 1.5%. The laser cavity is taken to be symmetric with 10 cm radius of curvature mirrors. The length of the Nd:YAG crystal is 8 mm, placed between mirrors that are separated by 9 mm. Numerical integration was used to obtain  $A_p^*$ . A similar curve (Figure 3) is obtained for  $\lambda_p = 808$  nm where the absorption coefficient of Nd:YAG is about 4 cm<sup>-1</sup>.

It is evident that a very broad minimum exists for the threshold pump power. This minimum is fairly low - in the range of 10-20 mW and flat for values of the pump waist in the range of 5-40  $\mu$ m. This broad minimum arises from the fact that  $w_{0,p} \ll w_{0,s}$  over the range plotted in Figure 3, so that  $A_p^* \simeq \frac{\pi}{2} \bar{w}_p^2$  is nearly constant over a wide range (see Equation 19). Note that in this configuration, the signal waist radius  $w_s$  is

# THRESHOLD POWER ABSORBED vs PUMP WAIST

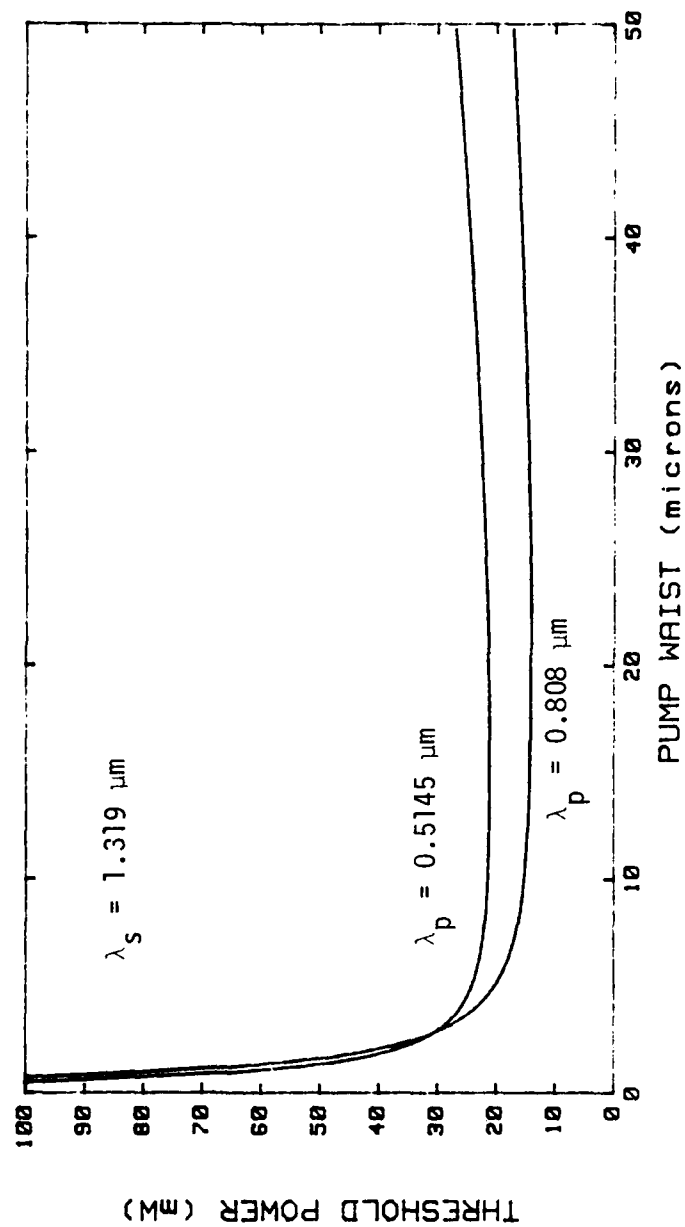


Figure 3 - Plot of Absorbed Pump Power at Threshold versus the Waist of the Pump Beam.



not optimum ( $w_{0,s} = 82.5 \mu m$  while  $w_{0,s,opt} = 43.5 \mu m$ , as given by Equation 23); the threshold would be about four times lower than indicated in Figure 3 with a proper choice of mirror curvature.

### 3. Slope Efficiency

Plots of the slope efficiency referred to absorbed pump power (Equation (15)) are presented in Figure 4 for pump wavelengths of  $0.5145 \mu m$  and  $808 nm$  as a function of the total round-trip loss. When the total round-trip loss  $\delta$  is equal to the transmission of the output coupler (here, 1%) the highest possible slope efficiency is obtained, given by the ratio of signal and pump photon energies. This maximum is 39% for  $\lambda_p = 0.5145 \mu m$  and 61% for  $\lambda_p = 808 nm$ .

### 4. Summary

The theory of modal overlaps in lasers has been applied to the case of a free space laser operating at  $\lambda = 1.32 \mu m$ . Theoretical predictions indicate that a pump waist radius in the range of  $5-50 \mu m$  should yield a minimum threshold power level. Values closer to  $5 \mu m$  will yield better results in principle but in practice there should not be any noticeable difference until the pump waist radius is increased past about  $50 \mu m$ . This work will allow the proper selection of a lens for mode matching the pump beam to the laser signal field in the miniature laser cavity for the experimental portion of this contract.

The slope efficiency that one can expect to obtain from these devices depends upon the internal loss of the laser. Device performance can be assessed, however, by relating measured values of the slope efficiency to the analytical expressions presented here to determine the loss in the cavity.

## D. FIBER LASERS

### 1. Introduction

Assuming a step index fiber configuration with an active core and a passive cladding the laser modes in the core region are given by<sup>18</sup>

$$s_{\nu,\mu_s}(r, \phi) = C_0 J_{\nu_s}(\kappa_{\nu,\mu_s} r) \cos^2 \nu_s \phi \quad (26)$$

# SLOPE EFFICIENCY VS CAVITY LOSS

INTERNAL ROUND-TRIP LOSS

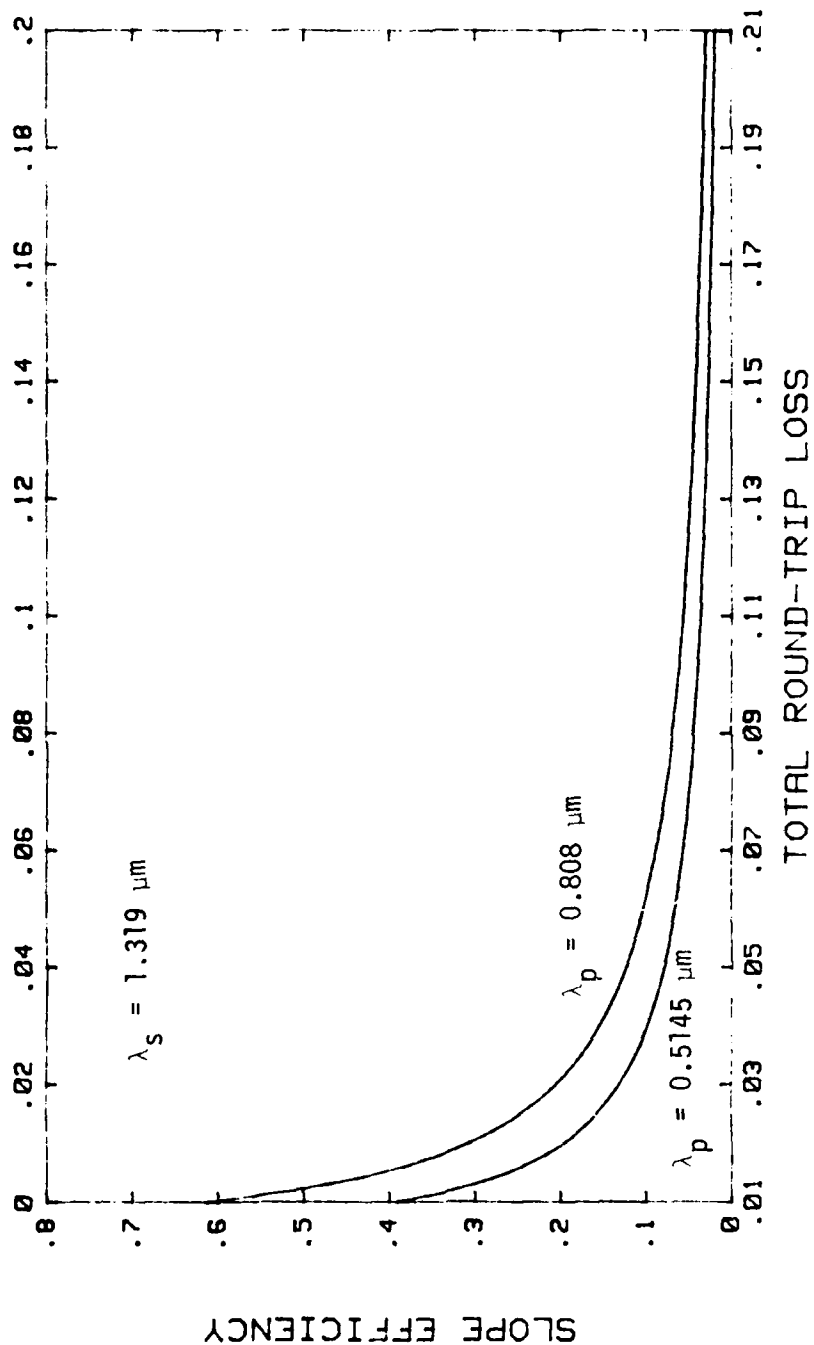


Figure 4 - Slope Efficiency versus Round-Trip Loss.

with the normalization constant  $C_0$  equal to

$$C_0 \equiv \left\{ -e_{\nu_s} \left( \frac{\pi a^2 l}{2} \right) J_{\nu_s+1}(\kappa_{\nu_s, \mu_s} a) J_{\nu_s-1}(\kappa_{\nu_s, \mu_s} a) \left( 1 + \frac{\kappa_{\nu_s, \mu_s}^2}{\gamma_{\nu_s, \mu_s}^2} \right) \right\}^{-1} \quad (27)$$

where  $e_{\nu_s} = 2$  for  $\nu_s = 0$  and 1 otherwise. In Equations (26) and (27)  $a$  is the fiber core radius and  $\beta_{\nu_s, \mu_s}$  is the propagation constant for the  $z$ -direction which is related to  $\kappa_{\nu_s, \mu_s}$  and  $\gamma_{\nu_s, \mu_s}$  by

$$\kappa_{\nu_s, \mu_s} = (n_{core}^2 k^2 - \beta_{\nu_s, \mu_s}^2)^{\frac{1}{2}} \quad (28)$$

$$\gamma_{\nu_s, \mu_s} = (\beta_{\nu_s, \mu_s}^2 - n_{clad}^2 k^2)^{\frac{1}{2}} \quad (29)$$

The modes described above are designated  $LP_{\nu_s, \mu_s}$  (linearly polarized) modes and are valid for a small index difference between the core and the cladding regions, in which case they are approximately linearly polarized in the transverse plane (small  $z$ -component). The propagation constant  $\beta_{\nu_s, \mu_s}$  is found from the eigenvalue equation

$$\kappa_{\nu_s, \mu_s} \left[ \frac{J_{\nu_s+1}(\kappa_{\nu_s, \mu_s} a)}{J_{\nu_s}(\kappa_{\nu_s, \mu_s} a)} \right] = i \gamma_{\nu_s, \mu_s} \left[ \frac{H_{\nu_s+1}^{(1)}(i \gamma_{\nu_s, \mu_s} a)}{H_{\nu_s}^{(1)}(i \gamma_{\nu_s, \mu_s} a)} \right] \quad (30)$$

The pump field is represented likewise. A slight variation in the expression for the pump field results from absorption at the pump wavelength. Since the total pump absorption is large, in a longitudinal optical pumping configuration this effect cannot be ignored. Thus the pump field is represented by

$$r_{\nu_p, \mu_p}(r, \phi, z) = C_{0,p} \exp -(\alpha_a + \alpha_s)z J_{\nu_p}(\kappa_{\nu_p, \mu_p} r) \begin{Bmatrix} \cos^2 \nu_p \phi \\ \sin^2 \nu_p \phi \end{Bmatrix} \quad (31)$$

where

$$C_{0,p} \equiv \left\{ -e_{\nu_p} \left( \frac{\pi a^2}{2(\alpha_a + \alpha_s)} \right) [1 - \exp -(\alpha_a + \alpha_s)l] J_{\nu_p+1}(\kappa_{\nu_p, \mu_p} a) J_{\nu_p-1}(\kappa_{\nu_p, \mu_p} a) \left( 1 + \frac{\kappa_{\nu_p, \mu_p}^2}{\gamma_{\nu_p, \mu_p}^2} \right) \right\}^{-1} \quad (32)$$

and  $e_{\nu_p} = 2$  for  $\nu_p = 0$  and 1 otherwise. Expressions analogous to Equations (28) - (30) are used to determine  $\kappa_{\nu_p, \mu_p}$  and  $\gamma_{\nu_p, \mu_p}$  for the pump mode.

Some predictions are now made concerning the expected behavior of fiber lasers operating at  $\lambda = 1.32 \mu m$  versus fiber diameter and core/cladding index difference.

Calculations were performed assuming an 8 mm length of fiber,  $\delta = 5\%$ , and an output coupler transmission of 1%.  $LP_{01}$  mode profiles are assumed for both the pump and signal modes. An optimum design will then be chosen for future device fabrication.

## 2. Threshold Pump Power

The dependence of the incident pump power at threshold versus fiber core radius is shown in Figure 5 for a pump wavelength of  $0.5145 \mu m$  and Figure 6 for  $\lambda_p = 808 nm$ . The general trend of the curves shows that the incident threshold pump power is infinite at a core radius of zero and decreases to some minimum value as the core radius is increased. This is because in very small fibers almost all of the pump power is present in the passive cladding region. As the core radius is increased most of the pump power is contained in the core region, which is active, the effective pump area is still relatively small, and the threshold is reduced. For larger core radii the threshold depends upon the area of the core and thus increases quadratically with the core radius. The minimum threshold for argon laser pumping is about 0.5 mW occurring at a core radius of about  $2.5 \mu m$  for an index difference of 0.010 ( $V = 2.26$ ). Decreasing the index difference to 0.005 doubles the minimum threshold pump power and shifts it slightly to a core radius of about  $3.5 \mu m$  corresponding to about the same  $V$  number ( $V = 2.24$ ). Even lower thresholds are obtained with a pump wavelength of 808 nm. A minimum threshold of about 0.15 mW (core radius =  $3 \mu m$ ) is predicted for an index difference of 0.010 ( $V = 2.72$ ) compared to 0.3 mW (core radius =  $4.5 \mu m$ ) for an index difference of 0.005, or a  $V$  of about 2.88.

## 3. Slope Efficiency

Slope efficiency versus core radius is shown in Figures 7 and 8 for the two pump wavelengths of interest. The slope efficiency starts at 0 for a core radius equal to 0 and then quickly approaches a constant value as the core radius is increased. This is because the slope efficiency depends upon the fiber parameters through the fraction of pump power contained in the active (core) region. At small values of the core radius most of the pump and signal power extend into the passive cladding of the waveguide, resulting in a poorer interaction. As the core radius is increased the amount of pump power contained in the core approaches unity. The slope efficiency then depends upon the ratio of the signal to pump photon energies and the ratio of the output coupler transmission to the total round-trip cavity loss. These asymptotic values of the slope efficiencies are about 3% for  $\lambda_p = 0.5145 \mu m$  and 12% for 808 nm for the example presented here. For argon laser

# THRESHOLD POWER vs CORE RADIUS

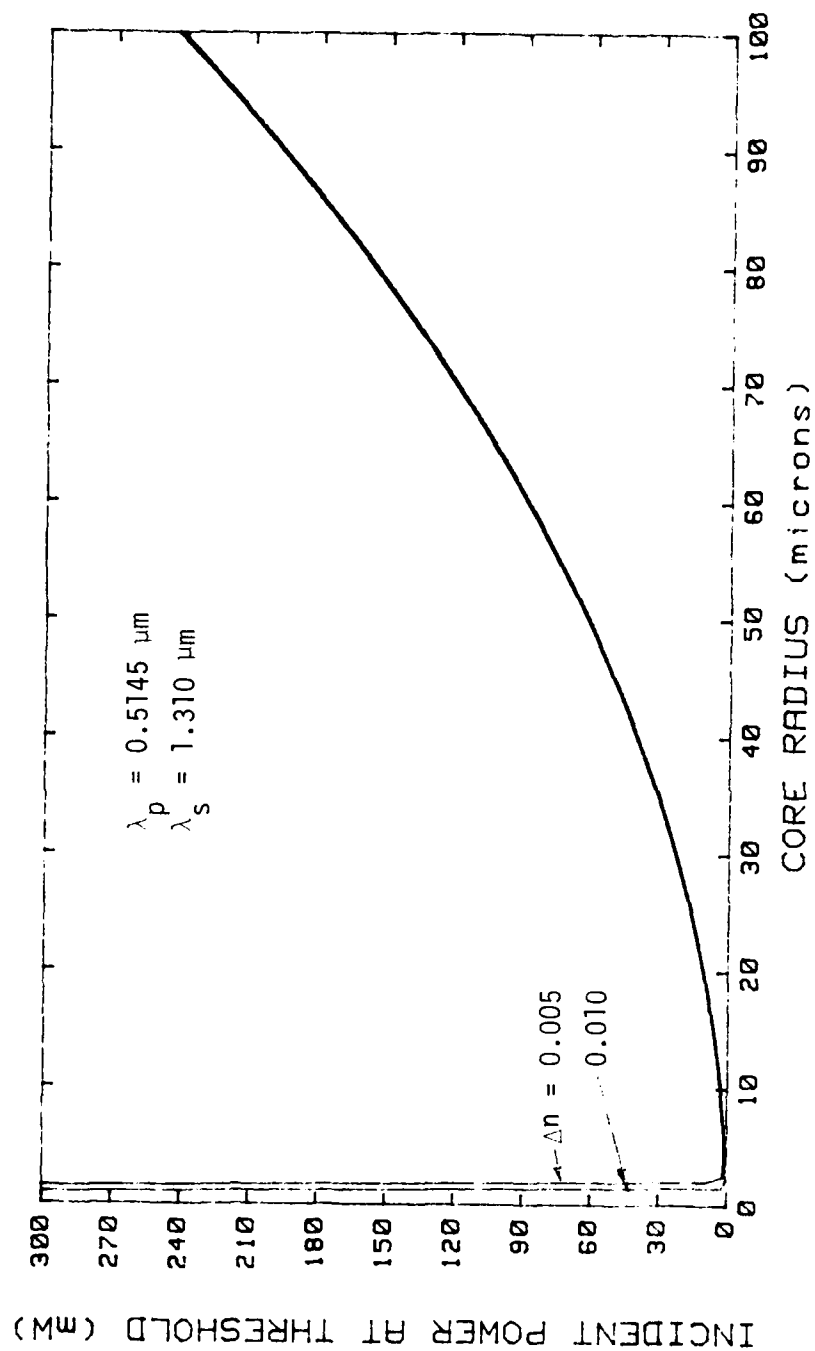


Figure 5 - Incident Threshold Pump Power versus Core Radius.

# THRESHOLD POWER vs CORE RADIUS

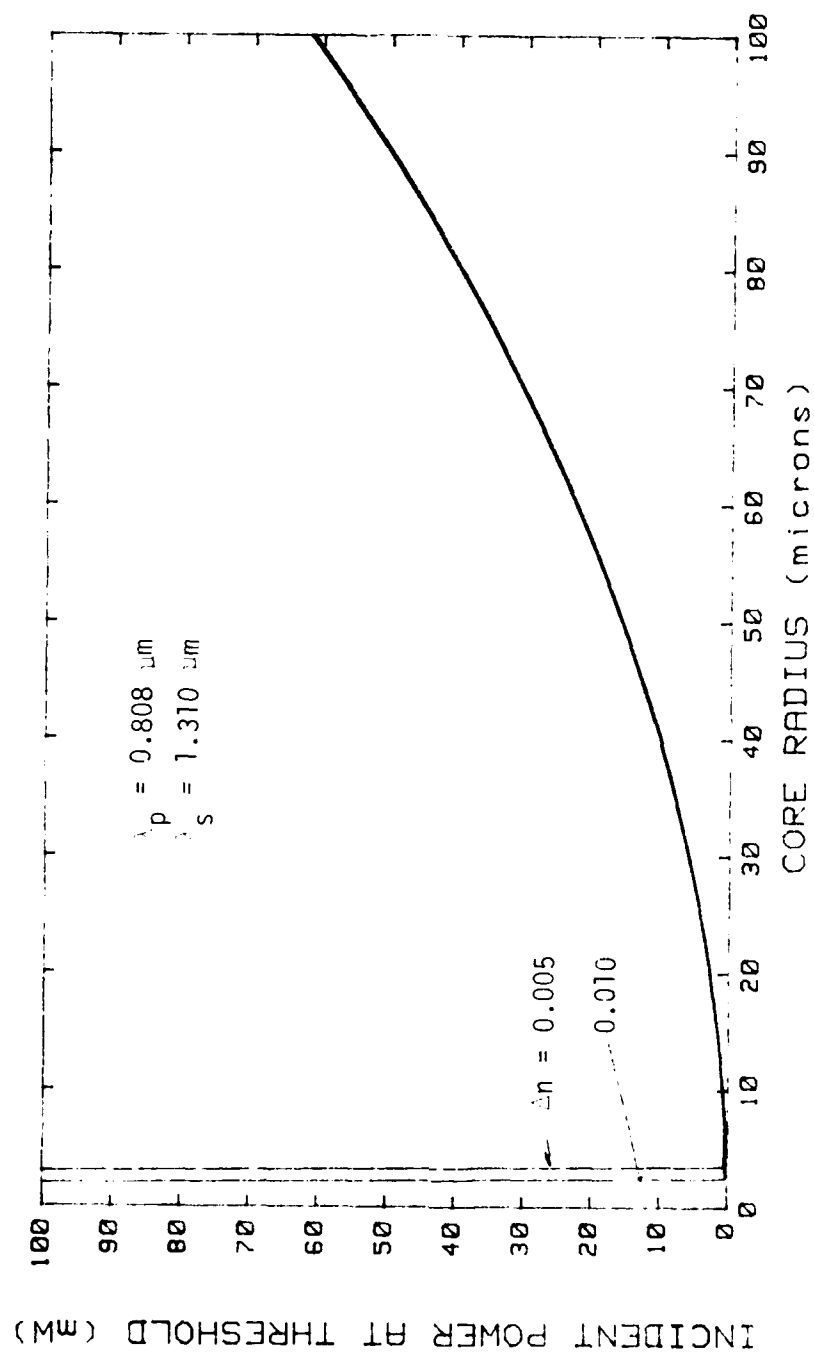


Figure 6 - Incident Threshold Pump Power versus Core Radius ( $\lambda_p = 808 \text{ nm}$ ).

# SLOPE EFFICIENCY vs CORE RADIUS

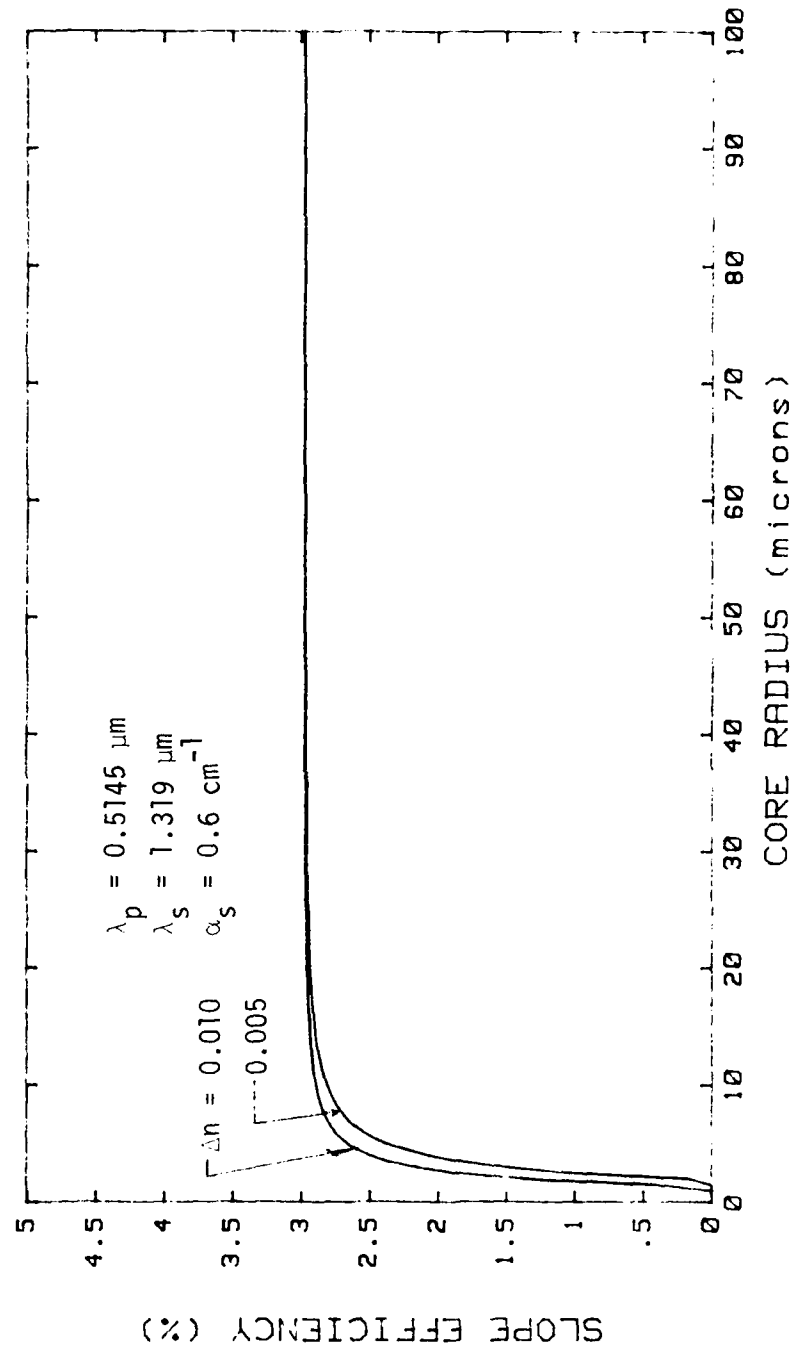


Figure 7 - Slope Efficiency (with respect to Incident Power) versus Core Radius.

# SLOPE EFFICIENCY VS CORE RADIUS

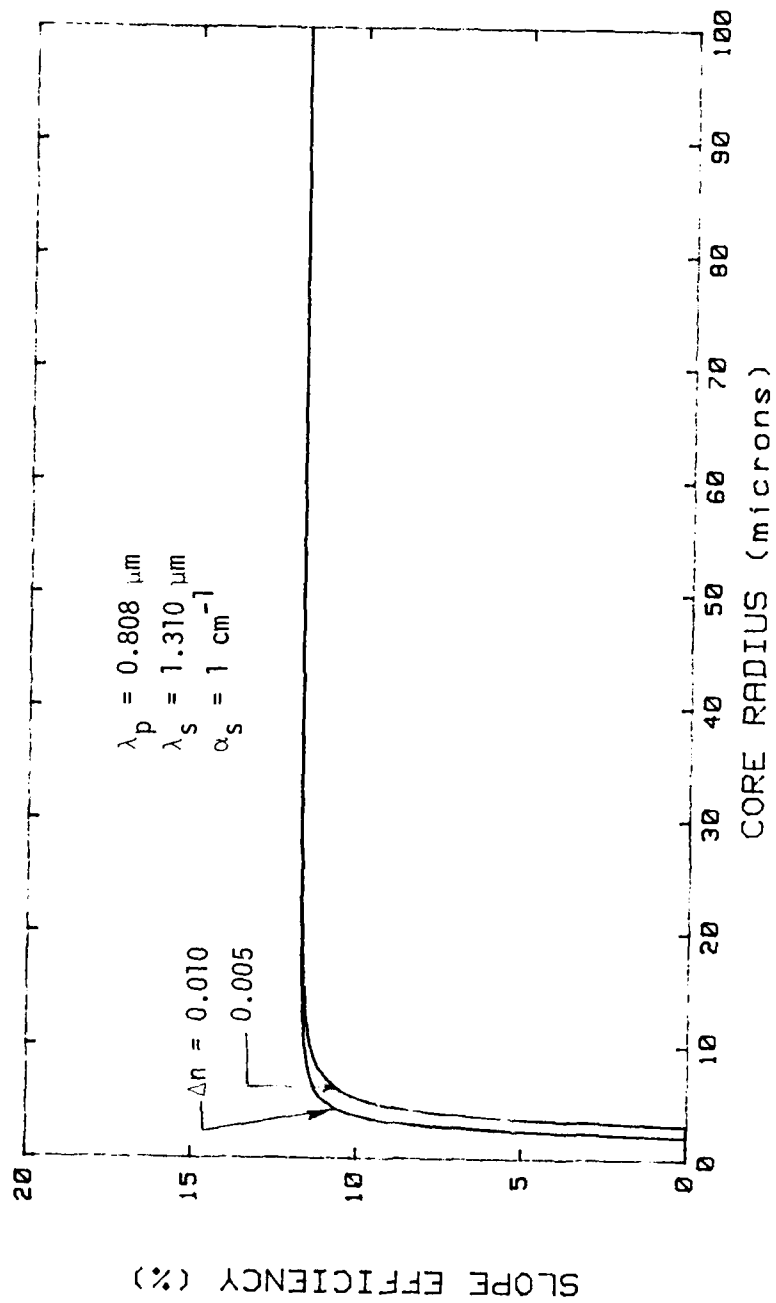


Figure 8 - Slope Efficiency versus Core Radius ( $\lambda_p = 808 \text{ nm}$ ).



pumping the slope efficiency is lower because (1) the fraction of absorbed pump power at this wavelength is lower and (2) the pump wavelength is also lower.

#### 4. Summary

The slope efficiency is fairly constant for values of the core radius greater than about  $5 \mu m$  ( $V \approx 3$ ). This is close to the region of inherently single mode operation of the waveguide. Slopes of 5-10% can be reasonably expected.

Threshold pump power coupled into the fiber is in the sub-milliwatt range for an optimum  $V$  - number of about 2.2 for  $\lambda_p = 0.5145 \mu m$  and about 2.8 for  $808 nm$  pumping. As the  $V$  - number is decreased below the optimum value the threshold pump power increases rapidly. As it is increased above this value the threshold pump power increases quadratically with the fiber core radius.

In summary, a fiber with a  $V$ -number of 2-3 is optimum for  $1.32 \mu m$  Nd:YAG fiber laser operation. This means that the best device performance is expected for waveguides that are close to being single mode.

### IV. ARGON LASER PUMPED Nd:YAG LASERS

#### A. MINIATURE BULK LASERS

##### 1. Laser Cavity

Laser mirrors and a small Nd:YAG crystal, described in Part 3a of this section, were placed together to form a laser resonator (see Figure 9). Each laser mirror was held by a gymbol mount which provided for tilt adjustment using micrometers and a lever arm action. Each gymbol mount was attached to an orthogonally aligned pair of linear translation stages which made it possible to position the mirror horizontally, as well as longitudinally. This allowed for a greater flexibility in cavity alignment over the setup used for  $1.064 \mu m$  laser work. The laser crystal holder was attached to an  $x$ - $y$  positioner which is used to position the crystal in the pump beam. All of the translation stages were attached to a solid block of aluminum for better mechanical stability.

Curved mirrors ( $R = 10 cm$ ) were obtained from an outside manufacturer for use in the  $1.32 \mu m$  miniature bulk laser experiments. One mirror was a high reflector (HR) while the other was a 1% output coupler. Mirror transmission at the pump wavelengths of  $0.5145 \mu m$  and  $0.808 \mu m$  should be greater than 75%, typically 95%, according to the

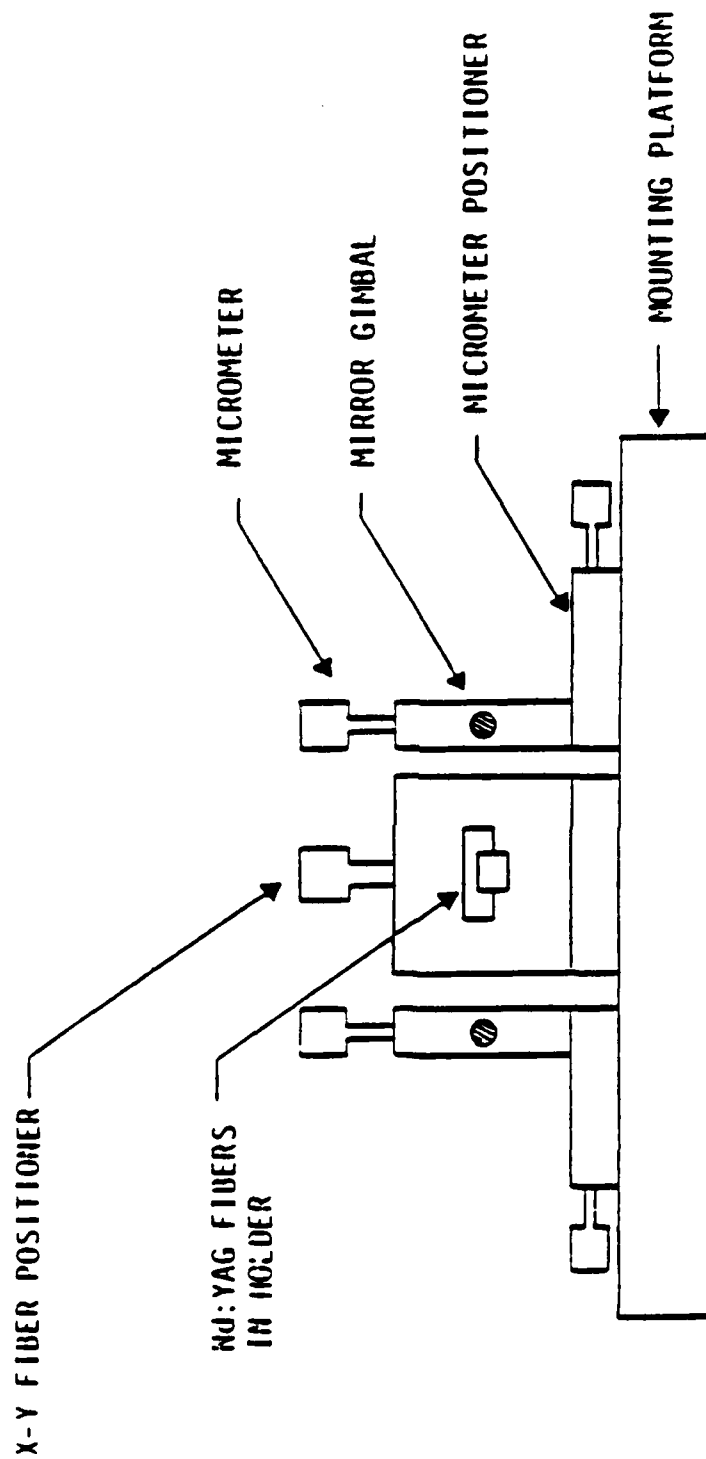


Figure 9 - Schematic of the Laser Cavity.

manufacturer. Transmission at  $0.5145\ \mu\text{m}$  was experimentally determined to be 86% and 94% for the high reflector and output coupler, respectively.

## 2. Experimental Arrangement

A schematic of the experimental arrangement is given in Figure 10. The  $5145\ \text{\AA}$  line of an argon ion laser was directed longitudinally into the laser cavity through the high reflector using a lens for mode matching purposes. The pump power was monitored by diverting a portion of the pump beam into a calibrated EG&G large area silicon detector via a beamsplitter (microscope slide). No filter was required here to block the  $1.32\ \mu\text{m}$  radiation from the Nd:YAG laser since silicon does not respond to this wavelength. Most of the  $1.32\ \mu\text{m}$  energy was passed through the beamsplitter and impinged onto a large area ( $1\ \text{cm}^2$ ) germanium detector. A neutral density filter was placed in front of the detector to attenuate the  $1.32\ \mu\text{m}$  laser beam and avoid saturating the detector. The pump beam was eliminated using a color filter. The transmission of the filters and the beam splitter at both pump and signal wavelengths was calibrated using a Perkin Elmer model 330 spectrophotometer. The Fresnel reflection ( $\lambda = 0.5145\ \mu\text{m}$ ) at each Nd:YAG crystal end-face was determined to be about 13%. Knowledge of the transmission of these optical elements along with the pump beam absorption coefficient for Nd:YAG ( $.6\ \text{cm}^{-1}$ ) yielded a fairly accurate estimate of the absorbed pump power.

The germanium detector was calibrated for  $1.32\ \mu\text{m}$  by measuring its response at  $1.064\ \mu\text{m}$  using a commercial Nd:YAG laser. The actual power at  $1.064\ \mu\text{m}$  was measured with a calibrated EG&G detector. The output current from the germanium detector was multiplied by a factor of  $\frac{4}{5}$  in order to obtain the desired calibration at  $1.32\ \mu\text{m}$ . This factor was determined by comparing the relative response of germanium at  $1.32\ \mu\text{m}$  and at  $1.064\ \mu\text{m}$ , available in the literature.<sup>19</sup>

## 3. Laser Measurements

### a. Laser Crystals

A total of three small crystals of Nd:YAG, labelled #1 through #3, were prepared for laser evaluation. These crystals, approximately  $2 \times 2 \times 8\ \text{mm}$  were polished with their end-faces parallel to each other. The surface flatness was better than  $\frac{\lambda}{4}$  in all cases. These samples were anti-reflection (AR) coated for normal incidence at  $\lambda = 1.319\ \mu\text{m}$  with a single layer of  $\text{MgF}_2$  (index of refraction  $\approx 1.38$ ) approximately  $2390\ \text{\AA}$  thick. Theoretical

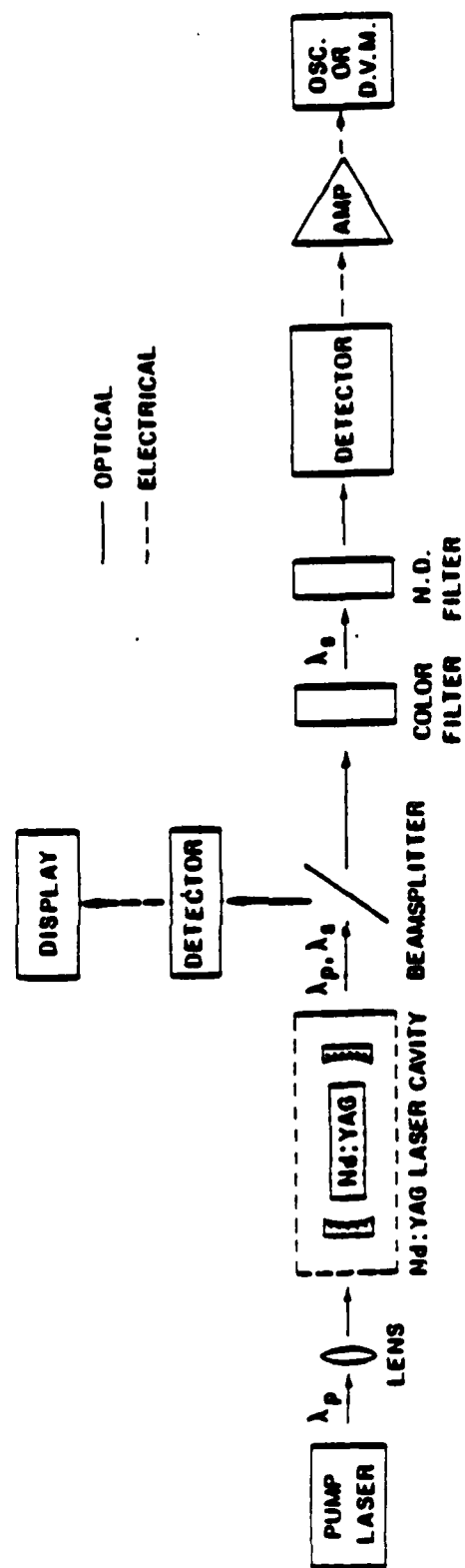


Figure 10 - Diagram of the Experimental Arrangement for Miniature Nd:YAG Laser.

calculations indicate that Fresnel reflection losses at  $1.319\ \mu\text{m}$  should be limited to less than 0.1% per end-face resulting in a contribution to the total round-trip laser cavity loss of less than 0.4%. The coating reflectivity at the pump wavelengths of  $0.5145\ \mu\text{m}$  and  $0.808\ \mu\text{m}$  was expected to be on the order of 5%. The actual reflectivity at  $0.5145\ \mu\text{m}$  was experimentally determined to be closer to 13% for crystal #1. This was measured by slightly tilting ( $\approx 4^\circ$ ) an AR coated crystal with respect to a probe beam and measuring the incident and reflected power with a silicon detector.

The absorption coefficient for laser crystal #3 was measured to be  $0.45\ \text{cm}^{-1}$ , which is the same value obtained for crystal #2 and close to that of laser crystal #1. This is not surprising since all three crystals were obtained from the same Nd:YAG boule. The lower value of the absorption coefficient compared to the expected  $0.6\ \text{cm}^{-1}$  means that the concentration of Nd ions in these samples may be slightly lower than the standard 1% level.

#### b. Laser Characterization

Laser oscillation at  $1.32\ \mu\text{m}$  was successfully demonstrated with all three miniature bulk laser crystals. A plot of output power versus absorbed pump power is presented in Figure 11 for crystal #1. The threshold occurred at about 27.2 mW of absorbed pump power (61 mW incident to the laser crystal) while the slope efficiency (referred to absorbed pump power) was determined to be 18.8% using a linear regression algorithm (the threshold data point was not used in the slope efficiency calculation because of the ambiguity involved in determining precisely when the onset of lasing occurs). A parameter known as the coefficient of determination indicates the quality of the curve fit achieved by the regression. This parameter may vary between 0 and 1.00 with values close to 1.00 indicating a better fit than values close to zero. In this case the coefficient of determination is 0.998 which shows that the data is highly linear, as expected. The waist of the pump beam was calculated to be approximately  $17.4\ \mu\text{m}$  and was obtained using a 9.8 cm focal length lens. Note that this waist radius is in the range of optimum operation as shown in Part c2 of Section III.

A set of data was also taken with a 17.2 cm focal length lens ( $32.8\ \mu\text{m}$  waist radius), as shown in Figure 11. The absorbed pump power at threshold was 42.9 mW while the measured slope efficiency was 23.4%. A value of 0.999 for the coefficient of determination indicates again the excellent linearity of the response.

Crystal #2 yielded the best results with a threshold of approximately 19.4 mW of absorbed pump power, and a slope efficiency of 36% which is close to the maximum

# INPUT/OUTPUT POWER CURVE

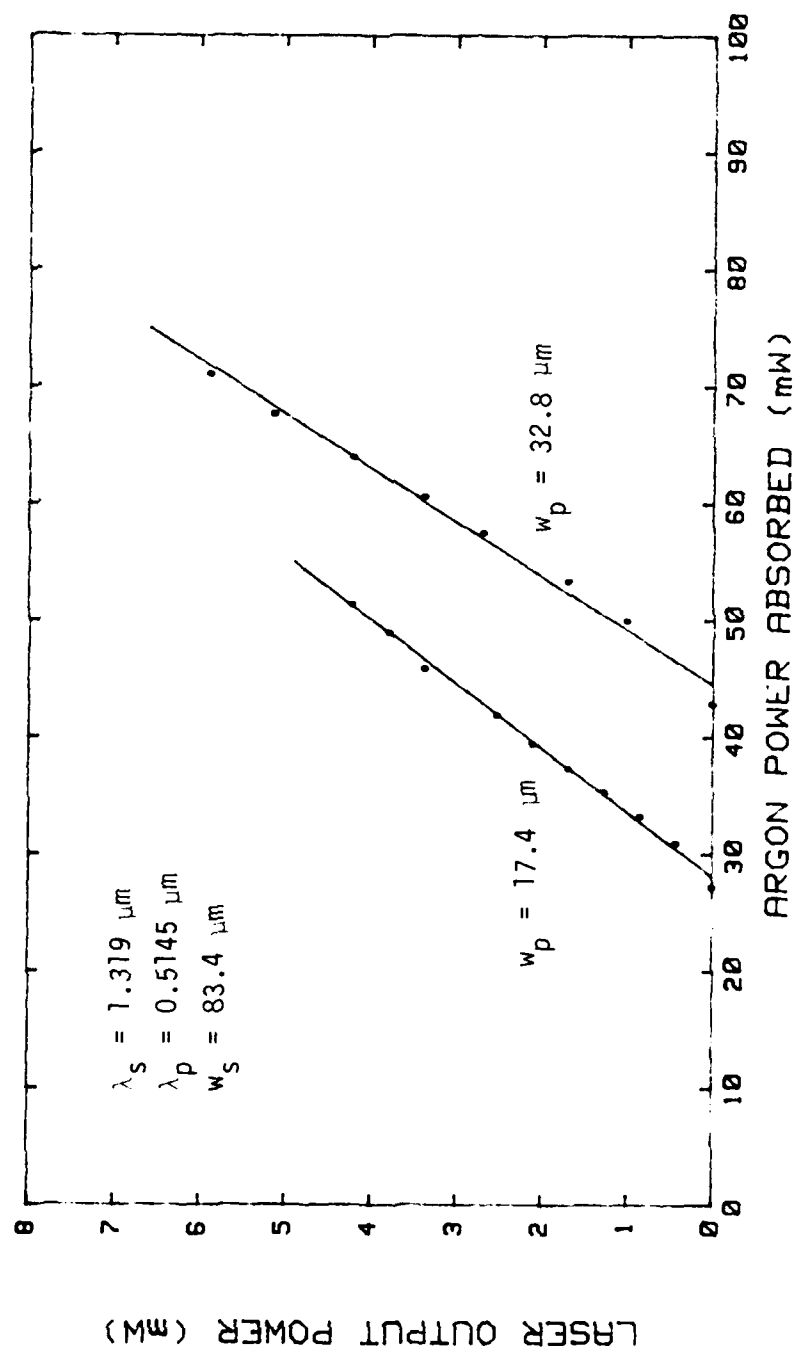


Figure 11 - Laser Output Power Versus Absorbed Pump Power for Crystal #1.

**Table 1.**  
**Summary of Results for Bulk Lasers**

<i>Crystal</i>	$w_p(\mu m)$	$w_s(\mu m)$	$s_{meas}$	$\delta_{1,inferred}$	$P_{th,meas}(mW)$	$\sigma_{inferred}(cm^2)$
1	17.4	83.4	0.1880	0.021	27.2	$0.78 \times 10^{-19}$
1	32.8	83.4	0.2344	0.017	42.9	$0.42 \times 10^{-19}$
2	17.4	79.5	0.3604	0.011	19.4	$0.53 \times 10^{-19}$
3	17.4	79.5	0.1485	0.026	24.8	$0.98 \times 10^{-19}$

theoretical value of 39% in the limit of zero internal cavity loss (See Equation (15)). The high slope efficiency of this laser indicates a very low internal round-trip loss of about 0.1%. The total cavity length in this case was shortened to 8.0 mm from the 9.0 mm length used with crystal #1 which slightly decreased the signal waist in the 7.5 mm long crystal to 79.5  $\mu m$ . The waist of the pump beam was 17.4  $\mu m$ . A plot of the laser output power versus absorbed pump power is given in Figure 12.

Crystal #3 was also tested using the same parameters for the cavity and pump beam as for laser crystal #2. The data indicate a threshold of 24.8 mW absorbed by the crystal and a slope efficiency of 14.9% which infers an internal loss of about  $2.6\% - 1.0\% = 1.6\%$  for the cavity.

#### c. Interpretation

The results obtained for these miniature bulk lasers have been summarized in Table 1. Estimates of the laser gain cross-section at 1.32  $\mu m$  based upon these measurements are also listed in the table. These estimates were calculated by first deducing the total round-trip loss from the measured slope efficiency (Equation (15)) and then using this value of the cavity loss along with the measured threshold pump power to determine  $\sigma$  (Equation (11)). The effective pump area  $A_p^*$  used in these calculations was estimated using Equation (19). The average value of these estimates is  $\sigma = 0.68 \times 10^{-19} cm^2$ . It should be noted that any error made in the estimate of the absorbed pump power affects the threshold pump power and the total cavity loss in the same way so that this effect cancels itself in the expression for threshold pump power (Equation (11)) which is used to determine the gain cross-section.

#### B. FIBER LASERS

# INPUT/OUTPUT POWER CURVE

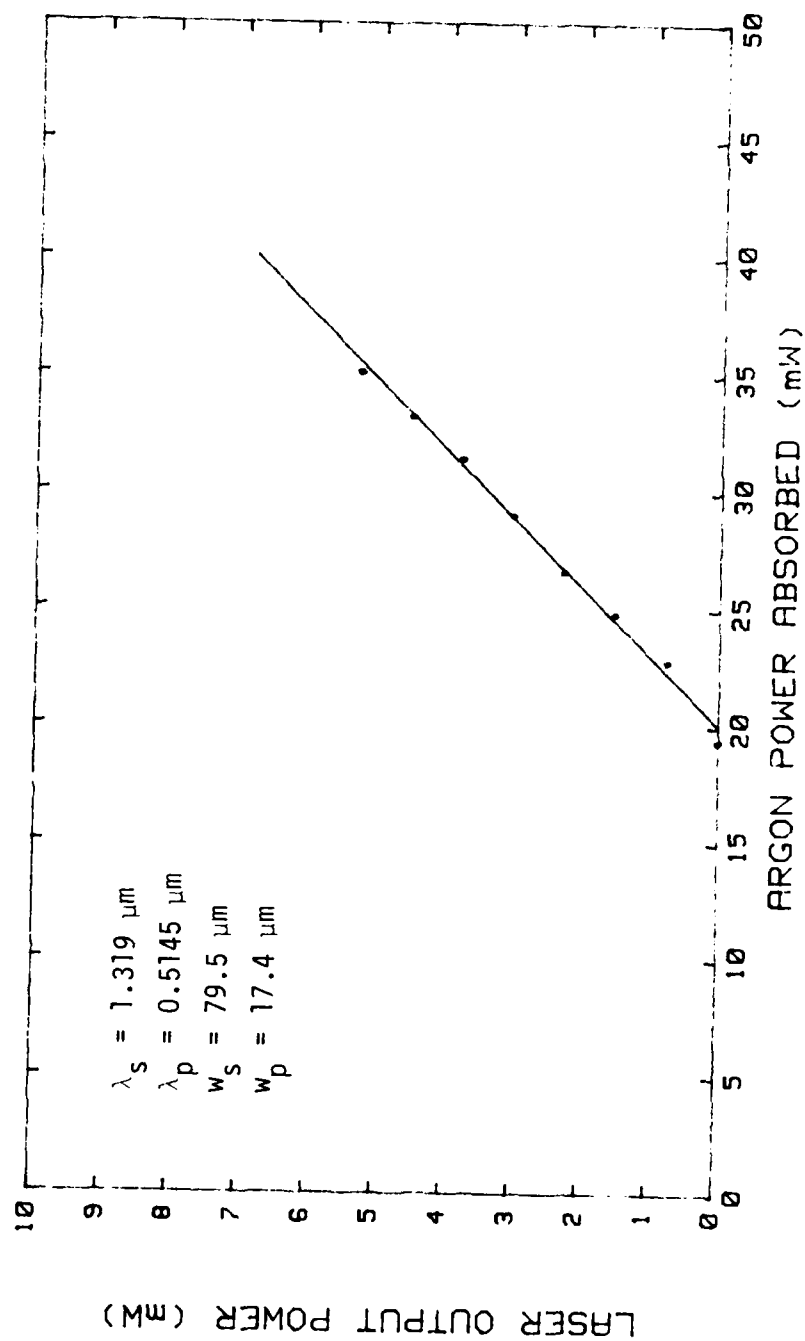


Figure 12 - Laser Output Power versus Absorbed Pump Power for Crystal No. 2.



## 1. CW Argon Pumping

### a. Experimental Procedure

Reflection coefficients for the coated end-faces of array #17 at the pump wavelength of  $0.5145\ \mu\text{m}$  were measured with the same procedure described in Part 3a of Section IV for miniature bulk lasers and found to be approximately 7.5% per end-face. Fiber array #17 was then placed in the laser cavity shown in Figure 9, for laser evaluation. Laser experiments were begun using the arrangement depicted in Figure 10. An argon laser operating at  $0.5145\ \mu\text{m}$  served as the pump source.

The pump beam was aligned through a fiber by observing the output of the fiber on a distant screen after first passing through a short focal length collimating lens placed near the fiber. Placing another short focal length lens on the input side of the fiber to expand the beam incident to the array produced a magnified image of the fibers and the slot on the screen. By moving this lens in and out of the path of the argon laser beam one could determine which fiber the pump beam was passing through and also if it was passing through unobstructed. All of the fibers appeared to transmit the pump beam reasonably well. Since the pump beam waist was about  $17.4\ \mu\text{m}$  (obtained using a  $9.8\ \text{cm}$  focal length lens), with a Rayleigh range of approximately  $3.4\ \text{mm}$  in Nd:YAG, the beam radius at either end-face of a fiber in this array should have been about  $26\ \mu\text{m}$  if the waist was located at the center of the fiber lengthwise. Thus, the pump beam could fit within the  $170\ \mu\text{m}$  diameter fibers without experiencing any guidance effect from the fibers.

To test the AR-coatings the array was displaced so that the pump beam passed through the Nd:YAG mounting jig to form a miniature bulk laser. Laser oscillation was easily achieved in the bulk with reasonable thresholds in the range of about  $50\ \text{mW}$  of absorbed pump power indicating adequate coatings.

After first aligning the tilt of the fiber so that the back reflection of the pump beam from the input face of the array was directed along the incident beam, the fiber was positioned transversely in the pump beam to obtain the best output spot from the fiber. This was done at low pump power levels in order to avoid burning the epoxy. The mirrors were then brought to within  $500\ \mu\text{m}$  of the end-faces of the fiber. With the argon pump power set at a minimum (so that the argon laser is near threshold) the back (HR) mirror of the fiber laser cavity was adjusted so that the reflected pump beam from this mirror was feeding back into the argon laser cavity. This always resulted in a slight enhancement of the argon laser output power. The pump power was then increased to well past the expected threshold value and the output coupler mirror adjusted until laser oscillation was

obtained.

#### b. Laser Measurements

Initial efforts to observe laser oscillation at  $1.319\ \mu\text{m}$  in the fibers of this array consisted of *cw* pumping a fiber with incident pump powers up to  $750\ \text{mW}$ . In order to avoid burning the epoxy, the argon laser beam was first aligned through a fiber at a low power level and then slowly increased. For preliminary tests the laser cavity employed the same  $10\ \text{cm}$  radius of curvature laser mirrors that were used for the miniature bulk lasers, with an output coupler transmittance of 1%. The mirrors were placed as close as possible to the ends of the array resulting in a  $10\ \text{mm}$  mirror separation.

Pulsed pumping was also attempted. In the pulsed pumping a chopper was used to provide a pulsed pump beam which allowed higher peak pump powers on the order of  $1.5\ \text{W}$  to be used, while maintaining an average power of about  $750\ \text{mW}$  to avoid damage to the fiber and/or coatings. The chopper frequency was about  $2\ \text{kHz}$  with a 50% duty cycle.

No laser action was observed in any of the fibers in either case. A calculation of the signal waist diameter (for an unguided device) showed that it was approximately equal to that of the fiber ( $170\ \mu\text{m}$ ), so that the signal probably experienced additional loss from aperturing by the fiber. On the other hand, if the signal propagated as a guided mode of the fiber it would have had a spot size of about  $110\ \mu\text{m}$  in diameter. A  $10\ \text{cm}$  radius of curvature mirror placed approximately  $500\ \mu\text{m}$  from the end of such a fiber would support a free space mode with a waist of  $110\ \mu\text{m}$  diameter located at the fiber end-face, so that laser action could have been possible in principle but was not observed.

The curved laser mirrors were then abandoned in favor of flat laser mirrors. This led to our first successful demonstration of a fiber laser operating at  $1.319\ \mu\text{m}$ . In this configuration the transmission of the flat output coupler was 1% while the other flat mirror was a high reflector. Fabrication of the flat laser mirrors was accomplished by deposition of multilayer dielectric coatings onto a  $1/2\ \text{mm}$  glass etalon. This was done as a custom order by an outside manufacturer. The mirrors were mounted on a  $0.5\ \text{inch}$  diameter aluminum cylinder with glue. The cylinder was then placed into the same mirror gimbal assembly that was used for the curved mirrors. A  $1\ \text{mm}$  diameter hole bored through the center of the aluminum cylinder provided passage for the pump and signal beams. Measurements showed that the pump beam transmission was about 66% for the output coupler and 71% for the high reflector. It should be noted that these values were much lower than those obtained for the curved mirrors.

Laser oscillation at  $\lambda = 1.319\ \mu\text{m}$  was first achieved in fiber #17-4. A plot of the laser

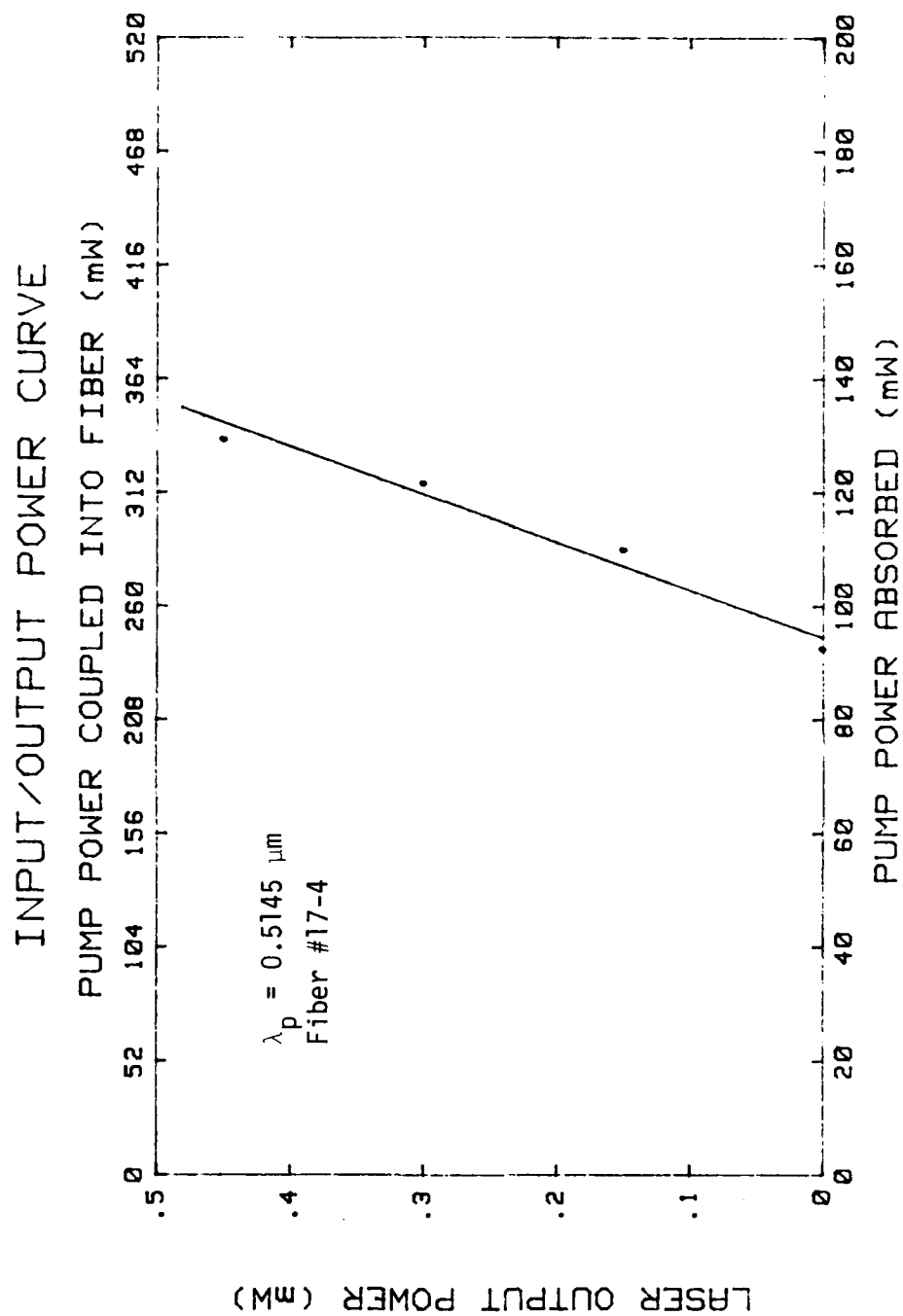


Figure 13 - Output Power versus Pump Power using a 1-Minute Rest Interval between Data Points.

output power versus pump power is presented in Figure 13. The estimated absorbed pump power at threshold was, 92.5 *mW*, corresponding to approximately 240 *mW* input into the fiber. Linear regression indicates a slope efficiency of 1.5% with respect to absorbed pump power and reasonably good linearity of the data. Total cavity loss, inferred from the slope efficiency, is  $\delta_1 = .26$ . The output power from the fiber laser was observed to vary slowly in time (on the order of a few seconds) for a fixed pump power level. This was found to be due to thermal effects from the high incident pump power required to obtain laser oscillation in the fiber. The data points shown in Figure 13 were obtained by momentarily increasing the pump power to some value above the threshold and noting the output power from the fiber laser before decreasing the pump power back to a minimum level. The interval between individual data points for this case was about 1 minute.

A set of data, presented in Figure 14, was taken without any rest interval between data points. No significant change was observed (the increased threshold was probably due to a less than optimal cavity alignment).

Laser oscillation was also obtained in fiber #17-3 with approximately the same threshold level. Unfortunately, the stability of the output power was not good enough to allow data to be taken. No laser oscillation was obtained in any of the other three fibers in the array using *cw* pumping.

### c. Interpretation

Table 2 lists the various measured and calculated laser parameters obtained from the measurements described in the previous section. In order to estimate the gain cross-section, the effective pump area  $A_p^*$  was first determined using Equation (19). The pump beam was assumed to be unguided with a waist radius of 17.4  $\mu\text{m}$  or an average waist radius of  $\bar{w}_p = 32 \mu\text{m}$  and the average signal waist radius was taken to be that of the guided ( $LP_{01}$ ) signal mode ( $\bar{w}_s = 59 \mu\text{m}$ ). This approach yields a value of  $A_p^* = 6.9 \times 10^{-5} \text{ cm}^2$ , and  $1.55 \times 10^{-10} \text{ cm}^2$  for the cross-section. This value of  $\sigma$  should be viewed as an upper bound on the cross-section. Since it is a factor of two larger than the value of  $\sigma$  measured in bulk Nd:YAG 1.32  $\mu\text{m}$  lasers ( $\sigma_{\text{bulk,ave}} = 068 \times 10^{-10} \text{ cm}^2$ ), it suggests that the signal waist is actually smaller than that of the  $LP_{01}$  mode, and that another guiding mechanism may be present, as was observed in earlier work with 1.064  $\mu\text{m}$  fiber lasers.<sup>9</sup>

Here it is noted that much lower threshold pump power levels were also obtained, on the order of 50 *mW* absorbed, but the cavity alignment was not stable. These transient observations were consistent with a cavity loss of approximately 14% round-trip indicating that at least 45% of the round-trip laser cavity losses listed in Table 2 was attributable

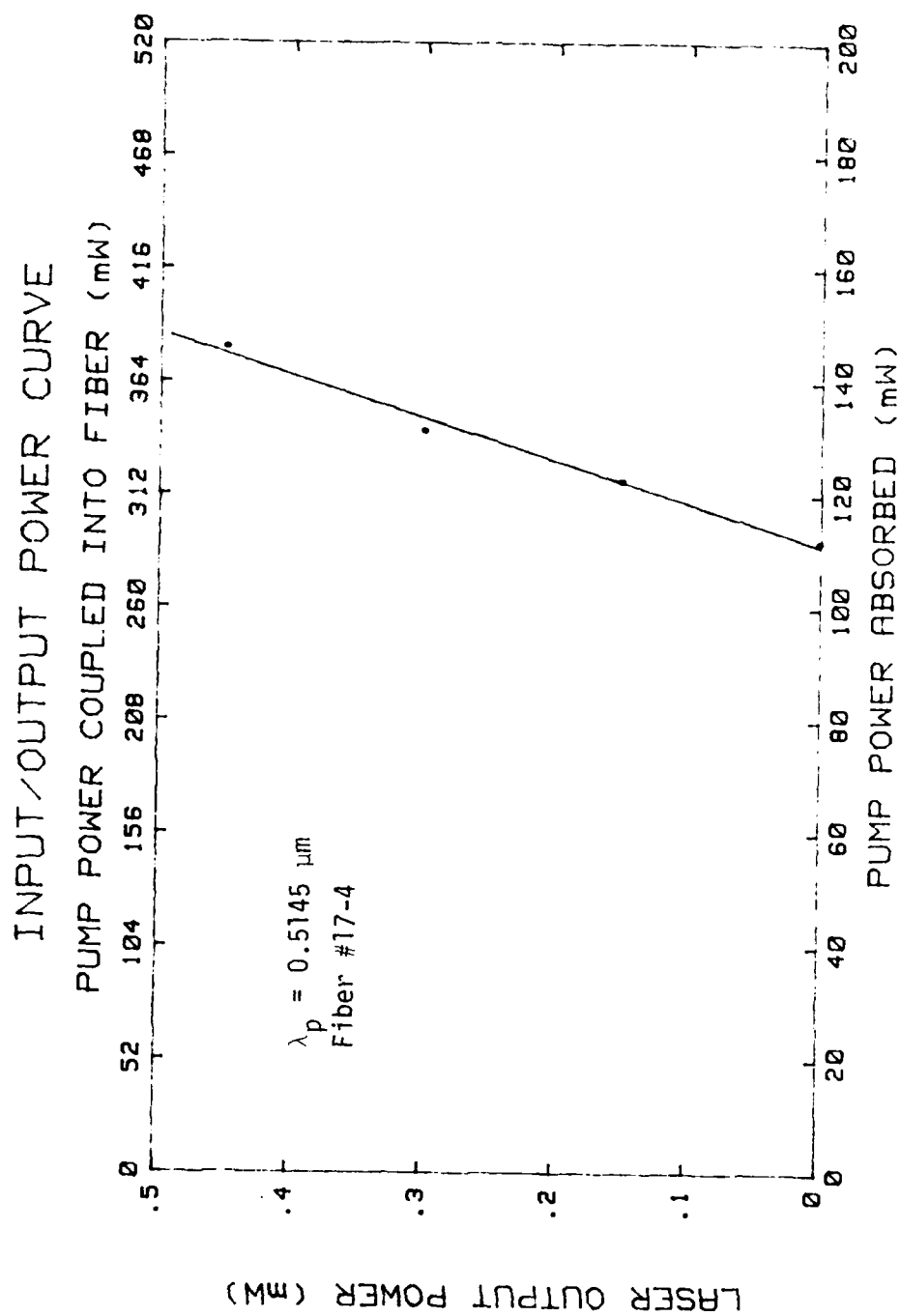


Figure 14 - Output Power versus Pump Power with no Rest Interval between Data Points.

**Table 2.**  
**Summary of Results for Fiber #17-4**

$\Delta t_{rest} (min)$	$s_{meas}$	$\delta_{1,inferred}$	$A_p^*(cm^2)$	$P_{th,meas}(mW)$	$\sigma_{inferred}(cm^2)$
0	0.0126	0.310	$1.094 \times 10^{-4}$	111.9	$1.41 \times 10^{-19}$
1	0.0152	0.257	$1.094 \times 10^{-4}$	92.5	$1.41 \times 10^{-19}$
5	0.0128	0.305	$1.094 \times 10^{-4}$	114.8	$1.35 \times 10^{-19}$

to a less than optimum cavity alignment. Output power levels of over 5 mW were also obtained but the power level would quickly drop due to thermal effects in the laser cavity.

## 2. Pulsed Argon Pumping

### a. Experimental Procedure

After repeated experiments with fiber array #17 using a *cw* argon ion laser pump source ( $\lambda_p = 0.5145 \mu m$ ) it was no longer possible to achieve laser oscillation in any of the fibers of the array. Also, it was observed that the quality of the pump beam output from the fibers had considerably degraded. Optical microscope inspection of the fiber end-faces revealed that the AR coatings were partially removed, probably as a result of an improper manipulation.

The remainder of the coatings was then removed using a new procedure which involves a gentle scrubbing of the end-faces of the fibers with a Q-tip coated with tin oxide. This process takes only a few minutes (as opposed to hours of re-polishing as was done before) and does not appear to have any effect upon the state of polish of the fiber ends. The end-faces of the array were then cleaned using ethyl alcohol and lens paper, and new AR coatings deposited. A check of the transmission of the pump beam through the samples showed that the quality of the new coatings was quite good. Their measured power reflection coefficients at the pump wavelength were found to be close to 1%. This is much lower than in previous cases (7-20%) for both the fibers and the miniature bulk lasers and slightly lower than the theoretically calculated value of approximately 4%.

The original set of flat laser mirrors were also visually examined and found to contain spots in the coatings, probably caused by the high optical intensities used in testing the devices. Another possibility is that the glue used to hold the mirrors in place may have crept onto the coated surfaces when subjected to temperature increases caused by absorbed optical power.

A new set of flat laser mirrors were selected. Each of the new mirrors transmit about 87.1% of the pump beam. This is much higher than the transmission of the first set of flat laser mirrors (71% for the *HR* mirror, 66% for the *OC*) which is below the range of 75%-95% for  $\lambda = 0.5145 \mu m$  specified by the manufacturer. This discrepancy was unexpected since all mirrors of a particular reflectivity were cut from the same glass etalon. It may be due to a non-uniformity of the particle flux during deposition of the multilayer dielectric coatings onto the etalon. Mirrors selected from the perimeter of the etalon could then exhibit slightly different characteristics than mirrors taken from the central portion.

Upon completion of its reprocessing, fiber array #17 was placed into the current laser cavity along with the new set of mirrors. A chopper was added to the experimental set-up (before the focusing lens, see Figure 10) to reduce the duty cycle and thermal effects. The pulse width was about 0.315 msec and the pulse repetition frequency 70.4 Hz (14.2 msec period) which corresponds to a duty cycle of about 2.2%. The maximum average pump power delivered to the fibers was thus restricted to 24.2 mW (at the 1.1 W maximum cw output power then available from the argon laser).

Alignment of the sample and back (*HR*) mirror was accomplished first under cw conditions at low pump power in the usual way. The chopper was then turned on and the argon laser output power increased close to its maximum level of 1.1 W. Adjustment of the output coupler orientation quickly led to laser oscillation, first in fiber #17-4, and then in all four of the other fibers of the array. Unlike earlier work with cw pumped 1.32  $\mu m$  fiber lasers the output from the pulsed fiber lasers was very stable. This is believed to be due to the better quality optical components (coatings, mirrors) and much lower average pump power in the pulsed case reducing thermal effects in the laser cavity.

#### b. Laser Measurements

Plots of the output power versus pump power for fibers 17-3 and 17-4 are shown in Figures 15 and 16, respectively. The results of the pulsed experiments are much better than those obtained previously under cw pumping conditions. Measured slope efficiencies are in the range of 5-6% as opposed to 1.5% obtained earlier with cw pumping. The absorbed pump power at threshold is 19.6 mW for fiber #17-3 and 44.7 mW for fiber #17-4, an improvement over the best previous cw measurement (50 mW but unstable).

Measurements of the absorption coefficients of the other three fibers of fiber array #17 were completed, allowing the analysis of data taken from these fibers to proceed. The measured values are slightly lower than the absorption coefficients for fibers #17-3 and #17-4. They are listed in Table 3 along with data from fiber array #18. Although fibers

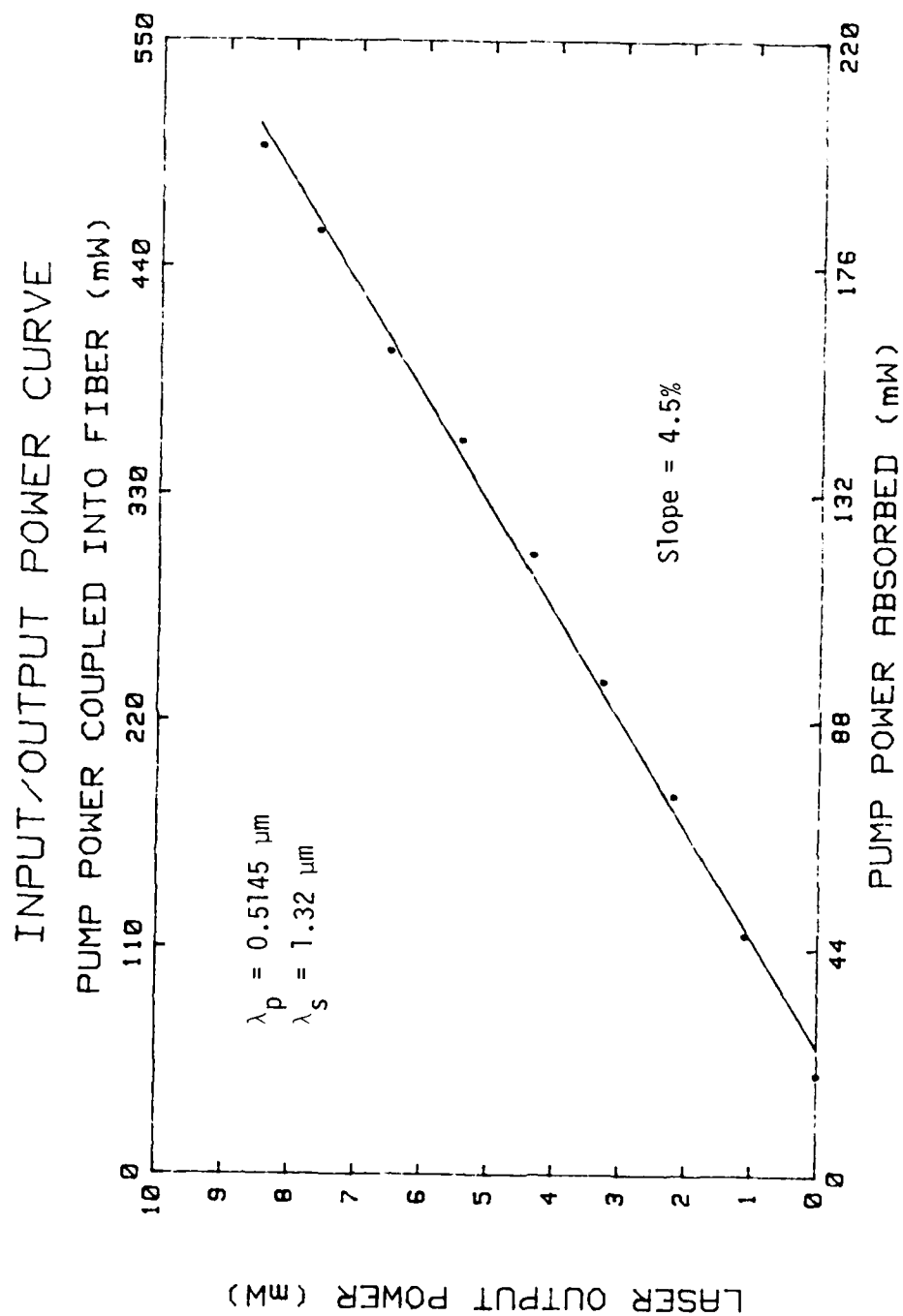


Figure 15 - Output Power versus Pump Power for Fiber #17-3.



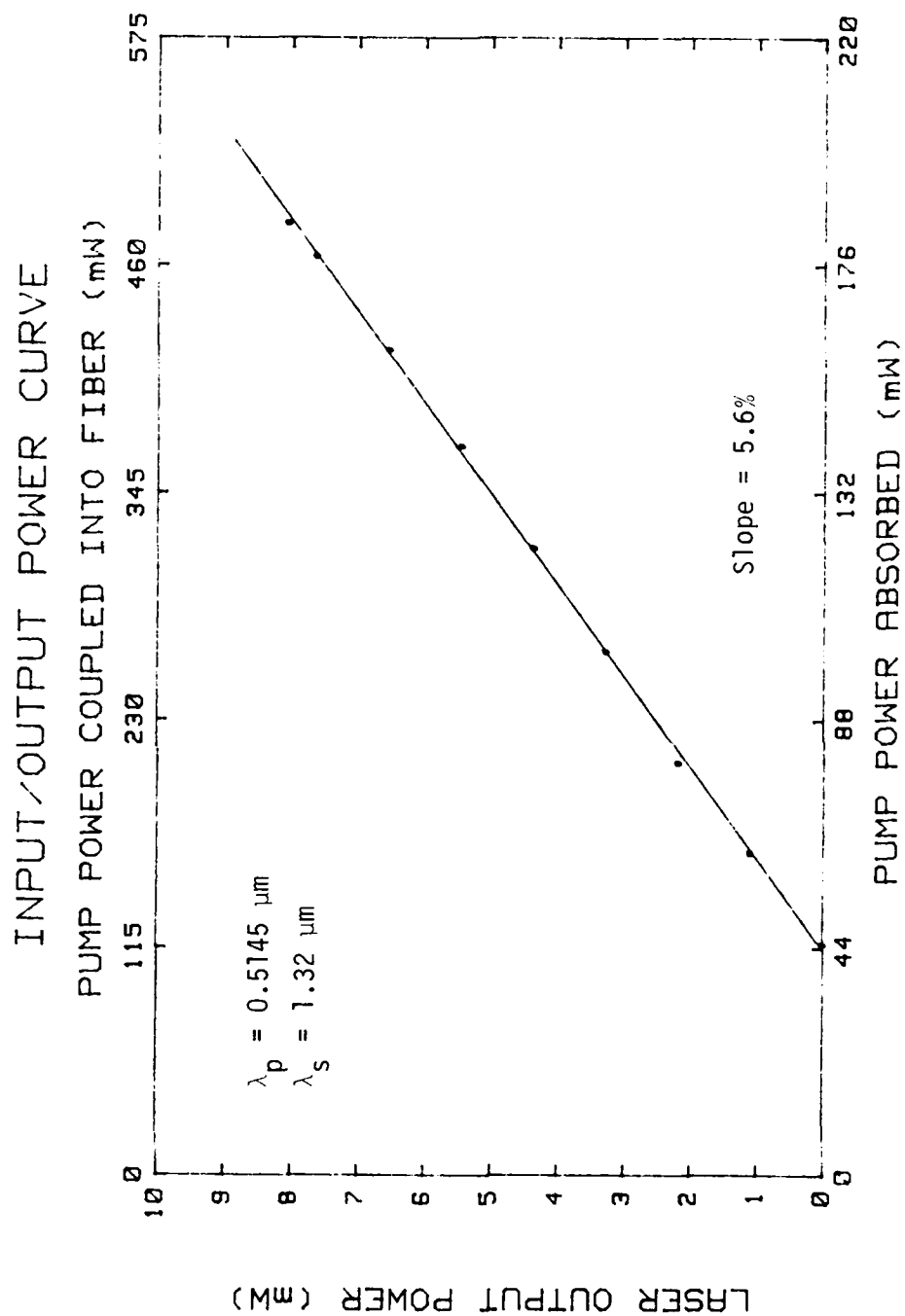


Figure 16 - Output Power versus Pump Power for Fiber #17-4.

Table 3.

## Measured Absorption Coefficients and Growth Rates

Fiber #	$\alpha_a$ ( $cm^{-1}$ )	Growth Rate (mm/min)
17-1	0.46	1/2
17-2	0.44	1/2
17-3	0.57	1/2
17-4	0.54	1/4
17-5	0.49	1/4
18-2	0.51	
18-4	0.51	

#17-4 and #17-5 were grown at a slower speed than the other three fibers in the array, their absorption coefficients do not appear to be distinctly different from those of the other fibers. The fiber lasers of array #17 were taken from the best sections of a longer fiber. Since the Nd ion concentration varies as the fiber is being grown a given section of the fiber is expected to have a slightly different Nd ion concentration than another section.

Table 4 summarizes the results obtained with fiber lasers from arrays #17 and #18. Threshold pump power for the fibers of array #17 ranged between 12 mW and 50 mW. Slope efficiencies varied from 4.9% for fiber #17-3 to 22.1% for fiber #17-1. Figure 17 shows a plot of the power output curve for fiber #17-1, which yielded the best 1.32  $\mu m$  fiber laser. The absorbed pump power at threshold was about 12.0 mW. The slope efficiency was 22%, less than a factor of two below the optimum value for .5145  $\mu m$  pumping. The maximum recorded output power was in excess of 20 mW, more than twice the previous maximum output power observed in fiber lasers. This data leads to an estimate of  $0.47 \times 10^{-19} cm^2$  for the gain cross-section compared to an average value of about  $0.67 \times 10^{-19} cm^2$  for the entire array. This is in excellent agreement with the average value of  $\sigma = 0.68 \times 10^{-19} cm^2$  measured in bulk 1.32  $\mu m$  Nd:YAG lasers. The effective pump area  $A_p^*$  used in the calculations for the cross-section was calculated using measured values of the signal mode radius (see Part c).

Laser action was obtained in two of the four fibers of array #18 (fiber diameter  $\approx 80 \mu m$ ). Only diffuse scattered pump light was observed at the output of the other two fibers, possibly due to a break in the fiber or poor crystal quality. The best result, plotted in Figure 18, was obtained using fiber #18-4. The measured slope efficiency in this case is just below 2%, about a factor of 3 better than that obtained using fiber #18-2. The lower values of  $A_p^*$  obtained for this array compensated for the higher loss and resulted

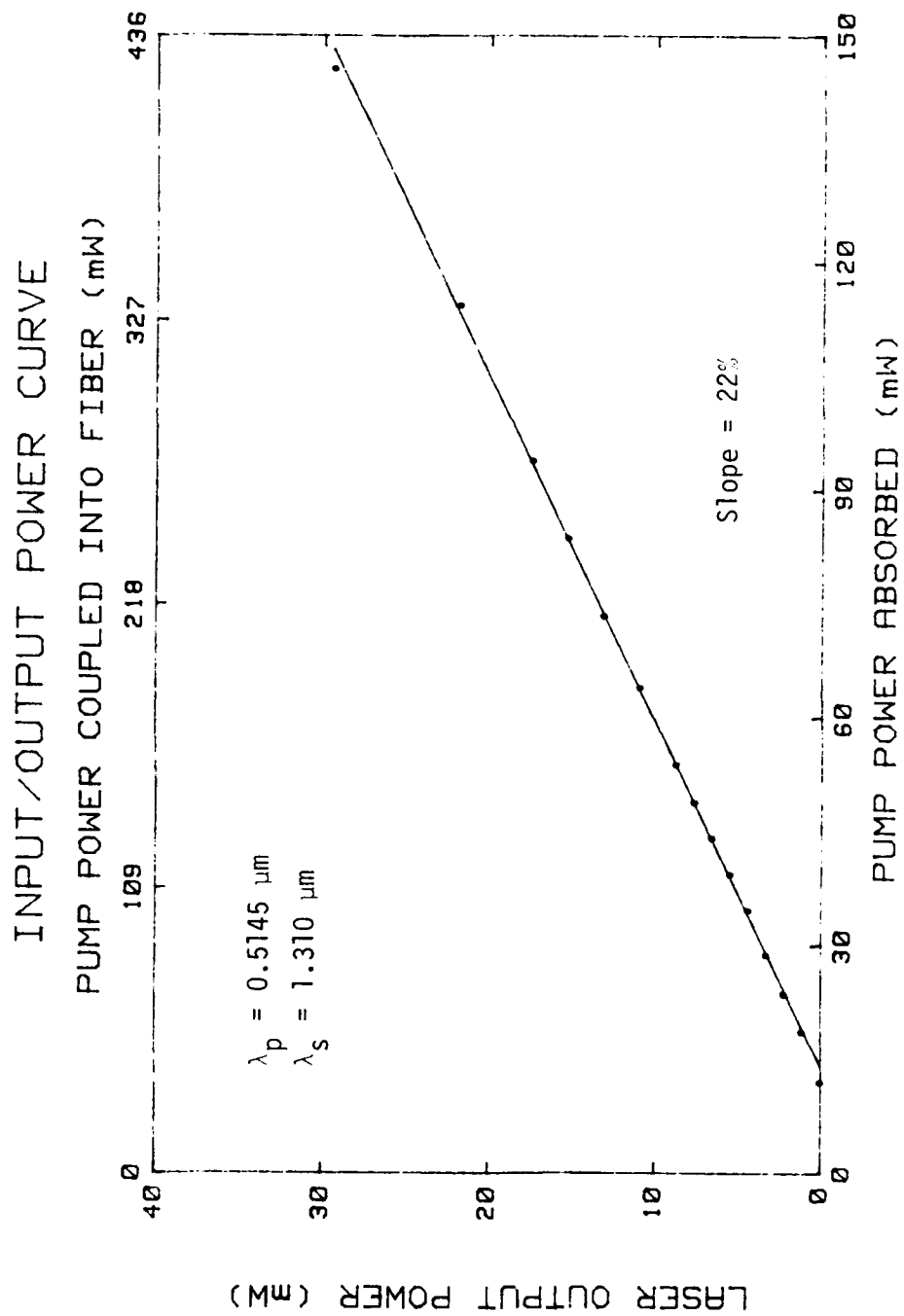


Figure 17 - Output Power versus Pump Power for Fiber #17-1.

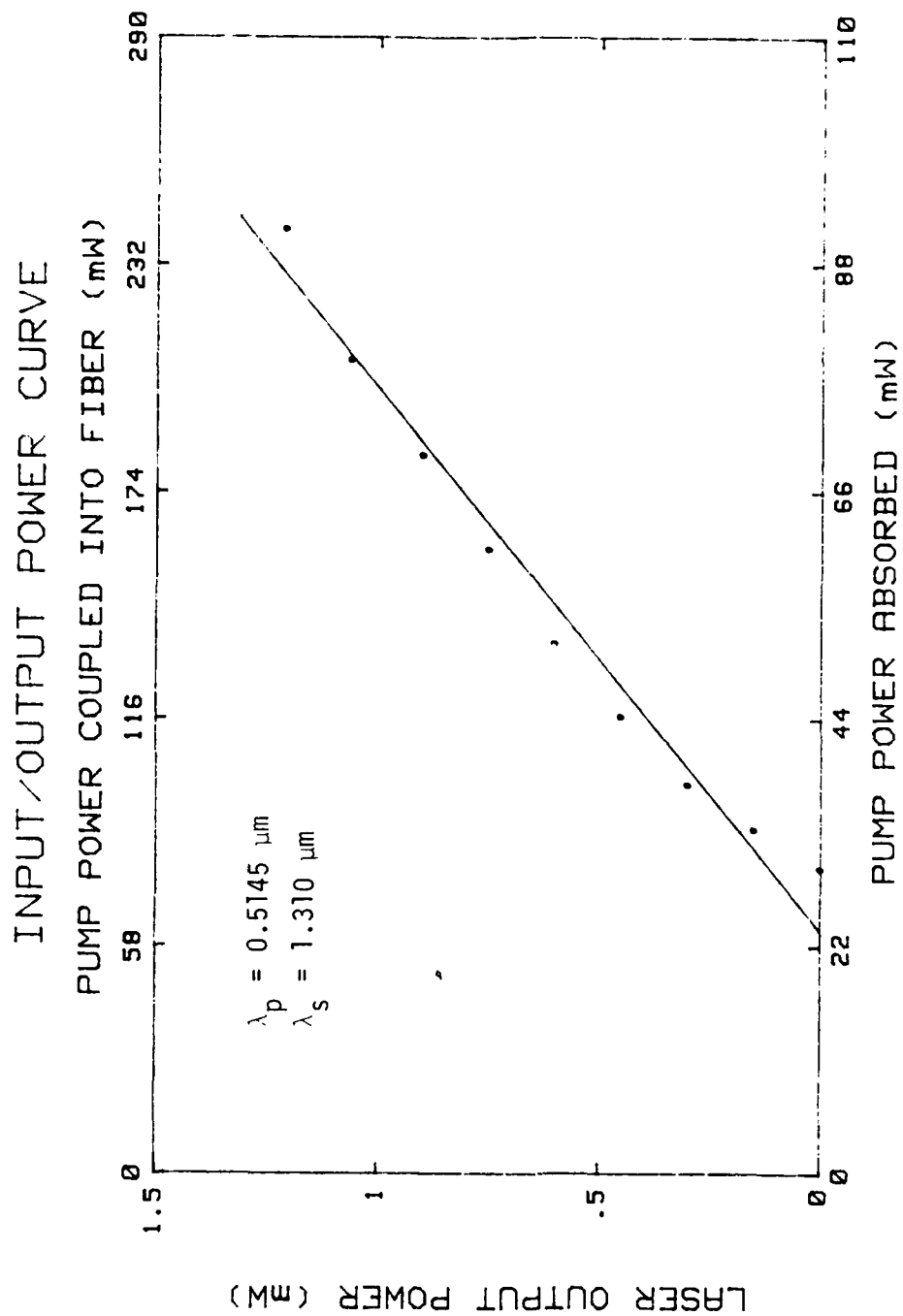


Figure 18 - Output Power versus Pump Power for Fiber #18-4.

**Table 4.**  
**Summary of Results for Arrays #17 and #18**

Fiber #	$s_{meas}$	$\delta_{1,inferred}$	$A_p^*(cm^2)$	$P_{th,meas}(mW)$	$\sigma_{inferred}(cm^2)$
17-1	0.2211	0.018	$3.945 \times 10^{-5}$	12.0	$0.47 \times 10^{-19}$
17-2	0.0868	0.015	$3.558 \times 10^{-5}$	19.8	$0.66 \times 10^{-19}$
17-3	0.0491	0.079	$4.324 \times 10^{-5}$	19.6	$1.43 \times 10^{-19}$
17-4	0.0564	0.070	$3.771 \times 10^{-5}$	44.7	$0.48 \times 10^{-19}$
17-5	0.0701	0.056	$3.220 \times 10^{-5}$	47.3	$0.31 \times 10^{-19}$
18-2	0.0062	0.628	$1.350 \times 10^{-5}$	32.3	$2.1 \times 10^{-19}$
18-4	0.0180	0.217	$1.271 \times 10^{-5}$	29.5	$0.77 \times 10^{-19}$

in relatively low pump power thresholds on the order of 30 *mW* absorbed for both fibers. A value of  $\sigma = 0.77 \times 10^{-19} \text{ cm}^2$  was obtained for fiber #18-4 and a larger value of  $2.1 \times 10^{-19} \text{ cm}^2$  for fiber #18-2.

#### c. Transverse Mode Profiles

The increased stability obtained under pulsed pumping conditions allowed the signal output mode profiles from the fiber lasers to be measured. A 50  $\mu\text{m}$  monochromator slit was placed in front of a large area (1  $\text{cm}^2$ ) Ge detector which was scanned across the signal output spot at a distance of approximately 9 inches from the fiber output end. Both vertical and horizontal scans were conducted at full pump power.

Representative traces from fiber #17-1 are shown in Figures 19 and 20. In all cases only a single (lowest order) transverse mode was observed, even at full pump power. This was expected on the grounds of gain and loss competition, as observed in earlier work on 1.064  $\mu\text{m}$  fiber lasers.<sup>9</sup> The modes look clean and symmetrical, possessing the near-Gaussian shape that one would expect. Also, there was very little astigmatism present (the residual astigmatism is probably due to measurement error). These results indicate that good coupling into a single mode fiber can be expected.

Table 5 contains a listing of the results of the scans of all five fibers of the array, as well as an estimate of  $A_p^*$ . The signal waist radii at the fiber output plane were calculated from the measured spot sizes. They are typically 42-50  $\mu\text{m}$ . This is lower than, yet in good agreement with, the theoretical value of 54  $\mu\text{m}$  for a 170  $\mu\text{m}$  diameter fiber.  $A_p^*$  was calculated using Equation (19), a pump waist radius of 17.4  $\mu\text{m}$  ( $\bar{w}_p = 32 \mu\text{m}$ ), and the average radius from the horizontal and vertical measurements.

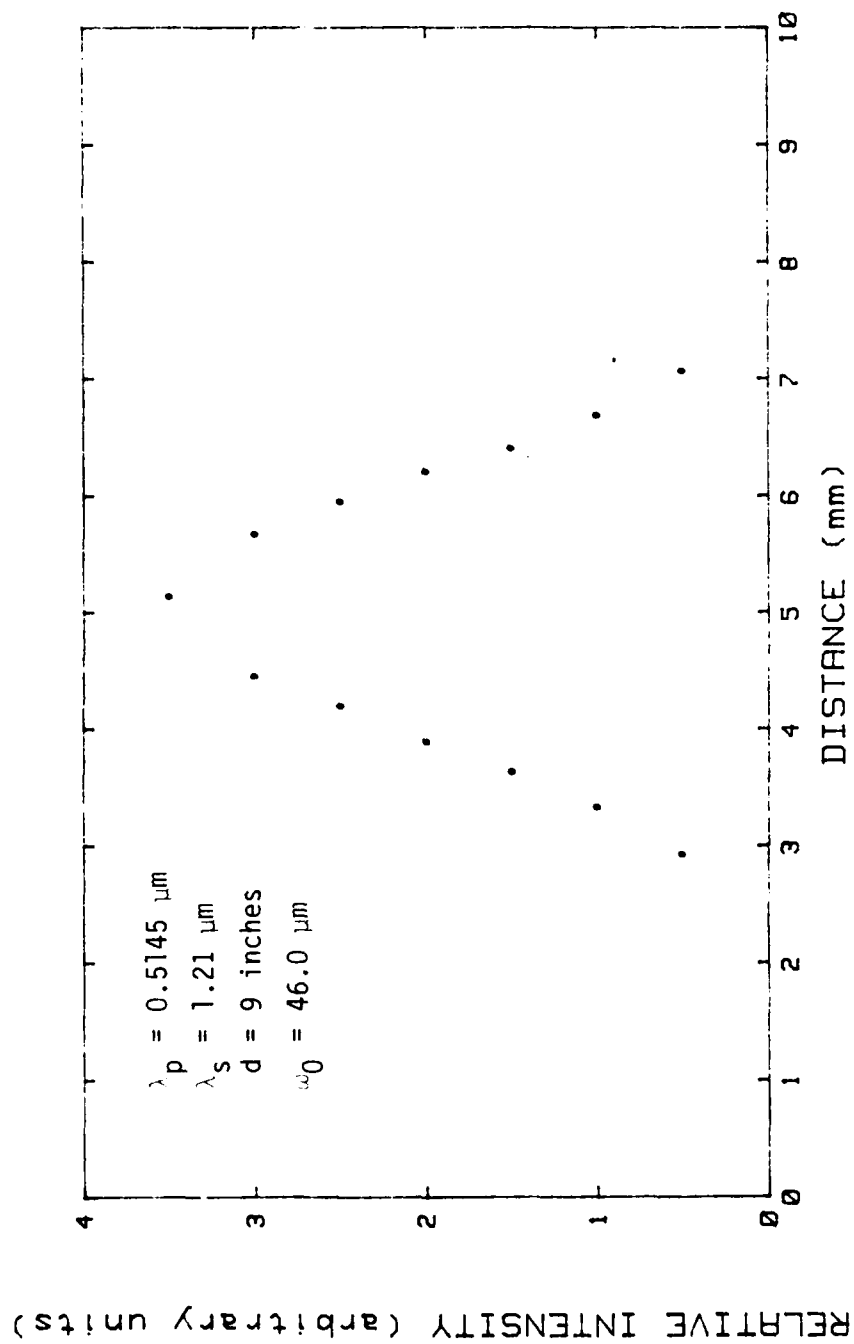


Figure 19 - Horizontal Mode Profile of 1.32  $\mu\text{m}$  Output from Fiber #17-1.

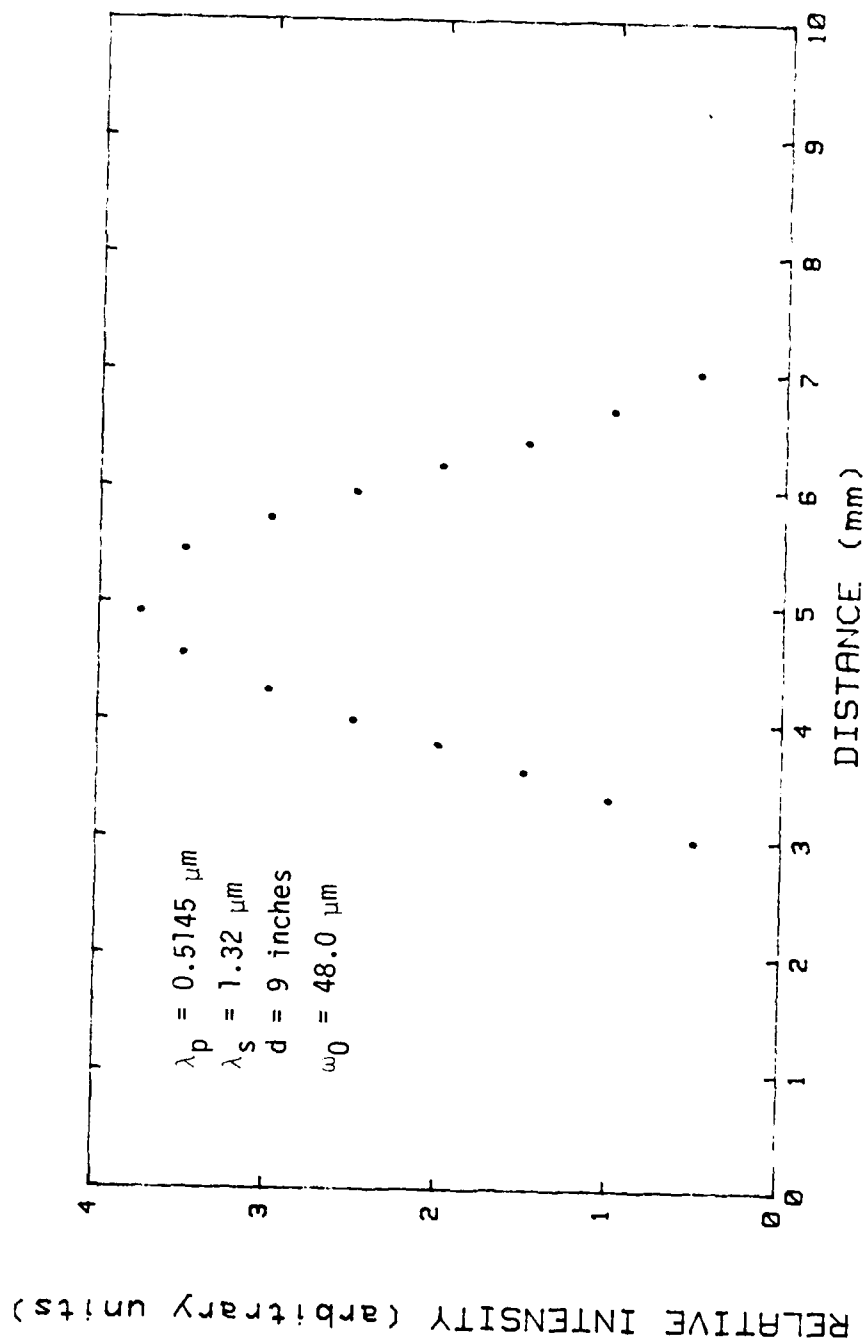


Figure 20 - Vertical Profile of 1.32  $\mu\text{m}$  Output from Fiber #17-1.

**Table 5.**  
**Fiber Laser Mode Waist Sizes**

Fiber #	$w_p(\mu m)$	$w_{0,hor}(\mu m)$	$w_{0,vert}(\mu m)$	$w_{0,ave}(\mu m)$	$A_p^*(cm^2)$
17-1	17.4	46.0	48.0	47.0	$3.945 \times 10^{-5}$
17-2	17.4	42.5	46.0	44.3	$3.558 \times 10^{-5}$
17-3	17.4	45.0	54.0	49.5	$4.324 \times 10^{-5}$
17-4	17.4	45.5	46.0	45.8	$3.771 \times 10^{-5}$
17-5	17.4	41.0	42.5	41.8	$3.220 \times 10^{-5}$
18-2	17.4	23.6	23.6	23.6	$1.350 \times 10^{-5}$
18-4	17.4	23.0	22.0	22.5	$1.271 \times 10^{-5}$

Signal mode profiles from the fibers of array #18 showed that the beam waist radius at the fiber output plane is about  $23 \mu m$  and very symmetrical about the fiber axis (see Table 5). This is in good agreement with the theoretical value of about  $26 \mu m$  expected for an  $80 \mu m$  diameter fiber. The average value of  $A_p^*$  is about  $1.311 \times 10^{-5} cm^2$ , almost a factor of 3 smaller than the average of  $A_p^* = 3.764 \times 10^{-5} cm^2$  for fiber array #17.

d. Loss Calculations

Total round-trip loss ( $T_1 = 1\%$ ) was found to be higher for the  $80 \mu m$  diameter fibers than for the  $170 \mu m$  fibers. Fiber #18-4 had the lowest loss factor  $\delta_1$  of approximately 0.22 while fiber #18-2 had a very high loss factor of about 0.63. The loss is actually given by  $1 - e^{-\delta_1}$  so that the actual losses were 20% for fiber #18-4 and 47% for fiber #18-2. The losses in these fibers may actually be somewhat lower due to an overestimation of the absorbed pump power. Because of residual defects on the fiber end-faces it is possible that some scattering of the pump beam may have occurred at the input end-face. Scattering losses due to the smaller diameter fibers could also have affected the estimate of amount of pump power absorbed by the fiber and thus the slope efficiency of the laser from which the loss is inferred. The Rayleigh range for the  $80 \mu m$  diameter fiber lasers was about  $z_R = 1.26 mm$ , which is smaller than the fiber length by a factor of 7. This shows that the signal was guided by the fiber in this case. The higher losses observed therefore resulted from scattering of the signal at the surface of the fiber. In contrast, the Rayleigh range for the  $170 \mu m$  fiber laser was about  $5 mm$  ( $w_0 = 46 \mu m$ ). Thus, an unguided Gaussian beam of this radius could have fit inside the fiber without being apertured (by the fiber) and therefore experienced lower loss.



**Table 6.**  
**Scattering Loss Coefficients**

Fiber #	$\alpha_s$ ( $cm^{-1}$ )
17-1	0.004
17-2	0.019
17-3	0.038
17-4	0.033
17-5	0.026
18-2	0.325
18-4	0.109

e. Comparison With 1.064  $\mu m$  Fiber Lasers

Estimates of the scattering loss coefficient  $\alpha_s$  of the fibers of arrays #17 and #18 have been inferred from the loss factor  $\delta_1$  obtained from the laser measurements. These values are listed in Table 6. They should be viewed as an upper bound on  $\alpha_s$ .

It is interesting to compare the results described here for 1.32  $\mu m$  fiber lasers to those obtained in an earlier phase of this contract for 1.064  $\mu m$  fiber lasers.<sup>9</sup> For guided devices (array #18) the lowest loss factor was  $\alpha_s = 0.109 \text{ cm}^{-1}$ , obtained for fiber #18-4. This can be compared to a loss coefficient of  $0.40 \text{ cm}^{-1}$  for an 80  $\mu m$  diameter fiber used in the 1.064  $\mu m$  laser experiments.<sup>9</sup> It should be stressed, however, that there is too little data in the guided case for a fair comparison. More data exists for unguided devices. For the latter case Table 7 lists loss coefficients for 7.8 mm long, 100  $\mu m$  diameter fibers used in the 1.064  $\mu m$  work<sup>9</sup> (array #1). This yields an average value of  $0.18 \text{ cm}^{-1}$  compared to an average of  $0.024 \text{ cm}^{-1}$  for array #17. It appears that the fibers used in the recent 1.32  $\mu m$  laser work exhibit a lower loss than fibers used previously to make 1.064  $\mu m$  lasers. The newer fibers were grown on the second generation growth station and had much better diameter control than the other fibers which were grown on the original fiber grower. This indicates the importance of the better diameter control obtained with the new growth station.

## V. DYE LASER PUMPING

### A. COHERENT DYE LASER SYSTEM

Because of its relatively high output power at 808 nm (compared to a laser diode) a

**Table 7.**  
**Scattering Loss For 1.064  $\mu m$  Fiber Lasers**

Fiber #	$\alpha_s$ ( $cm^{-1}$ )
1-1	0.022
1-2	0.094
1-3	0.144
1-4	0.017
1-6	0.030
1-7	0.641
1-8	0.052
1-9	0.364
1-10	0.074
1-11	0.324

dye laser was selected for initial characterization of 1.32  $\mu m$  fiber lasers pumped at this wavelength. The dye laser was a Coherent Model 599 Dye Laser System. The basic design was a three mirror, non-collinearly pumped, astigmatically compensated cavity. Pump light from a *cw* laser was focussed onto the dye stream by a pump mirror. The dye stream consisted of a high viscosity solvent (usually ethyleneglycol) with an organic dye solution at a concentration of  $10^{-4}$  to  $10^{-3}$  molar. Wavelength selection was accomplished with a birefringent tuning element which consists of three flat and parallel crystalline quartz plates placed inside the dye laser cavity at Brewster's angle (the plates form a birefringent filter which has low loss for linearly polarized light at a particular wavelength).

## B. EXPERIMENTAL ARRANGEMENT

Fiber #17-1 had the lowest threshold of all of the fibers in both arrays. It was therefore selected for tests using a *cw* dye laser tuned to a wavelength of 808 nm. Measurements showed that the pump beam transmission through the flat laser mirrors was about 85% for either mirror. The reflection coefficient of the coated Nd:YAG substrate at the pump wavelength was determined to be approximately 7.5%. The output from the dye laser was about 50 mW at  $\lambda = 808$  nm which was strong enough to be seen without any viewing device, as the laser beam appears red to the eye at this wavelength. This simplified matters somewhat but an *IR* viewer was still required to perform precise alignments.

Mirrors were used to direct the pump beam through the laser cavity and fiber #17-1.

Because the argon laser was used to pump the dye laser at  $\lambda_p = 0.5145 \mu m$  it was not possible to achieve laser oscillation first with the argon laser. Instead, the fiber and laser cavity were aligned as usual with the aid of an IR viewer. This proved to be quite easy. A fairly clean pump output spot was obtained from the fiber although some diffraction rings were observed. The amount of pump power coupled into the fiber was estimated to be about 20 mW. Virtually all of this was absorbed because of the strong absorption coefficient of Nd:YAG at 808 nm, believed to be about  $4 cm^{-1}$ . A measurement of the transmission of the pump beam through fiber #17-1 indicated that the absorption coefficient was actually about  $5.6 cm^{-1}$ . This estimate is probably high due to scattering of the pump beam by the fiber but it is of no consequence since almost all of the pump beam is absorbed for such large absorption coefficients. From previous work at 0.5145  $\mu m$  the absorbed pump power at threshold for the new pump wavelength was expected to be about 8 mW. This estimate was made by using the best threshold obtained at 0.5145  $\mu m$  (12.0 mW) and scaling the pump wavelength (the threshold varies as the inverse of the pump wavelength, Equation (11)).

### C. DISCUSSION

Repeated attempts to obtain laser oscillation in fiber #17-1 were unsuccessful. It is believed that the pump power level was not sufficient to allow an easy alignment of the fiber laser cavity. In past experience with fiber lasers pumped at  $\lambda_p = 0.5145 \mu m$ , low thresholds were obtained only after further cavity alignment performed once laser action had been obtained at a higher pump power level. The output power from the dye laser could probably be increased to about 100 mW by servicing the argon laser. Unfortunately, no time was left under the current contract to perform the necessary adjustments and continue the testing.

## PART C - THEORETICAL ANALYSIS AND DESIGN OF Q-SWITCHED FIBER LASERS

### I. MODAL OVERLAP THEORY OF Q-SWITCHED LASERS

#### A. GENERAL THEORY

Implementation of a Q-switching scheme in a fiber laser should be preceded by an

investigation of the effects of the spatial overlap between the signal mode in the cavity and the profile of the population inversion in the gain medium. A very broad theory is presented here which is applicable to unguided as well as waveguide lasers. Since the width of the  $Q$ -switched pulse is on the order of nanoseconds the effects of optical pumping and the relaxation of the population inversion are neglected during the emission of the output pulse. The switching time between high and low values of the cavity loss is taken to be negligible. Assuming some general spatial distribution for the population inversion  $n(x, y, z)$  the cavity equations of motion may be written as<sup>9,15,20</sup>

$$\frac{dn(x, y, z)}{dt} = -\frac{c\sigma}{n_l} \sum_{j=1}^m s_j(x, y, z) n(x, y, z) \quad (33)$$

$$\frac{dS_i}{dt} = \frac{c\sigma}{n_l} \int \int \int_{\text{active medium}} n(x, y, z) s_i(x, y, z) dv - \frac{c\delta_i}{2ln_l} S_i \quad (34)$$

where  $c$  is the velocity of light in free space,  $\sigma$  is the gain cross-section for stimulated emission,  $n_l$  is the index of refraction of the laser medium and  $l$  is the optical cavity length. Here  $s_i(x, y, z)$  is the photon distribution function for the  $i^{\text{th}}$  signal mode and  $\delta_i$  is the total round-trip loss for the  $i^{\text{th}}$  mode. The total number of photons in the cavity for the  $i^{\text{th}}$  mode  $S_i$  is found by integrating  $s_i(x, y, z)$  over the volume of the resonator.

At this point it is convenient to introduce the normalized spatial distribution functions  $n_0(x, y, z)$  and  $s_{0,i}(x, y, z)$  for the population inversion and the signal mode, respectively. They are defined by

$$n(x, y, z) = n n_0(x, y, z) \quad (35)$$

$$s_i(x, y, z) = S_i s_{0,i}(x, y, z) \quad (36)$$

where

$$\int \int \int_{\text{cavity}} s_{0,i}(x, y, z) dv = \int \int \int_{\text{active medium}} n_0(x, y, z) dv = 1 \quad (37)$$

Substituting Equation (35) into Equation (33) and then integrating over the active volume of the cavity yields

$$\frac{dn}{dt} = -\frac{c\sigma n}{n_l} \int \int \int_{\text{active medium}} \sum_{j=1}^m s_j(x, y, z) n_0(x, y, z) dv \quad (38)$$

Interchanging summation and integration in Equation (38) results in

$$\frac{dn}{dt} = -\frac{c\sigma}{n_l} n \sum_{j=1}^m \iiint_{\text{active medium}} s_j(x, y, z) n_0(x, y, z) dv \quad (39)$$

A parameter  $F_j$  is now defined which takes into account the spatial overlap between the  $j^{\text{th}}$  cavity mode and the profile of the population inversion in the laser medium. It is given by

$$F_j \equiv \iiint_{\text{active medium}} s_{0,j}(x, y, z) n_0(x, y, z) dv \quad (40)$$

The overlap integral  $F_i$  described in this work may be related to a filling factor  $F_{\nu_s \mu_s \nu_p \mu_p}$  as defined earlier (see Section II-B in Part B)

$$F_i = \frac{F_{\nu_s \mu_s \nu_p \mu_p}}{lA_f} \quad (41)$$

where  $A_f$  is the cross-sectional area of the active region of the fiber.

Equations (34) and (39) then become:

$$\frac{dS_i}{dt} = \frac{c\sigma}{n_l} n F_i S_i - \frac{c\delta_i}{2ln_l} S_i \quad (42)$$

$$\frac{dn}{dt} = -\frac{c\sigma}{n_l} n \sum_{j=1}^m F_j S_j \quad (43)$$

Next Equation (42) is divided by Equation (43) to eliminate explicit time dependence. This leads to

$$\frac{dS_i}{dn} = \frac{\delta_i}{2l\sigma} \frac{1}{\sum_{j=1}^m F_j S_j} \frac{S_i}{n} - \frac{F_i}{\sum_{j=1}^m F_j S_j} S_i \quad (44)$$

The population inversion at threshold  $n_{t,i}$  for the  $i^{\text{th}}$  transverse mode is defined as the inversion required to reach threshold in the  $cw$  case with the cavity loss equal to the high- $Q$  value of  $\delta_i$ :

$$n_{t,i} = \frac{n_0}{F_i} \quad (45)$$

where  $n_0$  is the threshold inversion for the plane wave case given by<sup>17,21</sup>

$$n_0 = \frac{\delta_i}{2l\sigma} \quad (46)$$

Equation (44) may now be rewritten in a much more simple and understandable form with the aid of Equation (45):

$$\frac{dS_i}{dn} = \frac{F_i S_i}{\sum_{j=1}^m F_j S_j} \left( \frac{n_{t,i}}{n} - 1 \right) \quad (47)$$

For the case of a single mode oscillating, Equation (47) reduces to

$$\frac{dS_i}{dn} = \left( \frac{n_{t,i}}{n} - 1 \right) \quad (48)$$

This last result is identical to that which would be obtained in a standard analysis of  $Q$ -switching involving an interaction of plane waves.<sup>21</sup> The spatial overlap between the signal mode and the profile of the population inversion in the laser material merely affects the value of the threshold inversion for the case of a single mode. The solution of the more general Equation (47) is:

$$S_i - S_{i,in} + \frac{1}{F_i} \sum_{\substack{j=1 \\ j \neq i}}^m F_j \int_{S_{i,in}}^{S_i} \frac{S_j}{S_i} dS_i = \left[ n_{t,i} \ln \frac{n}{n_{in}} - (n - n_{in}) \right] \quad (49)$$

The initial number of photons in the cavity for the  $i^{th}$  transverse mode is given by  $S_{i,in}$  while  $n_{in}$  represents the initial population inversion at the beginning of the  $Q$ -switched output pulse. Assuming  $S_{i,in}$  is negligible (compared to  $S_i$ ) allows one to write Equation (49) as

$$S_i + \sum_{\substack{j=1 \\ j \neq i}}^m \frac{F_j}{F_i} \int_0^{S_i} \frac{S_j}{S_i} dS_i = \left[ n_{t,i} \ln \frac{n}{n_{in}} - (n - n_{in}) \right] \quad (50)$$

Equations (50) actually comprise a system of equations for  $i = 1, 2, \dots, m$  which must be solved simultaneously. This can be done using numerical methods. The solutions to Equation (50) give the relationship between the number of photons in a given transverse mode  $S_i$  and the inversion  $n$  at any moment in time.

## B. SINGLE MODE CASE

### 1. Output Power

With only a single spatial mode present ( $S_j = 0$  for  $j \neq i$ ) Equation (50) reduces to

$$S_i = \left[ n_{t,i} \ln \frac{n}{n_{in}} - (n - n_{in}) \right] \quad (51)$$

At the end of the  $Q$ -switched pulse the photon density is once again zero. The final inversion  $n_f$  can be found by setting  $S_i = 0$  in Equation (51) which results in

$$\frac{n_f}{n_{in}} = \exp \left( \frac{n_f - n_{in}}{n_{t,i}} \right) \quad (52)$$

Equation (52) may also be obtained by setting  $S_i = 0$  in the more general expression of Equation (50). Equation (52) can be solved graphically or numerically for  $\frac{n_f}{n_{in}}$  as a function of  $\frac{n_{in}}{n_{t,i}}$ . This is done in Figure 21 where it should be noted that the threshold inversion is a function of the spatial overlap parameter  $F_i$ . The fraction of energy originally stored in the inversion is  $\frac{n_{in} - n_f}{n_{in}}$ , the so-called energy utilization factor. As  $n_{in}$  increases to values much higher than  $n_t$ , the final population inversion  $n_f$  is driven down to virtually zero and the energy utilization factor increases to near unity value.

The instantaneous output power is found from<sup>21</sup>

$$P_i = S_i h \nu_s \left( \frac{c T_1}{2 l n_l} \right) \quad (53)$$

where  $T_1$  is the output coupler transmittance. For the case of a single transverse mode laser the equation governing the dependence of the output power on the population inversion is found using Equations (51) and (53):

$$P_i = h \nu_s \left( \frac{c T_1}{2 l n_l} \right) \left[ n_{t,i} \ln \frac{n}{n_{in}} - (n - n_{in}) \right] \quad (54)$$

## 2. Maximum Output Power

The maximum output power is found by setting  $\frac{dP_i}{dn} = 0$  in Equation (54). This shows that the maximum output is obtained when  $n = n_{t,i}$ . Using this result in Equation (54) gives the following expression for the maximum output power:

$$P_{i,max} = h \nu_s \left( \frac{c T_1}{2 l n_l} \right) \left[ n_{t,i} \ln \frac{n_{t,i}}{n_{in}} - (n_{t,i} - n_{in}) \right] \quad (55)$$

It has been possible to put all of the results for the single mode case into forms equivalent to those obtained in a plane wave analysis.<sup>21</sup> The only difference is that the threshold inversion  $n_t$  is now replaced by  $\frac{n_t}{F}$  where  $F$  is the overlap between the profile of

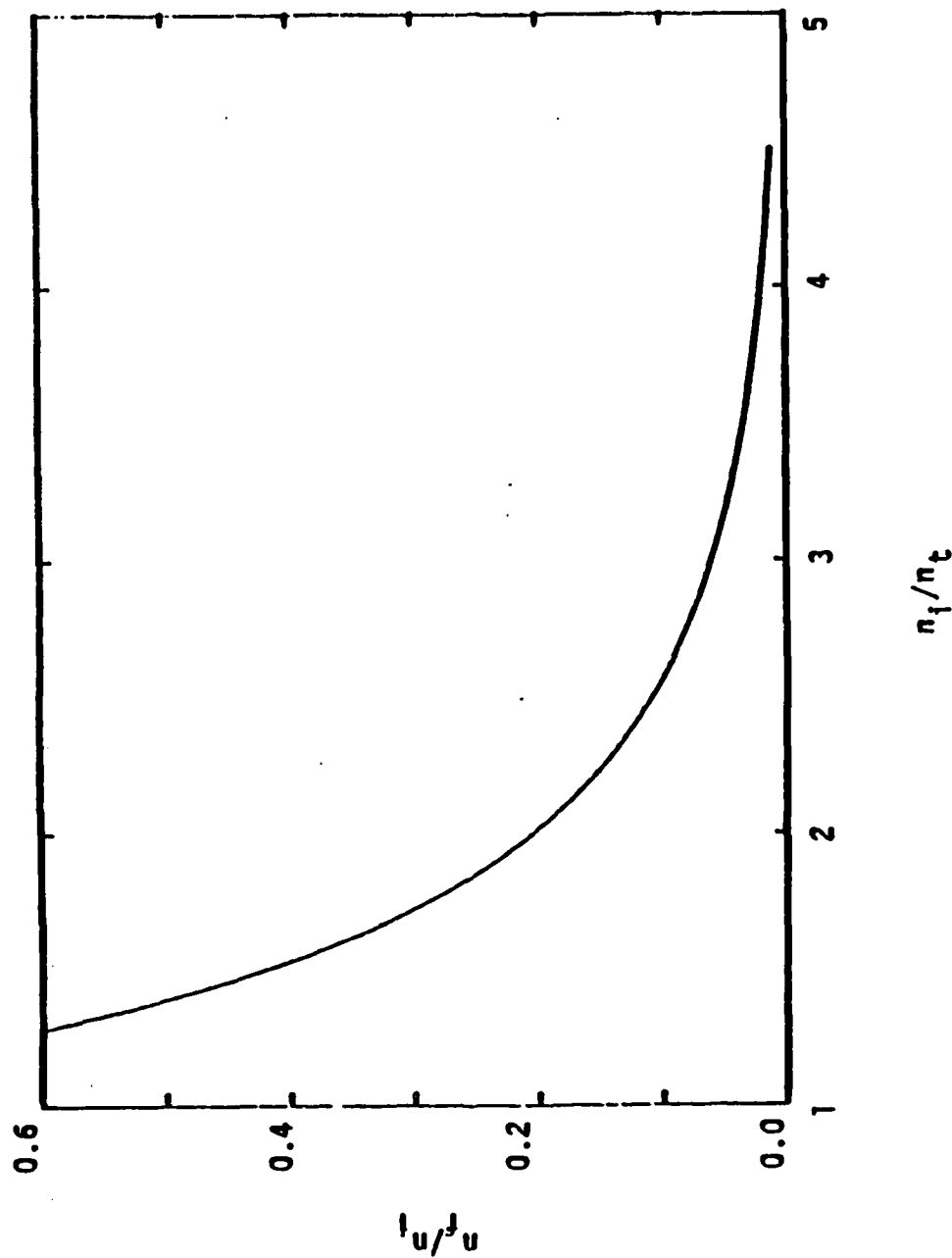


Figure 21 - Fraction of the Initial Inversion remaining after the Q-switch Pulse versus the Ratio of the Initial Inversion at the Beginning of the Pulse to the Threshold Inversion.



the population inversion and the signal mode. Also, note that, in general, the total cavity loss is different for each transverse mode.

### 3. Pulse Energy

The total energy in the output pulse may be obtained by integrating the instantaneous power  $P_i$  over time from the beginning to the end of the pulse.

$$E_i = \int_{t_i}^{t_f} P_i dt = \int_{n_i}^{n_f} \frac{P_i}{\frac{dn}{dt}} dn \quad (56)$$

where  $\frac{dn}{dt}$  is given by Equation (43) for the single mode case expressed in terms of output power instead of photon number:

$$\frac{dn}{dt} = -\left(\frac{2l\sigma}{T_1}\right)\left(\frac{F_i}{h\nu_s}\right)nP_i \quad (57)$$

Substituting Equation (57) into Equation (56) and performing the integration over  $n$  results in the following expression for the output pulse energy:

$$E_i = \left(\frac{T_1}{2l\sigma}\right)\left(\frac{h\nu_s}{F_i}\right)\ln\left(\frac{n_{in}}{n_f}\right) \quad (58)$$

Equation (58) may be rewritten in a form that is more convenient for physical interpretation with the aid of Equations (45), (46), and (52):

$$E_i = \frac{T_1}{\delta_i} h\nu_s (n_{in} - n_f) \quad (59)$$

The energy in the output pulse is proportional to the difference between the initial and final population inversions, the photon energy at the signal wavelength, and the ratio of the transmittance of the output coupler to the total round-trip loss.

### 4. Pulse Width

Assuming a triangular approximation to model the pulse shape, the pulse width  $\Delta t_i$  may now be defined as<sup>17,21</sup>

$$\Delta t_i \equiv \frac{2E_i}{P_{i,max}} \quad (60)$$

Using Equations (55) and (59) allows Equation (60) to be written as

$$\Delta t_i = \left( \frac{4 \ln l}{c \delta_i} \right) \frac{n_{in} - n_f}{n_{t,i} \ln \left( \frac{n_{t,i}}{n_{in}} \right) - (n_{t,i} - n_{in})} \quad (61)$$

or, in terms of the photon lifetime  $\tau_c = 2 \ln l / c \delta_i$  in the cavity

$$\Delta t_i = 2 \tau_c \frac{n_{in} - n_f}{n_{t,i} \ln \left( \frac{n_{t,i}}{n_{in}} \right) - (n_{t,i} - n_{in})} \quad (62)$$

The pulse width is found to be a complicated function of the overlap between the spatial distributions of the population inversion and the laser signal through the threshold inversion. It is also a function of the initial and final population inversions. Varying the device, signal, and pump beam parameters will thus affect the width of the output pulse.

### 5. Initial Population Inversion

The initial population inversion,  $n_{in}$ , at the beginning of the output pulse may be related to the pump power by use of the laser rate equations referenced from Section III of Part A of this report. During the off state when optical pumping is populating the upper laser level the cavity loss is high and laser oscillation is suppressed. This means that the photon number,  $S_i$ , and the rate of change of the photon number are equal to zero. The rate equations then yield the following expression relating the population inversion and the pumping rate during the off state

$$\frac{dn(x, y, z, t)}{dt} = r(x, y, z) - \frac{n(x, y, z, t)}{\tau_f} \quad (63)$$

where  $r(x, y, z)$  is the spatial distribution of the pump beam. Normalized distribution functions for the population inversion and the pump field may be defined as

$$n(x, y, z, t) \equiv n(t) n_0(x, y, z) \quad (64)$$

$$r(x, y, z) \equiv R r_0(x, y, z) \quad (65)$$

where

$$\int \int \int_{cavity} n_0(x, y, z) dv = \int \int \int_{cavity} r_0(x, y, z) dv = 1 \quad (66)$$

Here it is assumed that the profile of the population inversion follows the mode profile of the pump mode so that  $n_0(x, y, z)$  and  $r_0(x, y, z)$  have identical distributions.

Substituting Equations (64) - (66) into Equation (63) and integrating over the cavity yields

$$\frac{dn(t)}{dt} = R - \frac{n(t)}{\tau_f} \quad (67)$$

The solution of this equation, expressed in terms of absorbed pump power rather than photon pumping rate, is

$$n_{in} = n(t_2) = n(t_1) \exp\left(-\frac{\Delta t_p}{\tau_f}\right) + \left(\frac{\tau_f}{h\nu_p}\right) \left[1 - \exp\left(-\frac{\Delta t_p}{\tau_f}\right)\right] P_{abs} \quad (68)$$

where  $\Delta t_p = t_2 - t_1$  is the time interval during the off state when optical pumping is occurring,  $n(t_1)$  is the population inversion at time  $t_1$  when pumping is initiated,  $n(t_2)$  is the population inversion at time  $t_2$  which corresponds to the onset of laser action, and  $R = \frac{P_{abs}}{h\nu_p}$ .

For  $\Delta t_p \gg \tau_f$  ( $\tau_f$  is approximately 236  $\mu s$  for Nd:YAG), Equation (68) reduces to

$$n_{in} = \left(\frac{\tau_f}{h\nu_p}\right) P_{abs} \quad (69)$$

In cases where the active medium does not extend over the entire waveguide (as for a step index fiber with an active core and a passive cladding) the absorbed pump power depends upon fiber and pump beam parameters. Then it is better to express the initial population inversion in terms of the pump power  $P_{inc}$  coupled into the fiber at the input. Equation (69) then becomes

$$n_{in} = \frac{\tau_f}{h\nu_p} [1 - \exp(-\alpha'_p l)] P_{inc} \quad (70)$$

where  $\alpha'_p$  is the effective pump absorption coefficient which is simply the plane wave absorption coefficient multiplied by the fraction of the pump power contained within the active region of the waveguide.

## C. Q-SWITCHED FIBER LASERS

### 1. Fiber Laser Configuration

The theory derived above will now be applied to a fiber waveguide laser. A step index profile is assumed for the fiber laser, with the active (laser) material comprising the fiber core while the cladding is passive. Thus only the interactions of the laser signal

modes in the core region of the fiber are important for modal overlap calculations with the spatial profile of the population inversion (pump beam modes). A standard weakly guiding approximation is made for the fiber so that the  $LP_{\nu,\mu}$  modes described in Section III of Part A are used to represent the pump and signal distributions. All numerical examples treat the case of a fiber core made of Nd:YAG, with indices of refraction of about 1.819 at the signal wavelength ( $1.064\ \mu\text{m}$ ) and 1.845 at the pump wavelength ( $0.5145\ \mu\text{m}$ ).  $LP_{01}$  mode profiles are assumed for both the signal and the pump modes. The fluorescence lifetime of Nd:YAG is  $236\ \mu\text{s}$  while the gain cross-section at  $1.064\ \mu\text{m}$  is approximately  $3.2 \times 10^{-19}\ \text{cm}^2$ .

## 2. Behavior of Population Inversions

Plots of the variation of the initial, final, and threshold population inversions are shown in Figures 22 and 23 for pump wavelengths of  $0.5145\ \mu\text{m}$  and  $808\ \text{nm}$ , respectively. Laser action is possible only when the initial population inversion is greater than that required for threshold. This occurs for a broad but limited range of the core radius, as observed in Figures 22 and 23. A larger difference between the initial and threshold inversions results in a smaller value of the final inversion and thus more energy in the output pulse, which is proportional to the difference between the initial and final inversions. Minimum pulse width also occurs within a more limited part of this region resulting in a narrower range of optimum core radius for maximum peak output power in contrast to a broader region of maximum pulse energy.

## 3. Maximum Output Power

A plot of peak output power as a function of core radius is shown in Figure 24. The parameter used in the family of curves is the index difference between the core and cladding regions which is assumed to be the same for both the pump and signal wavelengths. The pump power coupled into the fiber is  $60\ \text{mW}$  and the output coupler transmission is taken to be 1% while the total round-trip cavity loss is 5% for the high- $Q$  state. The fiber length is  $8\ \text{mm}$  with an absorption coefficient of  $0.6\ \text{cm}^{-1}$  at the pump wavelength.

The values of the index difference used for the three curves are 0.001, 0.005, and 0.010. All of the curves approach zero as the core radius is decreased for core radii near zero. This corresponds to the fact that as the core volume shrinks toward zero the pump and signal fields extend into the passive cladding where there is no interaction between them. As the core radius is increased the effective gain (which is intensity dependent) is decreased;

# POPULATION INVERSION VS CORE RADIUS

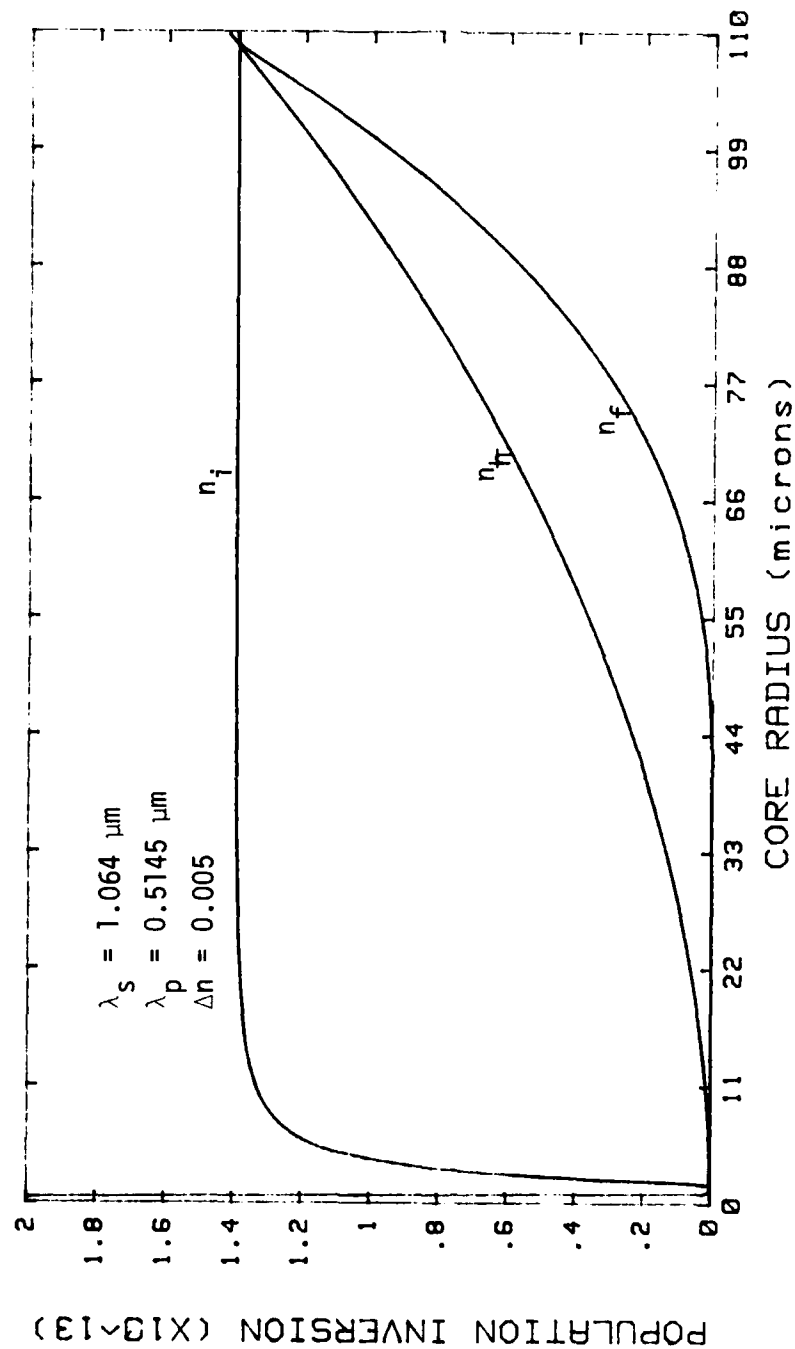


Figure 22 - Behavior of Population Inversions as a Function of the Fiber Core Radius.

# POPULATION INVERSION vs CORE RADIUS

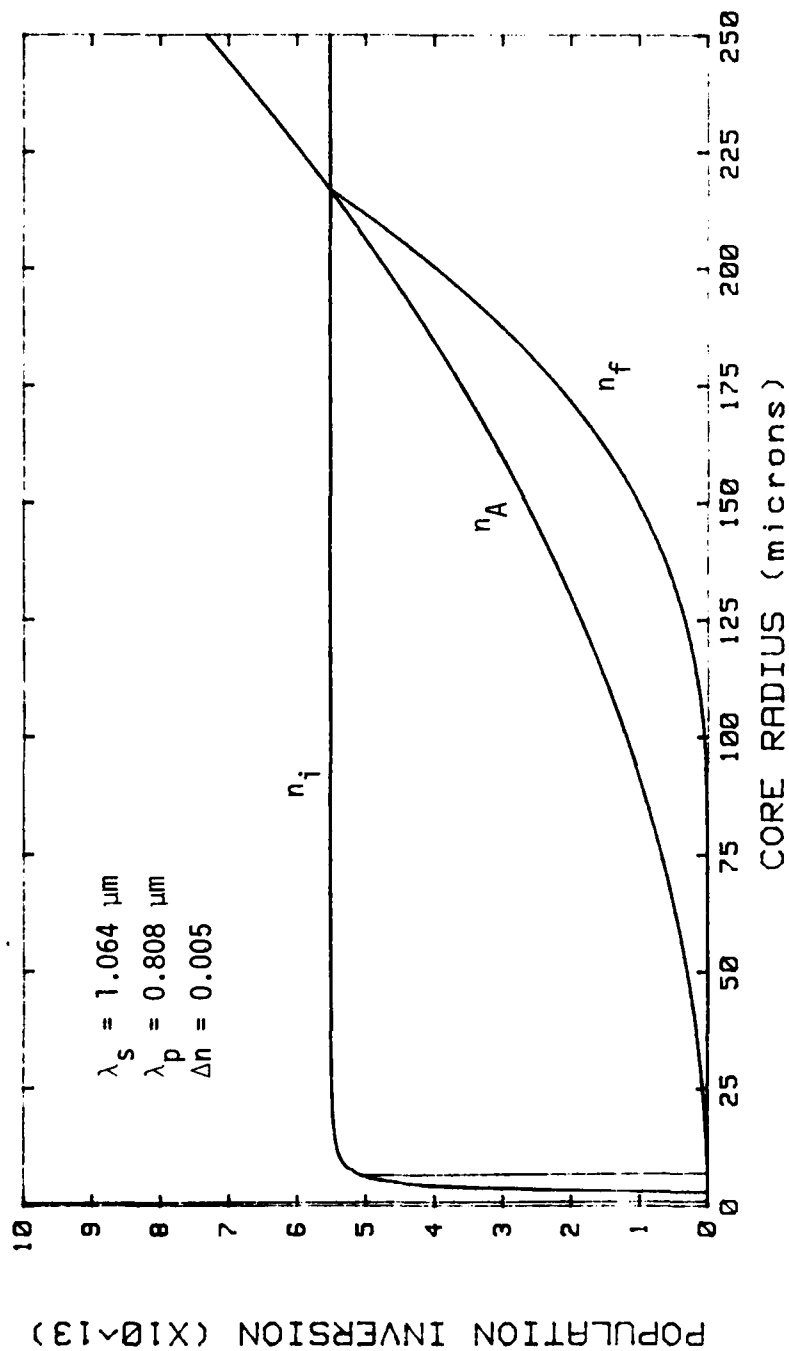


Figure 23 - Population Inversion versus Fiber Core Radius.

# MAXIMUM OUTPUT POWER vs CORE RADIUS

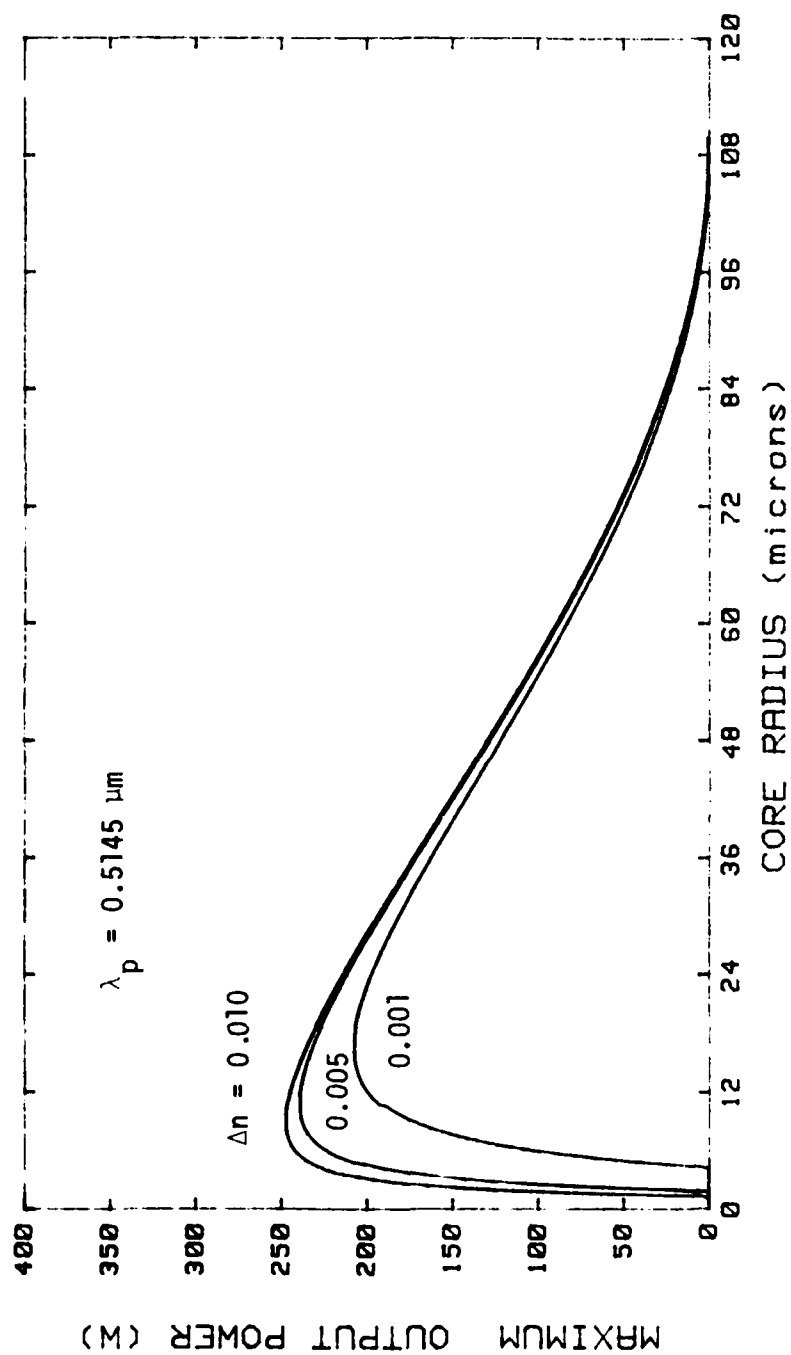


Figure 24 - Peak Output Power as a Function of the Fiber Core Radius.

when the initial inversion no longer exceeds the threshold inversion, no laser oscillation can occur. Thus, an optimum core radius exists which maximizes the peak power in the output pulse.

This behavior is indeed observed in Figure 24. For an index difference of 0.005 between the core and the cladding the optimum value of the core radius is about  $11\ \mu\text{m}$ . Increasing the index difference results in a slightly higher peak power since more of the pump and signal fields reside in the core region. Also, increasing the index difference shifts the optimum value of the core radius toward shorter core radii (the peak power occurs near optimum energy density, which itself is a function of the fiber  $V$  number, not of the core radius alone). In this particular configuration, and with a proper choice of fiber parameters, peak powers in excess of  $200\ \text{W}$  can be generated with a pump power level of only  $60\ \text{mW}$ . Note that the fiber diameter which optimizes the peak output power for this case is in the range of  $5\text{--}20\ \mu\text{m}$ , which is similar to the requirement for optimum operation of a *cw* laser of the same material.

A plot of the peak power obtained for a pump wavelength of  $808\ \text{nm}$  is presented in Figure 25. For direct comparison with argon laser pumping the same input power is assumed ( $60\ \text{mW}$ ). The curves are also plotted for three different values of the core/cladding index difference, as done previously. The same general behavior is observed. The peak output power is now on the order of  $1\ \text{kW}$  compared to  $240\ \text{W}$  for argon laser pumping. This improvement is due largely to the much larger absorption coefficient at  $\lambda_p = 808\ \text{nm}$  ( $4\ \text{cm}^{-1}$ ). Scaling the input pump power to that typically available from single transverse mode laser diodes ( $15\ \text{mW}$ ) results in a peak output power around  $125\ \text{W}$ . The maximum permissible core radius extends out to past  $200\ \mu\text{m}$  compared to just past  $100\ \mu\text{m}$  for argon laser pumping because of the higher gain per unit pump intensity achievable with  $808\ \text{nm}$  pumping.

#### 4. Output Pulse Energy

Pulse energy versus core radius is plotted in Figure 26 for an index difference of 0.005 between the core and the cladding. For small values of the core radius the energy in the output pulse increases with increasing core radius and quickly levels off at about  $0.52\ \mu\text{J}$  in the range of  $10\text{--}60\ \mu\text{m}$ . This is because the energy depends upon the difference between the initial and final population inversions. The initial inversion rapidly approaches a constant (maximum) value as explained previously so that the pulse energy stays fairly constant for a limited but wide range of core radius. At larger core values the threshold inversion begins to increase quadratically, causing the final inversion to increase until it reaches the



# MAXIMUM OUTPUT POWER vs CORE RADIUS

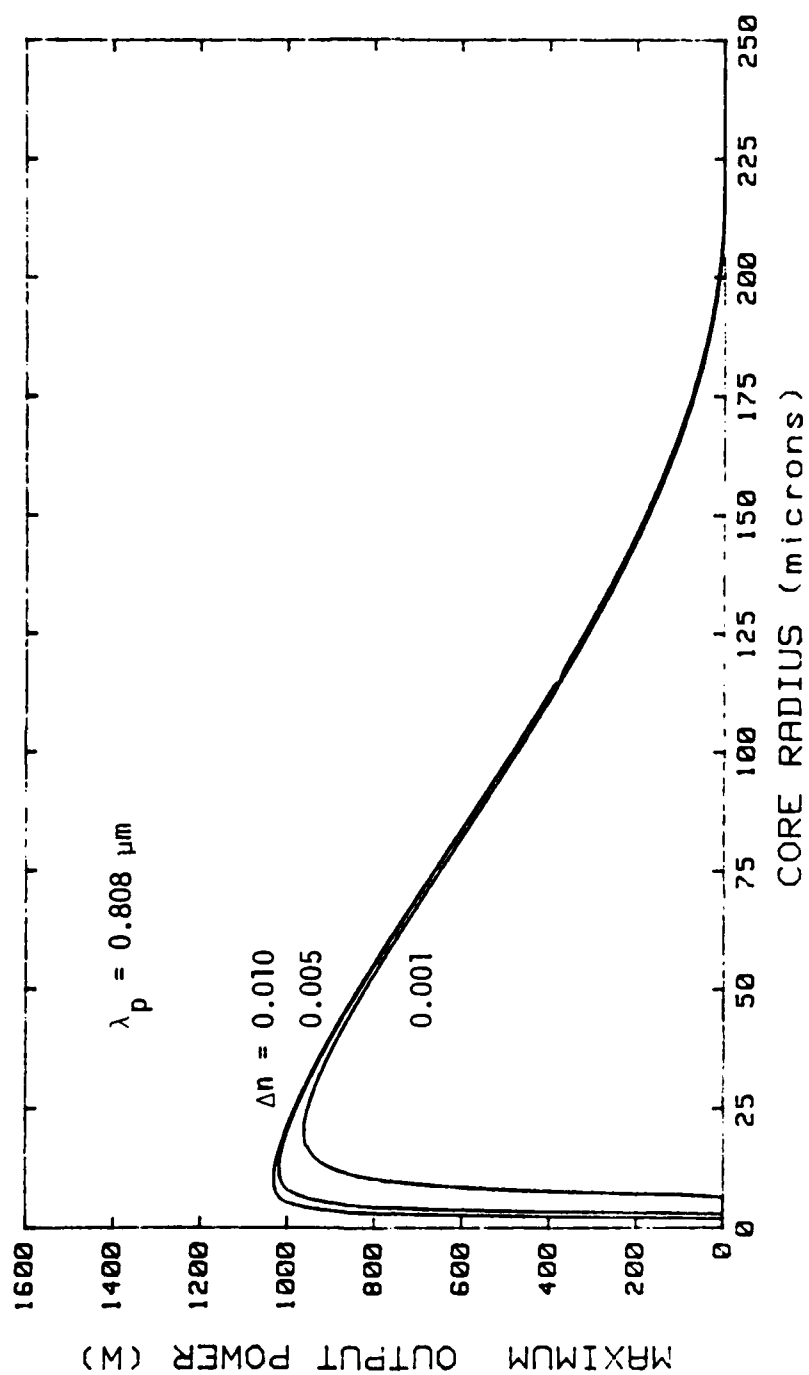


Figure 25 - Plot of Peak Output Power versus Fiber Core Radius.

# PULSE ENERGY vs CORE RADIUS

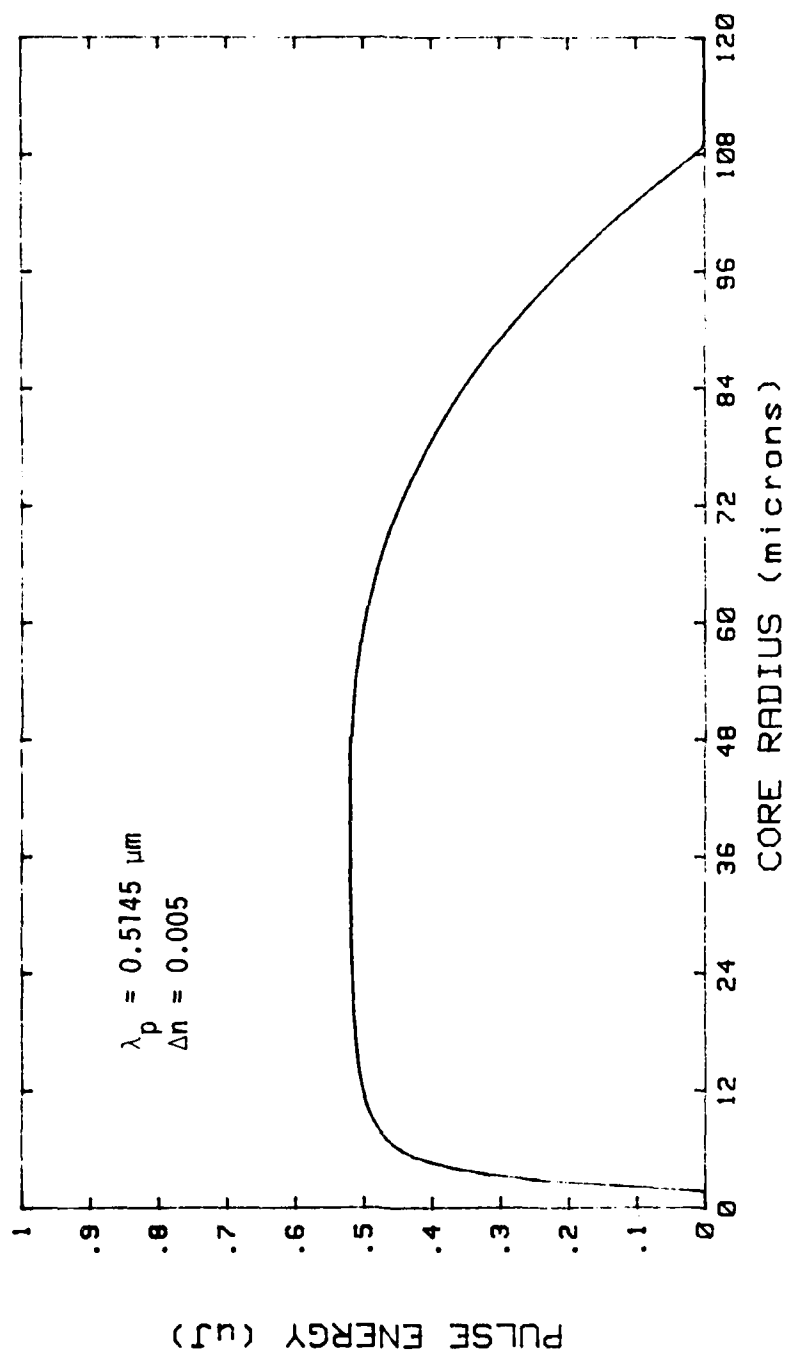


Figure 26 - A Plot of Pulse Energy versus Core Radius.

value of the initial inversion. At this point the initial, final, and threshold inversions are all equal and no laser oscillation can occur. Note that the region where the peak pulse energy occurs is much broader than the range of maximum peak output power. This is caused by an increase in the width of the output pulse, described below.

Much larger pulse energies are obtained for  $\lambda_p = 808 \text{ nm}$ , as shown in Figure 27 for the same input power and a core/cladding index difference of 0.005. The maximum energy is on the order of  $2 \mu J$  compared to about  $0.5 \mu J$  for  $\lambda_p = 0.5145 \mu m$ .

## 5. Pulse Width

The pulse width, plotted in Figure 28 as a function of core radius, is seen to increase monotonically, and nearly quadratically, over most of the practical operating range. The pulse width is a relatively weak function of the fiber size as it varies from 4 to  $8.5 \text{ nsec}$  for values of the core radius in the range of  $2\text{-}50 \mu m$ . Near the optimum range of operation ( $2\text{-}20 \mu m$  for an index difference of 0.005), it is close to its minimum value ( $4 \text{ nsec}$ ). As the core radius is further decreased from about  $2 \mu m$  the pulse width goes to infinity.

## 6. Summary

In this section a general theory of the effects of modal overlap in  $Q$ -switched optically pumped lasers has been developed. When applied to the case of a fiber laser it was shown that there is an optimum range of operation of the laser in terms of fiber  $V$  number (or core size for a given N.A.), which maximizes the peak output power. This range is  $V = 4\text{-}16$  (or  $a = 5\text{-}20 \mu m$  for  $\Delta n = 0.005$ ) which is similar to the range of optimum  $cw$  operation. Changing the index difference between the core and cladding regions has only a slight effect upon the peak power but shifts the optimum range of the core radius a modest amount. A given set of device and pump beam parameters affects the width of the operating range (with respect to core radius). For argon pumping at  $\lambda_p = 0.5145 \mu m$  the peak output power drops to zero at a core radius just under  $110 \mu m$  for an input power of  $60 \text{ mW}$  coupled into the fiber. A pump wavelength of  $808 \text{ nm}$  extends this region out to about  $220 \mu m$  for the same input pump power primarily because of the larger absorption coefficient at this wavelength. Anticipated peak powers are on the order of  $100\text{-}1000 \text{ W}$ .

The pulse energy is nearly independent of the fiber  $V$  number over most of the lasing range while the pulse width increases monotonically over the core range of interest. A typical value of the pulse width is  $4\text{-}8 \text{ nsec}$  for a practical Nd:YAG fiber laser.

Pumping with a laser diode is found to be superior to argon laser pumping in principle

# PULSE ENERGY vs CORE RADIUS

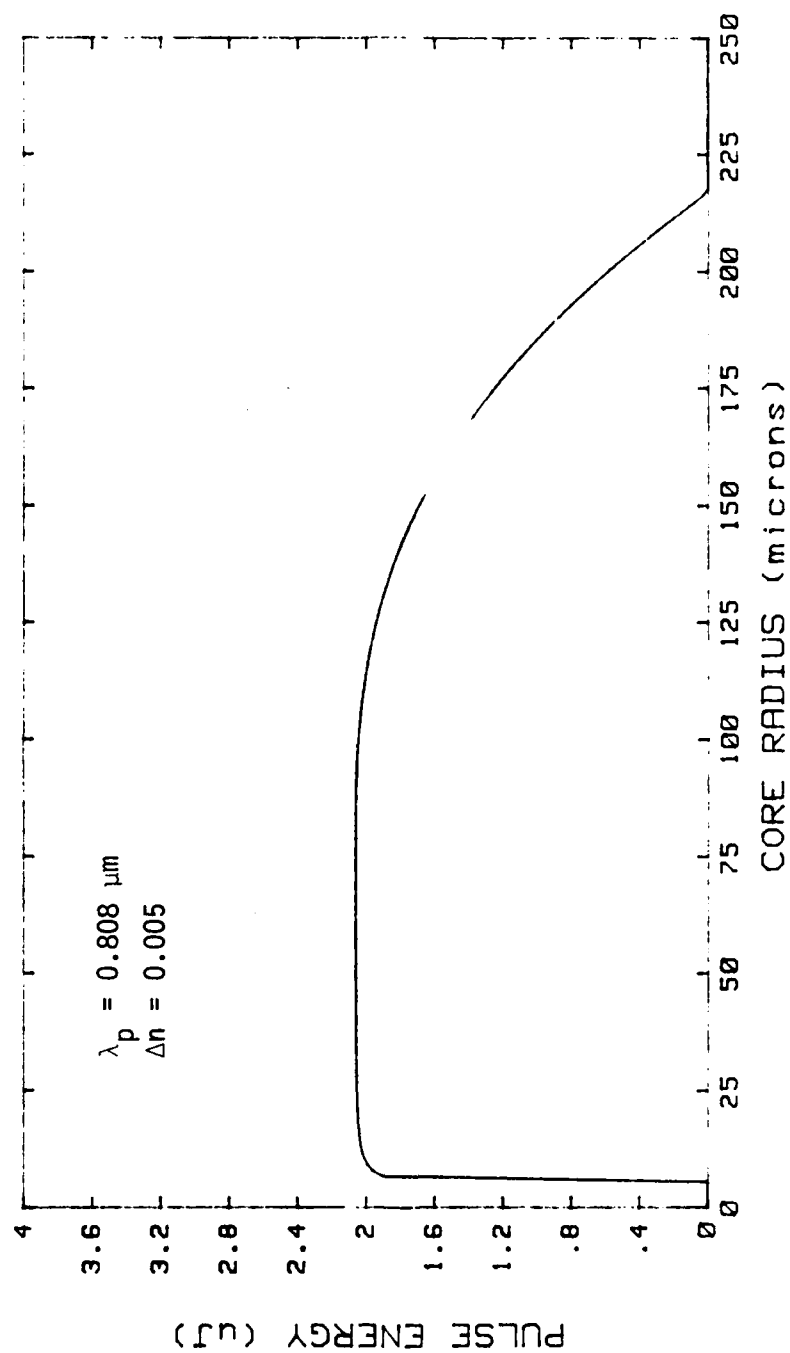


Figure 27 - Pulse Energy as a Function of the Fiber Core Radius.

# PULSE WIDTH vs CORE RADIUS

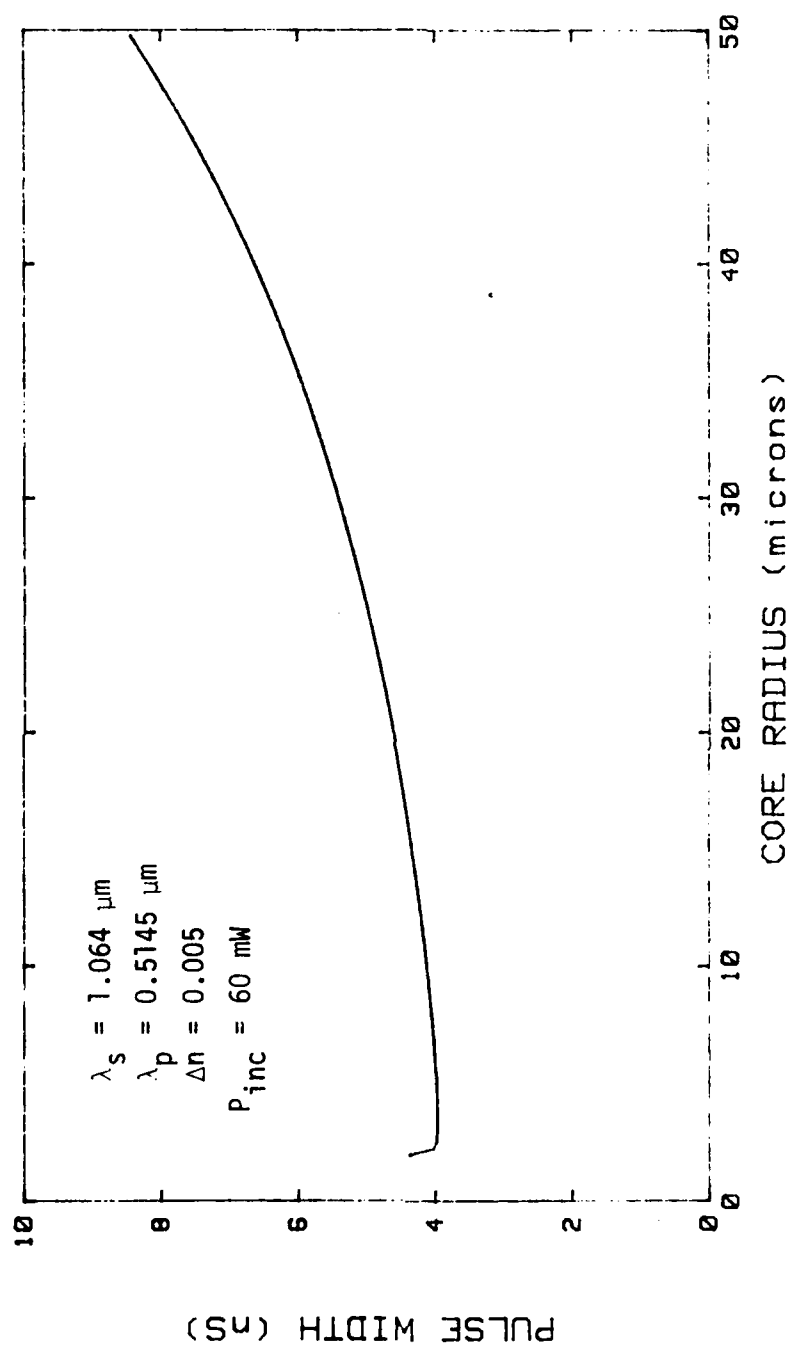


Figure 28 - Pulse Width versus Core Radius.

because it has a lower threshold and higher fractional absorbed power.

The effects of modal overlap in  $Q$ -switched fiber lasers is clearly understood and analytically characterized in terms of tabulated overlap coefficients. Although only the case of an end-pumped step-index fiber laser with an active core region has been extensively studied, this theory can easily be applied to other configurations. This includes unguided lasers as well as waveguide lasers.

## II. EVALUATION OF FIBER LASER $Q$ -SWITCHING SCHEMES

### A. SWITCHING METHODS

#### 1. Introduction

Now that the effects of fiber, pump, and signal parameters on  $Q$ -switched fiber laser performance have been studied, attention is directed toward an evaluation of switching schemes suitable for a fiber geometry, as reviewed below. Four basic methods will be discussed, namely mechanical and passive  $Q$ -switching, electro-optic  $Q$ -switching using an external crystal (or electro-optic fiber), and internal electro-optic  $Q$ -switching using an active electro-optic material.

#### 2. Mechanical $Q$ -Switching

One of the simplest  $Q$ -switching methods involves mounting one of the fiber laser mirrors on a vibrating mirror assembly. This assembly is used to vibrate the mirror about an axis perpendicular to the fiber axis in a harmonic manner with some maximum angular deflection. Only during a small part of the cycle is the mirror aligned properly with the fiber laser cavity axis to allow laser oscillation and pulse generation to occur. During the rest of the cycle the cavity  $Q$  is very low, allowing the population inversion to build up.

Assuming that the mirror is properly aligned when the angular deflection of the mirror is zero at time  $t = 0$  the motion of the mirror may be described by

$$\phi = \phi_{max} \sin(2\pi ft) \quad (71)$$

where  $\phi_{max}$  is the maximum angular deflection and  $f$  the vibration frequency.

Under the condition that oscillation occurs when the mirror is aligned to within  $\delta\phi$  of the condition  $\phi = 0$  for perfect alignment, the switching time  $\delta t$  (from the off to the on

state) is approximately given by

$$\delta t = \frac{\delta \phi}{\phi_{max}} \frac{1}{2\pi f} \quad (72)$$

Equation (72) is derived from Equation (71) assuming that  $\phi$  is small.

In order to assure that only a single pulse is generated, the vibration frequency must be fast enough so that the mirror does not remain aligned much longer than some maximum time interval  $\Delta t_{on}$ . This sets a lower limit to  $f$  through Equation (72):

$$f_{min} = \frac{\delta \phi}{\phi_{max}} \frac{1}{2\pi \Delta t_{on}} \quad (73)$$

A second requirement is that there be enough time  $\Delta t_{off}$  between the *on* states ( $\phi = 0$ ) to build up the population inversion near its steady state value. Referring to Equation (71), this sets an upper limit on the vibration frequency of

$$f_{max} = \frac{1}{2\Delta t_{off}} \quad (74)$$

These combined requirements restrict the practical vibration frequency range to

$$\frac{\delta \phi}{\phi_{max}} \frac{1}{2\pi \Delta t_{on}} < f < \frac{1}{2\Delta t_{off}} \quad (75)$$

Past experience with mechanically chopped Nd:YAG lasers indicates that a switching time on the order of  $\Delta t_{on} = 5 \mu sec$  is enough to generate a single *Q*-switched pulse, while cavity alignment normally needs to be achieved to  $\delta \phi = 0.1^\circ$ . Also, commercially available vibrating mirrors have a typical maximum angular deflection  $\phi_{max} = 2^\circ$ . This yields a minimum frequency requirement  $f_{min} = 1.6 kHz$ . As for the maximum frequency limit, take  $\Delta t_{off} = \tau_f = 236 \mu sec$  as the minimum off-time needed to excite the laser, which yields  $f_{max} = 2.2 kHz$ . These approximate figures show that a frequency in the range of 1 to 3 kHz should be adequate.

For a typical mirror of length  $l_m$  along a direction perpendicular to the rotation axis positioned at a distance  $d_m$  away from the end of the fiber  $\phi_{max}$  must be bounded according to

$$\phi_{max} < \sin^{-1} \left( \frac{2d_m}{l_m} \right) \quad (76)$$

so that the mirror will avoid touching the fiber mounting jig. As an example, consider the case of a mirror with a transverse dimension of 1 mm located 20  $\mu m$  from a fiber end-face. Equation (76) indicates that the maximum deflection of the mirror must not exceed  $2.3^\circ$ .

This method has the advantages of being easy to implement and contributing only a small added cavity loss during the *on* state (if switching occurs fast enough). At this point it is difficult to say whether a frequency of a few *kHz* will be sufficient for single pulse generation. But it should be enough to characterize the general device behavior. It is considered to be a straightforward next step in the study of  $1.064\ \mu\text{m}$  fiber lasers and, in the next phase of this work, might lead to the first practical demonstration of a pulsed single crystal fiber laser.

### 3. Electro-optic *Q*-Switching

A more attractive approach uses a miniature electro-optic crystal inserted between the fiber laser and one of the mirrors along with a miniature polarizer.<sup>22,23</sup> A typical arrangement is given in Figure 29. An optical field passing through the polarizer is linearly polarized according to the polarizer orientation. This field then passes through the electro-optic crystal, is reflected by the mirror, and once again passes through the crystal before impinging onto the polarizer. As the field passes through the crystal it is decomposed into orthogonally polarized components along the principal axes. A voltage of sufficient magnitude is applied to the crystal in an appropriate orientation to cause a relative phase shift of  $\frac{\pi}{2}$  radians between the two eigenpolarizations. Upon returning to the polarizer the optical field has experienced a phase shift of  $\pi$  radians between its polarization components so that it is linearly polarized at  $90^\circ$  to the original orientation and is consequently rejected by the polarizer. Laser oscillation can thus be suppressed in this manner to allow the population inversion to be pumped well above the threshold level. Momentarily switching the applied voltage to zero results in returning the cavity to its normal high-*Q* (low loss) state, which causes emission of a *Q*-switched output pulse.

The configuration shown in Figure 29 uses ring electrodes to generate the electric field along the fiber length. Such electrodes provide a fairly constant voltage across the fiber cross-section. A significant advantage of this type of electrode is that it does not contribute any additional loss to the optical field. Another possibility is to deposit transparent electrodes on the end-faces of the electro-optic fiber (or rod). The additional loss from such electrodes has not yet been evaluated.

The extinction ratio required for a polarizer need not be very high to work efficiently in a *Q*-switched device; a value of 10-20 *dB* should be sufficient. The polarizer transmission should, however, be as high as possible. Concerning miniature polarizing devices, micro polarizers consisting of alternate layers of a metal and a dielectric material have been recently reported in the literature.<sup>22,23</sup> These, and a number of other thin polarizers, may



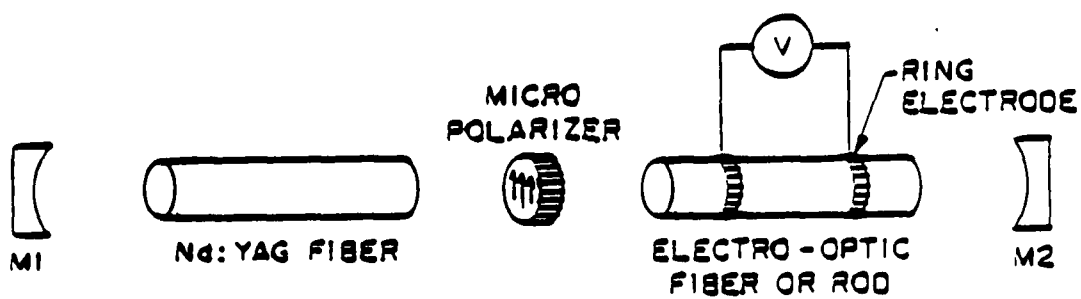


Figure 29 - Typical Arrangement for an Electro-Optic Switch in a Fiber Laser.

prove useful for the present purpose.

An example of this type of device is  $z$ -cut  $KD^*P$  in which the light propagates along the  $z$  axis of the crystal with the electric field applied along the same direction. In this configuration the light would initially be polarized along the  $x$  axis of the crystal and be decomposed into components polarized along the eigenvectors of the crystal which are located at  $+45^\circ$  and  $-45^\circ$  to the  $x$  axis. The phase shift between these two components is given by

$$\Delta\phi = \left( \frac{2\pi l}{\lambda_0} n_0^3 r_{63} \right) E_z = \left( \frac{2\pi}{\lambda_0} n_0^3 r_{63} \right) V_z \quad (77)$$

where  $n_0$  is the ordinary index of refraction,  $\lambda_0$  is the wavelength in free space,  $r_{63}$  is the linear electro-optic coefficient, and  $V_z$  is the applied voltage along the length  $l$  of the crystal, which results in the electric field of magnitude  $E_z$  in this direction. For  $KD^*P$  at a wavelength of  $1.064 \mu m$ ,  $n_0 = 1.4948$  and  $r_{63} = 25 \times 10^{-12} m/V$ . A relative phase shift of  $\frac{\pi}{2}$  radians is obtained with an applied voltage of  $3.2 kV$ . The rise-time is generally on the order of  $0.5 nsec$ .

Typical dimensions for such a device would be a  $500 \mu m$  diameter crystal with a length of at most a few  $mm$ . This crystal would be incorporated into a laser cavity along with a polarizer and a fiber made of Nd:YAG. The Q-switched laser analysis conducted under this contract shows that an  $8 mm$  long clad Nd:YAG fiber possessing an index difference of  $0.005$  would produce maximum peak output power with a core diameter of about  $22 \mu m$ .

Since the electric field is applied along the direction of light propagation, the phase shift is independent of the length of the crystal. It would be preferable to apply the electric field transversely so that (1) the phase shift would then depend on the ratio of the length to the transverse dimension which could be quite large for a small crystal, resulting in a reduction of the switching voltage, and (2) the electrode configuration does not introduce additional loss to the laser cavity. This type of orientation does not exist in  $KD^*P$  but is possible with  $LiNbO_3$ .

In  $LiNbO_3$  two configurations can be considered where the light propagates along the  $z$  axis of the crystal. In the first configuration the electric field is applied parallel to the  $y$  axis. The eigenvectors of this system are found to lie along the  $x$  and  $y$  axes. In the second configuration the electric field lies along the  $x$  axis which results in eigenvectors oriented at  $+45^\circ$  and  $-45^\circ$  with respect to the  $x$  (or  $y$ ) axis of the crystal. In either situation the phase difference between orthogonal polarization components is given by<sup>17</sup>

$$\Delta\phi = \left(\frac{2\pi l}{\lambda_0} n_0^3 r_{22}\right) E_0 = \left(\frac{2\pi}{\lambda_0} n_0^3 r_{22}\right) \left(\frac{l}{d}\right) V_0 \quad (78)$$

Here  $r_{22}$  is the electro-optic coefficient of interest and  $d$  is the distance between electrodes. Figure 30 shows a plot of the voltage necessary to produce a double-pass phase shift of  $\pi$  radians between the two eigenpolarizations versus the ratio of the length to the diameter of a  $\text{LiNbO}_3$  fiber (or small rod). This data was calculated using  $r_{22} = 3.4 \times 10^{-12}$  m/V,  $\lambda = 1.064$   $\mu\text{m}$ , and  $n_0 = 2.30$ . Also, the electrodes are assumed to be deposited directly onto the fiber (or rod). If this is not the case, the information presented in the figure is still valid provided that the diameter is interpreted to mean the distance between the electrodes. A 4 mm  $\text{LiNbO}_3$  fiber with a diameter of 22  $\mu\text{m}$  will switch with approximately 35 V compared to a switching voltage of 380 V required in a 4 mm long, 250  $\mu\text{m}$  diameter fiber.

#### 4. Electro-optic Active Material: Nd:LiNbO<sub>3</sub>

The above configuration introduces the additional complexity of having to align a second fiber within the laser cavity. It also increases the overall device length and round-trip loss. Added losses from coupling to the electro-optic single crystal fiber, as well as internal fiber losses, may degrade device performance. These undesirable characteristics may be avoided by simply merging the laser gain of Nd:YAG fibers with the electro-optic properties of  $\text{LiNbO}_3$  fibers. This is the case in Nd:LiNbO<sub>3</sub> single crystal fibers where the laser host crystal is itself electro-optic.

Laser action has been demonstrated in bulk Nd:LiNbO<sub>3</sub> by several authors.<sup>24-29</sup> The neodymium ion concentration in these crystals was typically 0.5-2.0%. Room temperature laser oscillation was observed on several lines of the  $4F_{3/2} \rightarrow 4I_{11/2}$  transition between 1.08  $\mu\text{m}$  and 1.10  $\mu\text{m}$ .

Some of the laser parameters of Nd:LiNbO<sub>3</sub>, measured by other authors, are listed in Table 8. The stimulated emission cross-section of Nd:LiNbO<sub>3</sub> (0.5% doped) is only slightly lower than that of Nd:YAG at 1.064  $\mu\text{m}$  (1% doped). Its fluorescence lifetime is fairly long although it is about 2-3 times smaller than that of Nd:YAG. Gain per unit pump power is expected to be 7-8 times lower in 0.5% Nd:LiNbO<sub>3</sub> than in Nd:YAG.<sup>27</sup>

Initially, laser oscillation was obtained only in rods with the geometrical axis perpendicular to the  $c$ -axis of the crystal ( $c \perp F$ , where  $F$  is the direction of laser signal propagation). In these cases the laser signal output was observed to decrease and finally disappear after about 10 minutes of operation. This behavior was attributed to laser damage in the crystal due to the high optical intensity at the pump wavelength ( $\lambda_p \approx 753$  nm, 6

# SWITCHING VOLTAGE FOR A LiNbO3 FIBER

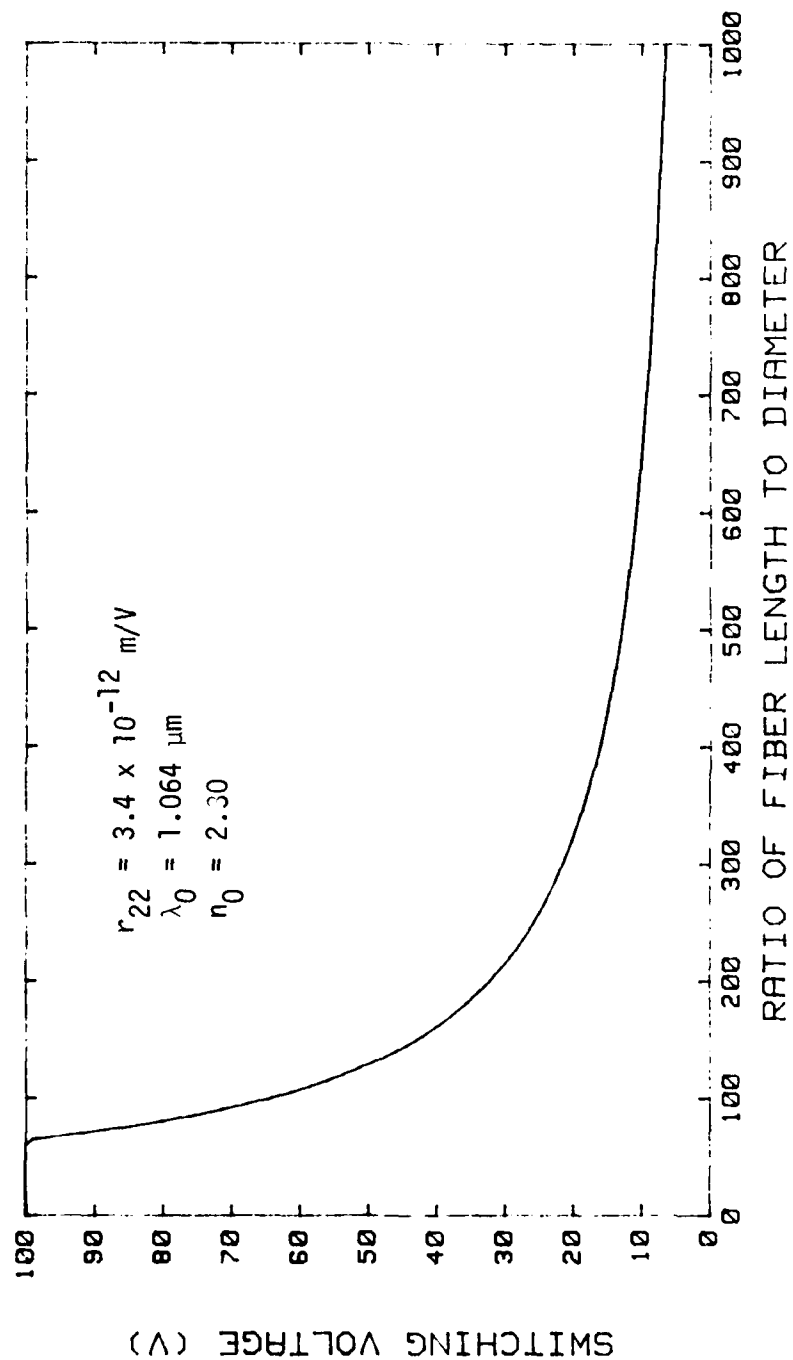


Figure 30 - Required Switching Voltage for a LiNbO<sub>3</sub> Fiber as a Function of the Ratio of Length to Diameter.

Table 8.

Measured Optical Parameters of Nd:LiNbO<sub>3</sub> ( $c \perp F$ )

Fluorescence Lifetime ( $\pm 5 \mu s$ )	100 $\mu s$ (0.5% Nd), 85 $\mu s$ (1.0% Nd), 80 $\mu s$ (2.0% Nd)
Cross-Section	$1.1 \times 10^{-19} \text{ cm}^2$ (0.5% doped)
Fluorescence Linewidth	22 $\text{cm}^{-1}$ ( $\lambda = 1.0846 \mu m$ ), 30 $\text{cm}^{-1}$ ( $\lambda = 1.0932 \mu m$ )
Scattering Loss	0.03 dB/cm (0.5% doped)

$\text{kW/cm}^2$ ).

Optical damage in LiNbO<sub>3</sub> has been known for many years and mechanisms have been identified that explain its origin. Two standard methods to avoid optical damage are 1) operate the crystal above a critical temperature ( $\sim 120^\circ \text{C}$  in LiNbO<sub>3</sub>) and 2) to propagate along the  $c$ -axis of the crystal. As explained previously, this last configuration, in which the optical field propagates along the crystal  $c$ -axis with the electric field applied transversely, is also advantageous because it requires lower switching voltages. Another solution to the damage problem is to use damage-free LiNbO<sub>3</sub>. A boule of LiNbO<sub>3</sub> that showed no optical damage when subjected to  $cw$  optical intensities ranging up to several hundreds of  $\text{kW/cm}^2$  (near  $\lambda = 0.5 \mu m$ ) has recently been grown in China. This damage threshold is many orders of magnitude above the best results obtained previously. Mass spectroscopy revealed the presence of several impurities in the crystal, including Mg, halogens, transition metals, and even Fe<sup>28</sup> which was long thought to be the major cause of damage in LiNbO<sub>3</sub>.

Crystal Technology has recently reported the growth of damage-free LiNbO<sub>3</sub>.<sup>28</sup> Samples have been made available to the Ginzton Laboratory and are expected to be commercially available soon. Also, single crystal fibers grown from damage-free LiNbO<sub>3</sub> have been successfully grown on the fiber growth station of the Ginzton Laboratory, and their damage threshold is now being evaluated. Doping these fibers with Nd-ions would then proceed in a straightforward manner using a method previously demonstrated here with CaSc<sub>2</sub>O<sub>4</sub>.<sup>10</sup>

More recently, laser action in Nd:LiNbO<sub>3</sub> has been achieved in the  $c||F$  configuration.<sup>29</sup> It was found that in previous attempts stimulated emission was inhibited by  $UV$  radiation from the pump lamp. Pulsed laser operation in  $c||F$  Nd:LiNbO<sub>3</sub> has been observed at  $\lambda = 1.0932 \mu m$  using  $UV$ -filtered pump lamps with a threshold only about 70% larger than in the  $c \perp F$  configuration. In this mode, the crystal suffers no optical damage from the pump, and the  $r_{22}$  electro-optic coefficient can be used for signal modulation. It is not clear, however, why  $cw$  laser operation has not yet been reported in the  $c||F$  configuration.

## 5. Passive Q-Switching

Passive Q-switching is another potential scheme for Q-switching a fiber laser. It has the advantage over other methods of not requiring any applied voltage nor any polarizer so that a much simpler design is possible. A simple demonstration of this type of device would be to place a thin film of a saturable absorber (such as a dye solution) between a fiber end and mirror (the dye solution would be held by surface tension). When the fiber laser is optically pumped the saturable absorber is initially opaque to the signal field that would otherwise be circulating in the cavity. Since the absorption coefficient of the dye is a function of the optical field intensity, as the optical intensity  $I$  is increased the absorption coefficient decreases from its unsaturated value  $\alpha_0$  according to<sup>21</sup>

$$\alpha = \frac{\alpha_0}{1 + \frac{I}{I_s}} \quad (79)$$

where  $I_s$  is the saturation intensity of the dye. Initially, the dye absorption coefficient is equal to the large value of  $\alpha_0$  so that no laser oscillation can occur. During pumping the population inversion increases until the gain equals the loss in the cavity, i.e. when

$$2\alpha t + \delta_1 = \frac{n_{in}}{n_{t,i}} \delta_i = N \delta_i \quad (80)$$

Here  $t$  is the thickness of the dye film,  $\delta_1$  is the cavity loss not including the absorption of the dye,  $n_{in}$  is the population inversion at the onset of laser oscillation,  $\delta_i$  is the total cavity loss for the  $i^{th}$  transverse mode under normal conditions (high- $Q$  state), and  $n_{t,i}$  is the *cw* laser threshold inversion for a total loss equal to  $\delta_i$  in the cavity.  $N$  is the ratio of the initial to threshold inversions. Since  $n_{t,i}$  is proportional to  $\delta_i$ , Equation (80) is observed to be independent of the total loss  $\delta_i$ .

At this point the laser intensity begins to increase while the dye loss starts to decrease according to Equation (79). Laser rate equations show that after some build-up time the signal intensity circulating inside the cavity reaches its maximum value given by<sup>21</sup>

$$I_{i,max} = \left( \frac{2\delta_i}{T_1} \right) \left( \frac{P_{i,max}}{A_{eff}} \right) \quad (81)$$

Here  $A_{eff}$  is the effective area over which the power is distributed and  $P_{i,max}$  is the peak power of the output pulse given by Equation (55). The factor of 2 stems from the fact that the intensity which saturates the absorption is the sum of the counterpropagating intensities in the laser cavity. Note that Equation (81) assumes that the laser is operating in a single transverse mode (not necessarily the lowest order mode).

**Table 9.**

**Properties of Some 1.064  $\mu\text{m}$  Saturable Absorbers**

<i>Dye</i>	<i>Eastman #9740</i>	<i>Eastman #9860</i>	<i>Eastman #14015</i>
$I_s$ ( $\text{MW}/\text{cm}^2$ )	40	56	50
$\tau_D$ ( $\mu\text{sec}$ )	8.3	9.3	1000
<i>Stability</i>	<i>Average</i>	<i>Average</i>	<i>Excellent</i>

The residual dye loss corresponding to this maximum intensity is

$$\delta_b = \frac{2\alpha_0 t}{\left(1 + \frac{I_{s,\text{max}}}{I_s}\right)} \quad (82)$$

where the total loss  $\delta_i$  is related to  $\delta_b$  and  $\delta_1$  by

$$\delta_i = \delta_1 + \delta_b \quad (83)$$

From Equation (82) it is apparent that in order to minimize the residual dye absorption it is necessary that  $\frac{2\alpha_0 t I_s}{I_{s,\text{max}}} \ll 1$  which in turn translates into the requirement that the laser emission cross-section  $\sigma_l$  must be much smaller than the dye absorption cross-section. Another prerequisite for a saturable absorber, necessary for repeated  $Q$ -switching of the laser, is that the dye solution be photochemically stable.

For a given set of device parameters Equation (80) can be used to calculate the required unsaturated loss factor  $\alpha_0 t$  for a given pump power level. Equations (81) and (82) form a system of coupled equations which can be solved numerically to yield the residual loss  $\delta_b$  of the dye when it is bleached with the maximum intensity. The total loss  $\delta_i$  is then found from Equation (83) which allows the peak power in the output pulse to be calculated (Equation (55)).

Only a few saturable absorbers are available that absorb light in the vicinity of 1.064  $\mu\text{m}$ . Some of these are listed in Table 9 along with some data taken from the literature. Included is the recovery time from the bleached to the unbleached state.

Consider an 8 mm long Nd:YAG fiber laser with a diameter of 22  $\mu\text{m}$  and a core/cladding index difference of 0.005 operating at a wavelength of 1.064  $\mu\text{m}$ . For an input pump power of 60 mW coupled into the fiber ( $\lambda_p = 0.5145 \mu\text{m}$ ) and a loss  $\delta_1 = 0.05$  the required unsaturated loss factor is found to be 1.97 and the residual loss is 0.164 (total loss is then 0.214). The initial population inversion  $n_i$  at the onset of laser action is about  $N = 18.6$  times the threshold inversion ( $n_{t,i} = 7.15 \times 10^{11}$ ).

Peak output power from this device (with  $T_1 = 0.01$ ) under the stated operating conditions is approximately 200 W corresponding to a maximum intensity of  $2.2 \text{ GW/cm}^2$  (making the approximation that the field is fairly uniform over the entire core of the fiber). This intensity level is below the surface damage threshold in Nd:YAG which is on the order of 10's of  $\text{GW/cm}^2$ . This example assumes that Eastman #14015 dye is used as the saturable absorber ( $I_s = 50 \text{ MW/cm}^2$ ).

The behavior of the initial and threshold population inversions as a function of pump power is shown in Figure 31. As the pump power is increased the threshold inversion decreases rapidly at first and then begins to level off at higher pump powers (total bleaching of the dye). The initial inversion increases linearly with increasing pump power.

The unsaturated loss coefficient and the residual loss corresponding to the peak intensity are plotted in Figure 32 for pump powers up to 100 mW coupled into the fiber. These curves are similar to those shown in Figure 31. This is because the unsaturated loss coefficient is proportional to  $N_{in}$  (and thus to the pump power) while the threshold inversion is a linear function of the residual loss.

Peak output power as a function of pump power is presented in Figure 33. The peak power is observed to vary almost linearly with pump power.

## B. COMPARISON OF SWITCHING METHODS

Both active and passive methods of  $Q$ -switching have been considered in this section. All have been found to be feasible for use with a fiber although some methods are more desirable than others for various reasons. Mechanical  $Q$ -switching may lead to an early demonstration of a pulsed fiber laser as would a passive scheme using a saturable absorber but these methods would limit the practical usefulness of such devices. In particular, mechanical  $Q$ -switching requires a vibrating mirror assembly be brought in close proximity to a fiber end-face. This would tend to hinder efforts to miniaturize the device. Limited dye lifetimes would naturally lead to shorter overall lifetimes for the pulsed lasers that used this method.

An electro-optic  $Q$ -switching scheme partially overcomes these difficulties and allows for the possibility of the electro-optic crystal to be implemented in a fiber format, compatible with the laser host geometry. The disadvantage of this method is that an external fiber would have to be aligned with the laser host fiber although butt-coupling the two fibers may minimize this problem. A laser host material that is itself electro-optic, such as Nd-doped  $\text{LiNbO}_3$ , overcomes this problem entirely although both methods suffer from the disadvantage of requiring a polarizer. Miniature polarizers have been reported in the



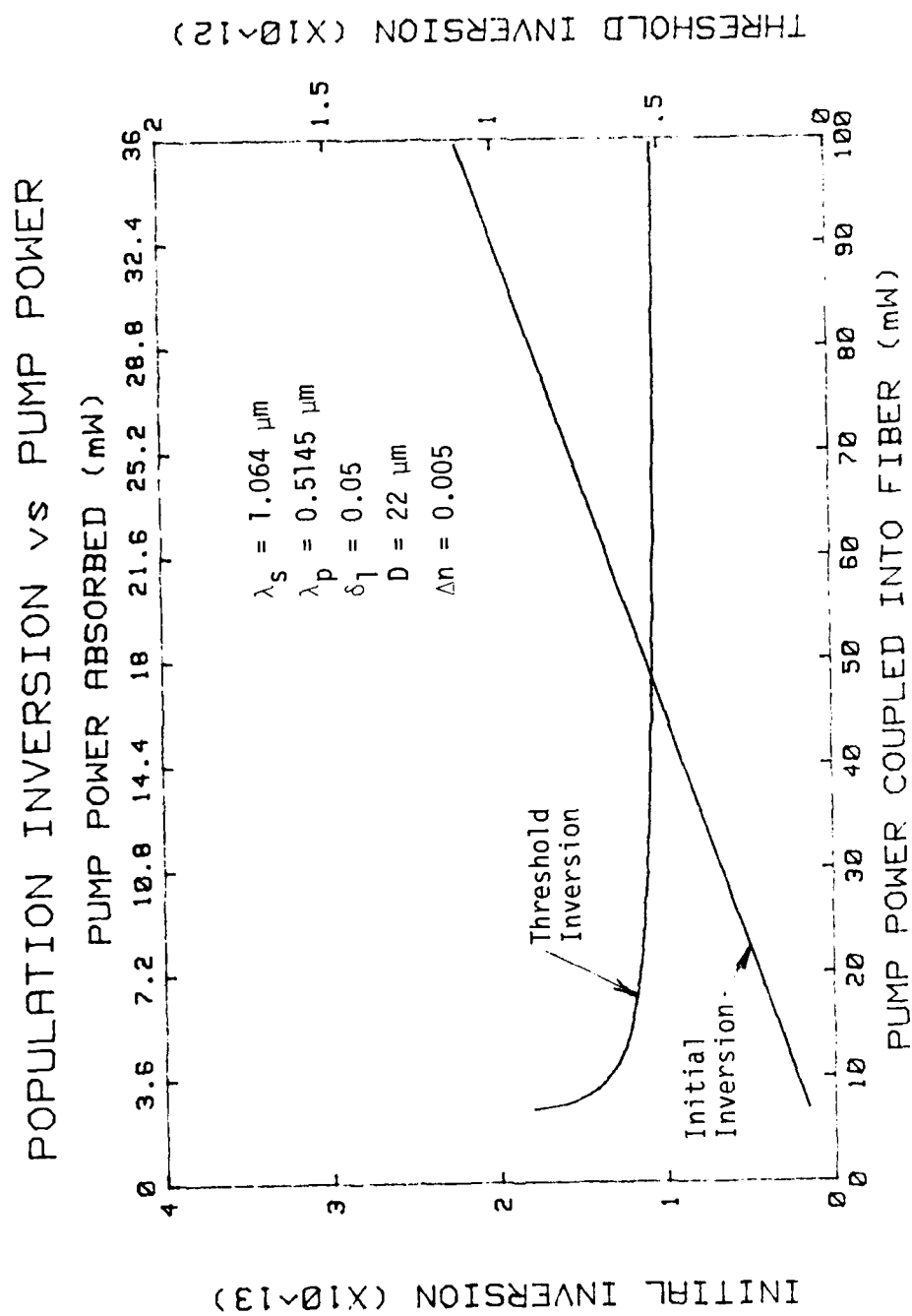


Figure 31 - Initial and Threshold Population Inversions as a Function of Pump Power using a Saturable Dye Absorber.

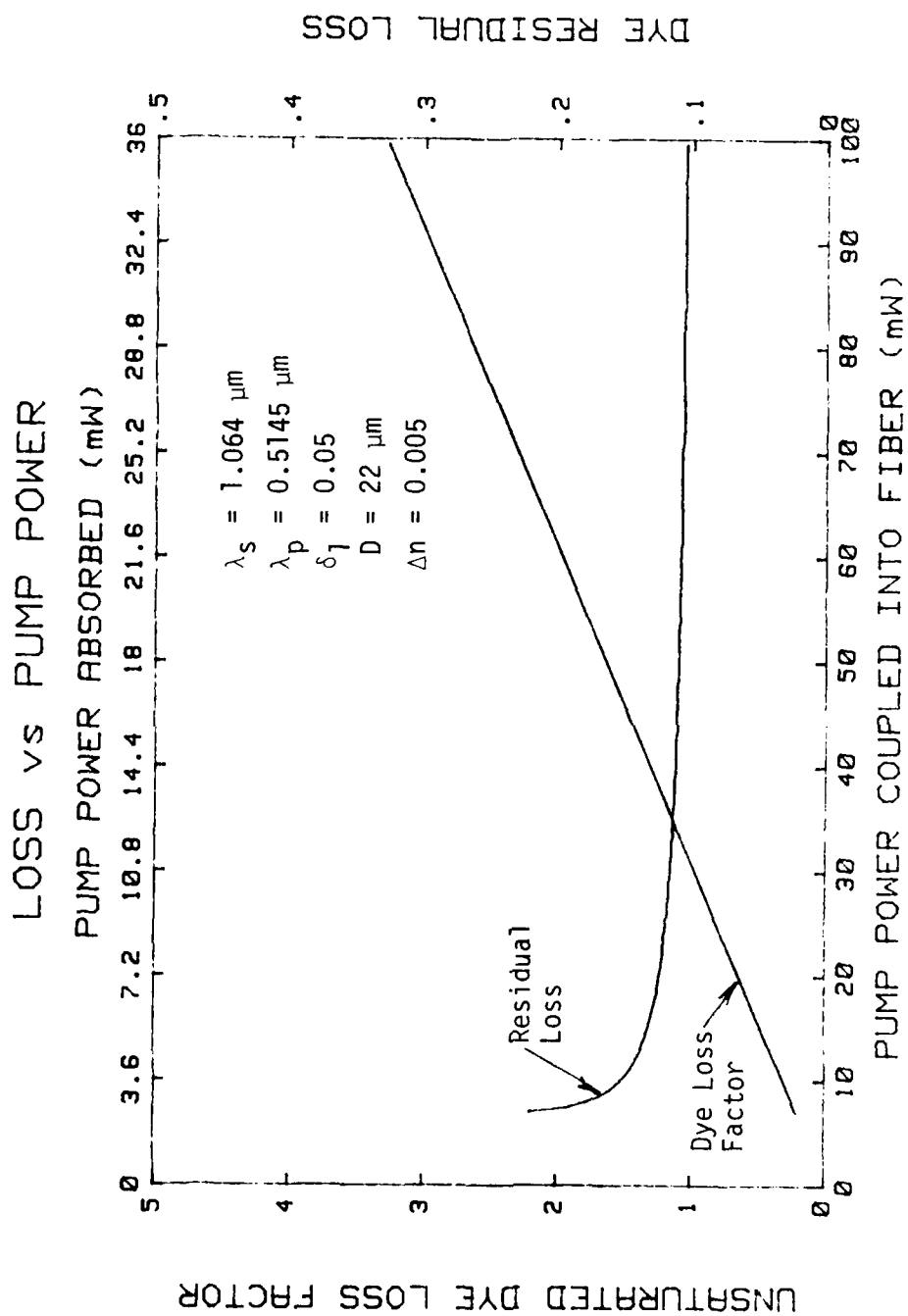


Figure 32 - Dye Loss versus Pump Power.

AD-A163 106

DIODE PUMPED FIBER LASER(U) STANFORD UNIV CA EDWARD L  
GINZTON LAB OF PHYSICS C GAETA ET AL DEC 84 GL-3756  
AFWAL-TR-84-1159 F33615-82-C-1749

2/2

UNCLASSIFIED

F/G 20/5

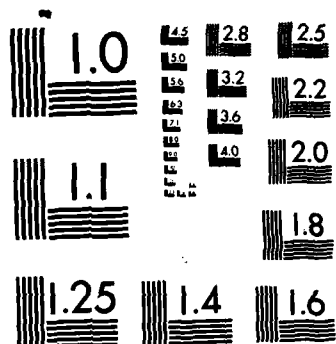
NL

END

FILED

..

DTIC



MICROCOPY RESOLUTION TEST CHART  
NATIONAL BUREAU OF STANDARDS-1963-A

# PEAK OUTPUT POWER VS PUMP POWER

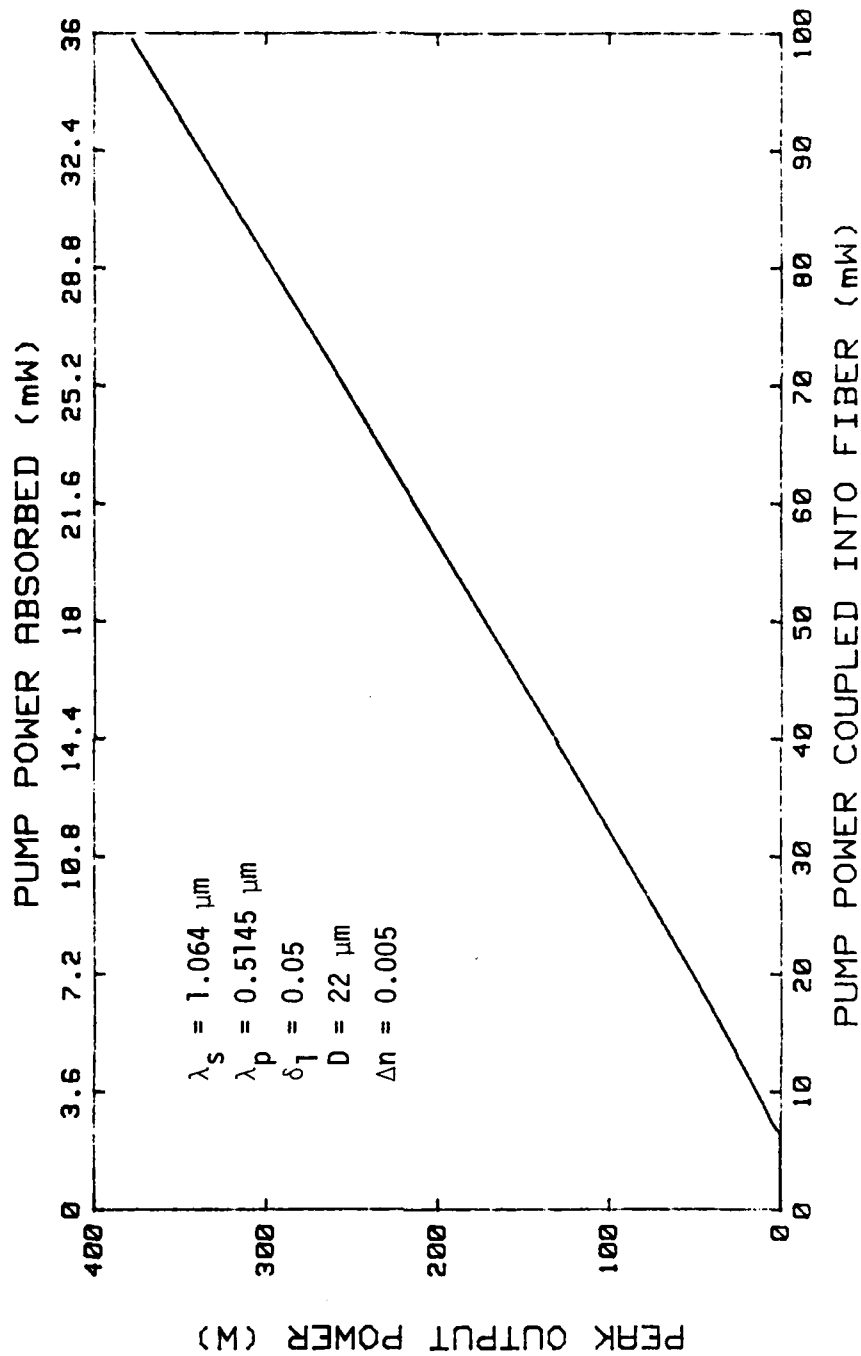


Figure 33 - Peak Output Power versus Pump Power.

literature but their eventual usefulness for pulsed fiber laser applications has yet to be assessed.

### C. RECOMMENDATIONS

At this time it appears that the most appealing choice for  $Q$ -switching a fiber laser is the use of the combined active and electro-optic properties of a fiber of Nd-doped ( $c$ -axis)  $\text{LiNbO}_3$ . Such a device is self-contained and therefore eliminates the need to align an additional crystal modulator. These fibers have already been grown on the same fiber growers that produce the Nd:YAG fibers for this contract. The emission wavelength from such a device will be only slightly different from the  $1.064 \mu\text{m}$  line of Nd:YAG. A study of the emission spectrum from this little-known material as well as an experimental evaluation of the electro-optic effect in both doped and undoped  $\text{LiNbO}_3$  fibers should probably precede device work.

In view of the relatively high (and fixed) switching voltage of  $\text{KD}^*\text{P}$  this material is not considered as an attractive candidate for a fiber laser  $Q$ -switch. A vibrating mirror and/or passive  $Q$ -switching with a saturable absorber will also be of immediate interest to study pulsed Nd:YAG fiber lasers in parallel with the evaluation of electro-optic fibers which may eventually be used as fiber laser  $Q$ -switches.

### III. CONCLUSION

The work performed under this contract resulted in the successful demonstration of laser action in  $170 \mu\text{m}$  and  $80 \mu\text{m}$  diameter Nd:YAG single crystal fibers using an argon ion laser as a pump source ( $\lambda_p = 0.5145 \mu\text{m}$ ). Thresholds as low as  $12 \text{ mW}$  and slope efficiencies of 22.3%, i.e., less than a factor of two below optimum value, have been observed. Losses inferred from laser measurements were lower for these fibers than for the fibers used in earlier work at  $\lambda = 1.064 \mu\text{m}$ . This attests to the higher quality of the new set of fibers, due to an improved diameter control. The measured value of  $\sigma = 0.67 \times 10^{-19} \text{ cm}^2$  for the gain cross-section of these fibers agrees well with measured bulk laser data at  $1.32 \mu\text{m}$ .

Fiber processing was advanced to the point where individual fiber lasers are now produced using a new high temperature epoxy. In the near future this may allow for a good quality thin film deposition directly onto the fiber end-faces. Capillary tubes used in the construction of these devices allowed for good tolerances to be obtained in polishing the end-faces of the fiber perpendicular to the fiber axis. Techniques developed here will

pave the way for the development of practical single crystal fiber devices such as stabilized sources and monolithic lasers.

Under the present contract a theoretical model of the interaction of the pump and signal fields in a pulsed fiber laser has also been developed. A range of the core radius has been shown to exist which maximizes the peak power and energy of the optical pulse emitted by the laser while minimizing the pulse width. Results were obtained for both argon laser and laser diode pumped Nd-YAG fiber lasers.

A variety of standard *Q*-switching methods were evaluated in order to determine their suitability for use with a fiber laser. A detailed investigation was made of each method and examples of possible designs using these techniques included to illustrate the features offered by each of them.

This work is an important first step in the development of pulsed fiber laser systems. Future work in this area should primarily include an experimental feasibility study of some of the *Q*-switching techniques discussed here. This should include a study of miniature polarizers which are important in a scheme involving an electro-optic material. A promising material for such an application is damage-free LiNbO<sub>3</sub>. Characterization of the electro-optic and optical properties of this material should precede or parallel the development of electro-optically *Q*-switched fiber lasers.

## REFERENCES

1. R. A. Bergh, et al., "Overview of Fiber-Optic Gyroscopes," IEEE Journal of Lightwave Technology LT-1, 2, 91-107 (April 1984).
2. L. F. Stokes, et al., "Sensitive All-Single-Mode Fiber Resonant Ring Interferometer," IEEE Journal of Lightwave Technology LT-1, 1, 110-115 (March 1983).
3. S. A. Newton, et al., "Single Mode Fiber Recirculating Delay Line," Proc. SPIE 326, 108-115 (January 1982).
4. K. P. Jackson, et al., "Optical Fiber Delay Line Signal Processing," to be published in IEEE Trans. on Microwave Theory and Techniques.
5. T. Giallorenzi, et al., "Optical Fiber Sensor Technology," IEEE Journal of Quantum Electronics, QE-18, 4, 626-665 (April 1982).
6. C. A. Burrus and J. Stone, "Single-Crystal Fiber Optical Devices: A Nd:YAG Fiber Laser," Applied Physics Letters 26, 6, 318-320 (March 1975).
7. J. Stone and C. A. Burrus, "Self-Contained LED-pumped Single-Crystal Nd:YAG Laser," Fiber and Integrated Optics, 2, 1, 19-46 (1979).
8. M. Digonnet and H. J. Shaw, "Fiber Ring Laser Gyro Amplifiers," Final Technical Report, No. AFWAL-TR-81-1067, for Contract F33615-79-C-1789.
9. M. Digonnet and H. J. Shaw, "Diode Pumped Fiber Laser," Final Technical Report, No. AFWAL-TF-83-1110, for Contract F33615-82-C-1749.
10. R. S. Feigelson, "Growth of Fiber Crystals," Fifth International Summer School on Crystal Growth, Davos, Switzerland, to be published.
11. M. M. Fejer, et al. "Growth and Characterization of Single Crystal Refractory Oxide Fibers," Proc. of SPIE 320, p. 50 (1982).
12. M. M. Fejer, to be published.
13. NASA Publication, NASA RP-1061(1980).
14. Epoxy Technology.
15. M. J. F. Digonnet and C. J. Gaeta, "Theoretical Analysis of Optical Fiber Laser Amplifiers and Oscillators," submitted for publication in Applied Optics.
16. H. Kogelnik and T. Li, "Laser Beams and Resonators," Applied Optics 5, 10, 1550-1567 (October 1966).
17. A. Yariv in *Quantum Electronics*, John Wiley and Sons, Inc., New York (1975).
18. D. Marcuse in *Theory of Dielectric Optical Waveguides, Quantum Electronics, Principles and Applications*, Academic Press (1974).



19. *Handbook of Lasers with Selected Data on Optical Technology*, CRC Press, Cleveland.
20. Ken'ichi Kubodera and Kenju Otsuka, "Single-Transverse-Mode LiNdP<sub>40</sub>12 Slab Waveguide Laser," *Journal of Applied Physics* **50**, 2, 653-659 (February 1979).
21. W. Koechner in *Solid State Laser Engineering*, Springer Series in Optical Sciences 1, Springer-Verlag (1976).
22. Shojiro Kawakami, "Light Propagation Along Periodic Metal-Dielectric Layers," *Applied Optics* **22**, 16, 2426-2428 (August 1983).
23. Kazuo Shiraishi, et al., "Fiber Faraday Rotator," *Applied Optics* **23**, 7, 1103-1106 (April 1984).
24. N. F. Evalanova, et al., *JETP Letters* **5**, 10, 291 (1967).
25. L. F. Johnson, et al., *Journal of Applied Physics* **40**, 1, 297 (January 1969).
26. L. I. Ivleva, et al., *Soviet Physics - Doklady, Crystallography* **13**, 12, 1185 (1969).
27. I. P. Kaminow and L. W. Stulz, *IEEE J. Quantum Electronics*, **QE-11**, 306 (1975).
28. Robert Byer, Stanford University, private communication.
29. A. A. Kaminskii, *Phys. Stat. Sol. (a)*, **1**, 573 (1970).

**END**

**FILMED**

24-86

**DTIC**